Australian Government
Bureau of Meteorology

# ACCESS-A: Development of the pan-Australia convective-scale numerical weather prediction model

**Charmaine Franklin, Shaun Cooper, Belinda Roux, Mathew Lipson, Scott Wales**

**August 2025**

*Bureau Research Report - 117*

# ACCESS-A: Development of the pan-Australia convective-scale numerical weather prediction model

Charmaine Franklin, Shaun Cooper, Belinda Roux, Mathew Lipson, Scott Wales

Bureau of Meteorology

Bureau Research Report No. 117

August 2025

National Library of Australia Cataloguing-in-Publication entry

Authors: Charmaine Franklin, Shaun Cooper, Belinda Roux, Mathew Lipson, Scott Wales

Title: ACCESS-A: Development of the pan-Australia convective-scale numerical weather prediction model

ISBN: 978-1-923469-11-2

ISSN: 2206-3366

Series: Bureau Research Report – BRR117

Enquiries should be addressed to:

Lead Author: Charmaine Franklin

Bureau of Meteorology

GPO Box 1289, Melbourne

Victoria 3001, Australia

charmaine.franklin@bom.gov.au

## Copyright and Disclaimer

© Commonwealth of Australia 2025

Published by the Bureau of Meteorology

To the extent permitted by law, all rights are reserved and no part of this publication covered by copyright may be reproduced or copied in any form or by any means except with the written permission of the Bureau of Meteorology.

The Bureau of Meteorology advise that the information contained in this publication comprises general statements based on scientific research. The reader is advised and needs to be aware that such information may be incomplete or unable to be used in any specific situation. No reliance or actions must therefore be made on that information without seeking prior expert professional, scientific and technical advice. To the extent permitted by law and the Bureau of Meteorology (including each of its employees and consultants) excludes all liability to any person for any consequences, including but not limited to all losses, damages, costs, expenses and any other compensation, arising directly or indirectly from using this publication (in part or in whole) and any information or material contained in it.

# Contents

## List of Figures

## List of Tables

# Executive Summary

This report documents the development of the ACCESS-A model including the model grid design and science configuration. This model development is the pre-assimilation development, which is required to ensure that the model accurately represents the physics and dynamics of the atmosphere-land system, is numerically stable and provides a reliable baseline for introducing observational data assimilation.

The ACCESS-A model grid covers the entire nation, with the stretched grid reducing in resolution from 1.5 – 4 km around the horizontal boundaries to deal with the effects of lateral boundary spin up. The science configuration tested in this report is the RAL3.1 (Regional Atmosphere and Land) configuration, which is the final configuration used for ACCESS-A apart from an additional minor fix introduced as RAL3.2 that does not affect the model characteristics or evaluation against observations.

ACCESS-A is numerically stable and has a realistic representation of high impact weather across Australia. For the small number of cases tested, tropical cyclones are well simulated, although their peak intensities tend to be underestimated. The large rainfall accumulations of flooding events are captured, with occasional displacement of the heaviest falls supported by high fractions skill scores. Convective behaviour is broadly realistic, with too many small convective cells indicating less organisation. Maximum fog fraction spatial distributions and the associated reduced visibility compares well with observations. Extreme winter weather temperatures and summer heat are realistically captured, with evidence of 10m winds speeds over complex topography being too low. Thunderstorm tracks and lightning flashes qualitatively align with observations, confirming the model's capability to reproduce key weather features.

Verification across tropical, subtropical, southeastern, central and Mediterranean Australian (southwest – southcentral) domains shows generally good performance with consistent model biases:

- Rainfall: 6 hourly precipitation accumulations compare well with rain gauge observations. Southern domains tend to show an underestimate in heavy rain rates compared to GPM-IMERG satellite observations.
- Screen level temperature and humidity: A cold and moist bias overnight in tropical and central domains, mostly neutral to slightly warm morning biases elsewhere.
- 10m wind speeds: Overestimated overnight in tropical and central domains, underestimated during the day in other regions.
- Cloud cover: Slight underprediction, particularly overnight, contributing to cold biases in some domains.

### Additional summary for operational weather forecasting

From an operational weather forecasting perspective, the ACCESS-A RAL3 science configuration includes several key differences compared to the RAL1 configuration used in ACCESS-C3 and C4:

- Precipitation characteristics: RAL3 has more light and less heavy precipitation.

- Frontal precipitation: There is an increase in light precipitation around fronts.
- Cloud cover: Cloud cover appears more realistic; however, care needs to be taken with interpretation of high cloud fraction.
- Orographic precipitation: Stronger orographic enhancement of precipitation.
- Cyclone intensity: In the limited number of tropical and extra-tropical cyclones examined they tend to be weaker than those simulated with RAL1.

# 1. Introduction

Regional convective-scale numerical weather prediction (NWP) models have been operational at the Bureau since 2017. As for other national meteorological centres, these convective-scale models have proven to provide enhanced predictive capabilities for forecasting precipitation and high-impact weather and provide valuable information on local weather.

The km-scale horizontal grid boxes of convective-scale models bring benefits over coarser global models for two main reasons. The higher resolution allows the dynamics of atmospheric convection to be modelled with sufficient accuracy that the convection parameterisation can be turned off. Switching off the convection scheme significantly improves modelled precipitation, including a more realistic diurnal cycle, better inland propagation of coastal convection, and also allows the model to represent convective organisation, including the associated extreme rainfall and wind gusts. The km-scale of convective-scale models means a more accurate representation of local topography and coastlines compared to global models, resulting in improvements to modelled forecasts of orographic precipitation, land-sea breeze circulations and localised fog.

The first Bureau convective-scale system was the APS2 upgrade of the ACCESS-City system, ACCESS-C2, which comprised 6 domains with a 1.5km horizontal grid length (Roff et al. 2022). The APS3 upgrade in 2020 saw data assimilation introduced with hourly 4D-Var in ACCESS-C3, (Rennie et al. 2022) and the first convective-scale ensemble system with 12 members at 2.2km horizontal grid length, ACCESS-CE3 (Cooper et al. 2025). As demand for high-resolution model forecasts over other regions of the country increased, APS3 release 2 introduced a further ACCESS-City domain over northern Queensland. With increasing demand for national coverage of convective-scale NWP models, work has begun on developing ACCESS-A and ACCESS-AE.

ACCESS-A has the potential to bring scientific benefits and improved performance over the smaller ACCESS-C domains due to the larger domain's ability to develop its own dynamical circulation. This is because ACCESS-A is less constrained by the driving model and its biases. The larger domain means that the model can capture a greater range of scale interactions where mesoscale variability could influence the larger circulation. In addition, the effect of spin-up from the lateral boundaries is pushed away from the areas of interest, producing more accurate precipitation characteristics (Warner et al. 2025).

The ACCESS-A model described in this report is the initial development that configured and tested the model grid and science configuration with no data assimilation. The implementation and testing of data assimilation in ACCESS-A is documented by Rennie et al. (2025).

# 2. Model description

## 2.1. Model domain and grid

The prognostic variables used in the RAL3.1 configuration are the three-dimensional wind components, virtual dry potential temperature, Exner pressure, dry density and six moist prognostics, which due to the use of a new double moment cloud microphysics scheme (see sub-Section 2.2.1) expand the prognostics carried by ACCESS-City models (mass mixing ratios and number concentrations for each of the 5 hydrometeor species). The prognostic variables are discretised onto the horizontal latitude-longitude grid using Arakawa C-grid staggering, and in the vertical using Charney-Phillips staggering.

The ACCESS-A horizontal grid uses a variable resolution grid, which is the same approach used in the ACCESS-City models. The use of a variable resolution grid is a computationally cheaper approach than having a larger uniform resolution grid to deal with the impact of coarse resolution boundary condition information spinning up and affecting the region of interest. The outermost grid resolution of 0.036° (~4 km) contains 36 grid points, which then varies over 49 grid points to a uniform inner domain resolution of 0.0135° (~1.5 km) (see Figure 1). The extent of the 1.5km domain covers all the APS3 ACCESS-City domains.

A terrain-following hybrid height coordinate is used with 90 vertical levels, which includes 67 levels below 18km (33 below 4km, 16 below 1km) and 23 levels above this with a fixed model lid at 40km above sea level. Compared to the 80 vertical levels of the ACCESS-C3 model, ACCESS-A has enhanced vertical resolution in the lowest levels of the atmosphere, particularly in the boundary layer which helps with the representation of low cloud and fog.

The total number of horizontal grid points in ACCESS-A is 3690 x 3045, which together with the 90 vertical levels totals more than 1 billion grid points. This very large domain km-scale model is the largest the Bureau has developed, and will provide national km-scale NWP forecast guidance and output for downstream applications, as well as a wealth of research opportunities to assess the upscale influence of tropical convection on weather and climate in the tropics and extra-tropics, and provide data to support parameterisation development, machine learning applications and other research.

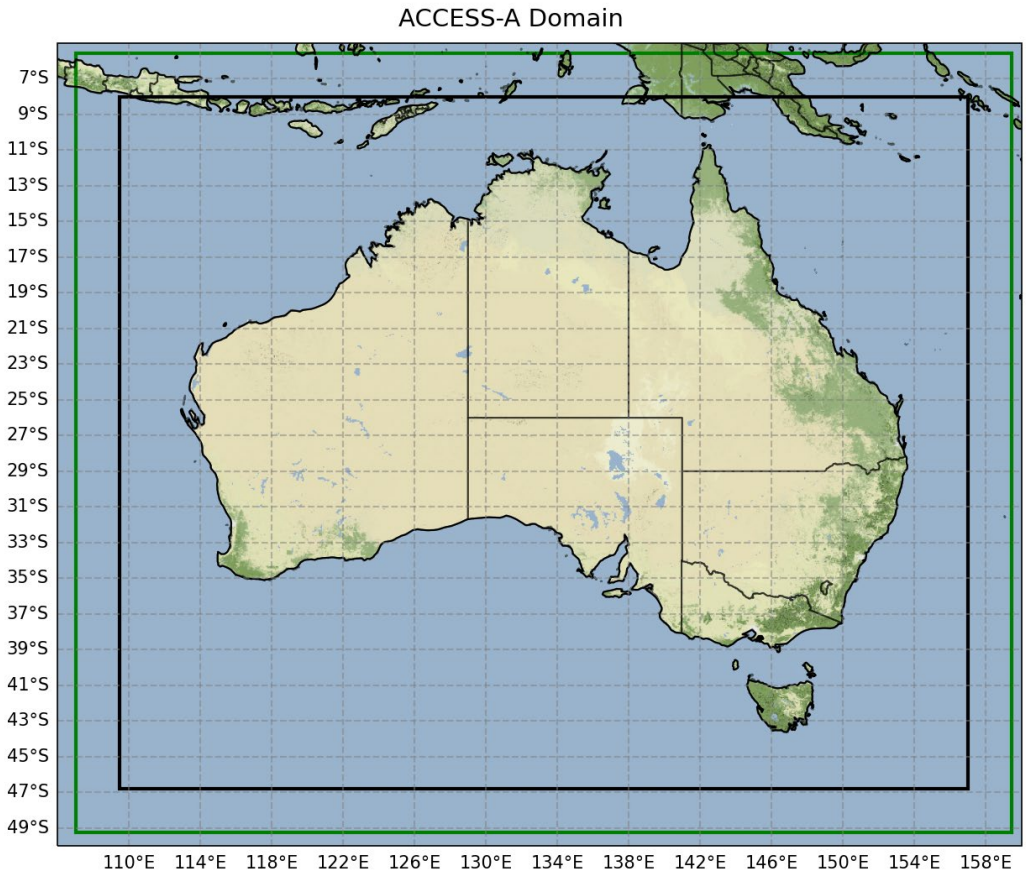


Figure 1: The outer ACCESS-A domain is denoted by the green rectangle and the uniform inner domain is shown by the black rectangle.

### 2.1.1 Lower boundary condition description

Information describing the characteristics of the lower boundary are specified in ancillary files. Some of these ACCESS-A details are described in this subsection with further details documented in Table 3 of Bush et al. (2025).

#### Land-sea mask and topography

The land-sea mask is generated using the European Space Agency (ESA) Climate Change Initiative (CCI) version 1.6.1 (Defourny 2016); however, some grid points are defined as sea even though they contain Automatic Weather Stations (AWS). Following the approach in ACCESS-C, the land-sea mask is flipped to land for ocean grids containing AWS stations if they include a neighbouring land point in the x/y direction (i.e. not diagonally, and not isolated islands). For ACCESS-A this results in 67 grids containing AWS being flipped from sea to land. The Shuttle Radar Topography Mission (SRTM) at 90m resolution is used to generate the model topography.

### Natural land cover and Leaf Area Index

Land cover ancillaries are generated from the European Space Agency (ESA) Climate Change Initiative CCI version 2.0.8 (hereafter CCIv2), available in annual maps from 1992-2020 at 300 m resolution (Harper et al. 2023). ACCESS-A uses the 2020 CCIv2 annual map, a year which had rainfall close to the long-term average across the nation. The resulting land cover ancillaries correct many of the deficiencies in the original CCI-based ancillaries including classifying ephemeral lakes designated as permanent water bodies, arid areas in central Australia as bare soil rather than permanent water, classifying large open cut mines as bare soil rather than urban, and removing needle leaf trees throughout central Australia (Figure 2). Other broad-scale changes include a greater proportion of grasses and a lower proportion of shrubs. Areas of bare soil and trees remain broadly similar.

Leaf Area Index (LAI) data is generated from MODIS collection 5 (De Kauwe et al. 2011), which has a resolution of 4.6 km. As the model resolution is much higher than the native LAI source data, this can generate spuriously high values of LAI, particularly in cases where the model grid box has a low vegetated fraction that lies in a more highly vegetated MODIS pixel. This issue was identified after the ACCESS-A model development had completed and remains an issue for future development, although we note that Met Office testing for a British Isles domain at 1.5km resolution revealed little impact of rectifying this problem.

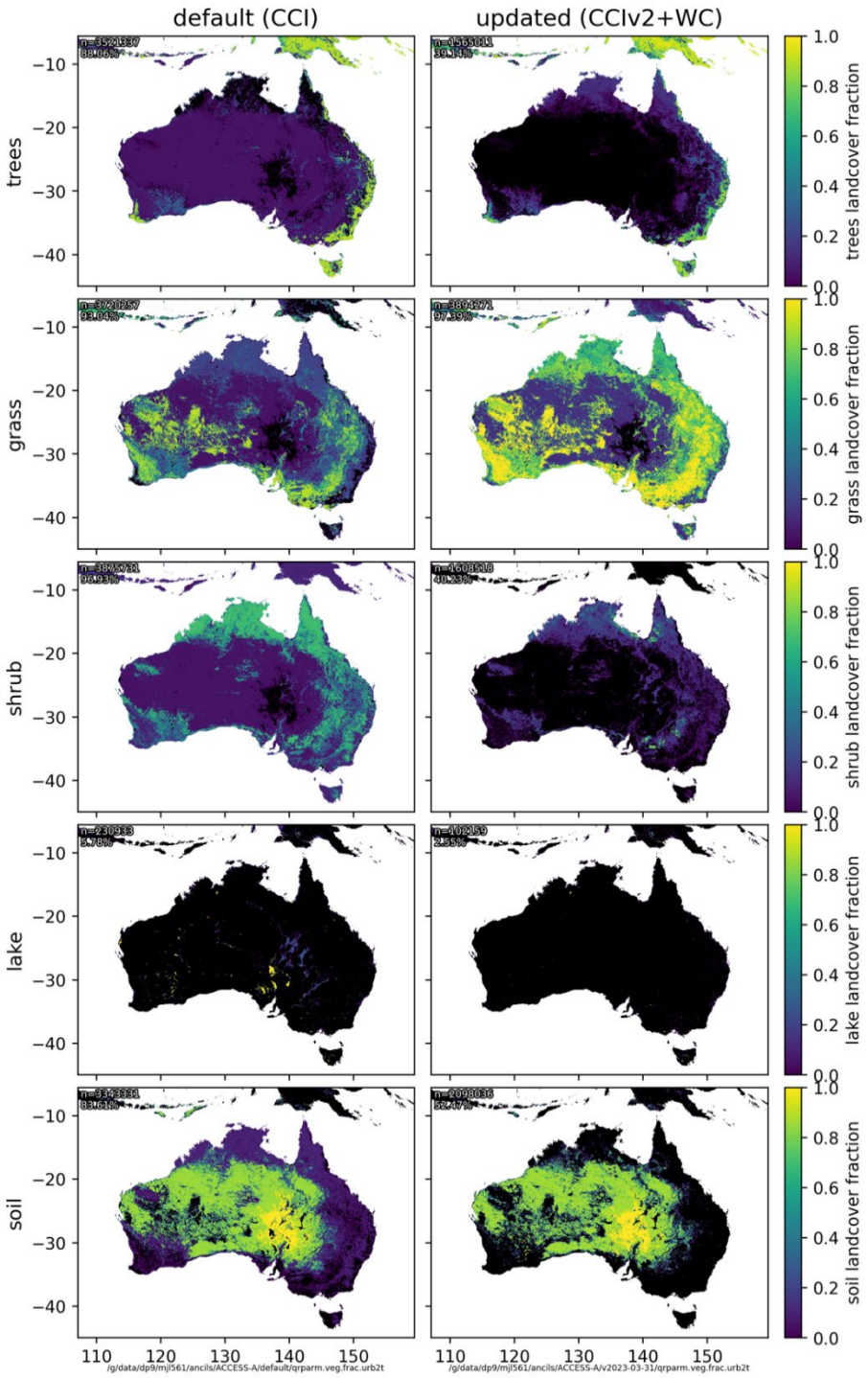


Figure 2: Comparison of land use from CCI (left) and CCIv2 with WorldCover (right).

## Urban land cover

Figure 3 compares 1.5 km horizontal grid length urban impervious fractions derived from various global datasets alongside very high resolution (2 m) land cover data for Sydney (Lipson et al., 2022) upscaled to match ACCESS-A grids. Compared with the 2 m data, CCI, IGBP and CCIv2 derived ancillaries significantly overestimate impervious urban cover and underestimate its spatial variability across Sydney. Ancillaries from an alternative global dataset, the 10 m resolution ESA produced WorldCover 2020 v100 (Zanaga et al., 2020) better represents impervious urban cover from the low-density fringes to the high-density urban core (Figure 3, right panel). While WorldCover underrepresents impervious fraction in highly vegetated areas (e.g. northern Sydney suburbs) it has significantly lower overall errors than other datasets. For ACCESS-A, we therefore use WorldCover for urban areas (with CCIv2 elsewhere).

WorldCover includes 10 non-urban land types (e.g. trees, shrubs, water, ice etc) which can be mapped to JULES plant function types (PFT) (Table 1). In mapping WorldCover types to JULES PFTs, some conversions are straightforward (e.g. shrubland → shrubs). For others we draw on the CCI cross walking approach to partition WorldCover types into appropriate JULES PFTs. As the high resolution (10 m) WorldCover can distinguish small scale urban features it is less heavily reliant on cross-walking compared with CCI (300 m). WorldCover data replaces CCIv2 in any ACCESS-A grid with urban fraction greater than 0.01.

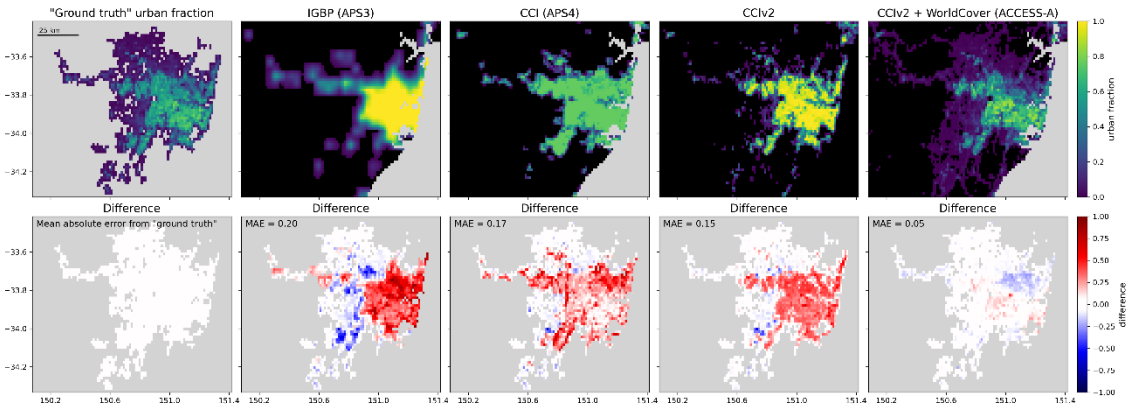


Figure 3: Upper panels show the urban impervious fraction for Sydney from a 2m resolution dataset (Lipson et al. 2022) and various global datasets. Lower panels show the differences in urban fraction from the 2m dataset.

Table 1: Mapping of ESA WorldCover categories to JULES. WorldCover is used in grid cells with > 0.01 urban fraction.

| **WorldCover type** | **JULES plant function type (PFT)** |
|---|---|
| Tree cover | trees (later partitioned into broad leaf and needle leaf trees using CCI proportions in the corresponding grid) |
| Shrubland | shrub |
| Grassland | grass (later partitioned into C3 and C4 grass) |
| Cropland | grass (later partitioned into C3 and C4 grass) |
| Built-up | urban (later partitioned into roof and canyon) |
| Bare / sparse vegetation | soil |
| Snow and ice | ice |
| Permanent water bodies | water |
| Mangroves | 0.6 x trees, 0.2 x lake, 0.2 x grass |
| Herbaceous wetland | 0.4 x grass, 0.3 x lake, 0.15 x trees, 0.15 x shrubs |
| Moss and lichen | 0.8 x grass, 0.2 x soil |

### C3/C4 grass partitioning

JULES separately represents C3 and C4 grasses, while CCI and CCIv2 do not. In ACCESS-A, the 250 m Australian C4 grass dataset from Donohue (2023) is used to partition C3 and C4 grasses. Noting that grasses on non-Australian land masses are partitioned using the ISLSCP II global 1-degree C4 percentage dataset (Still et al., 2009).

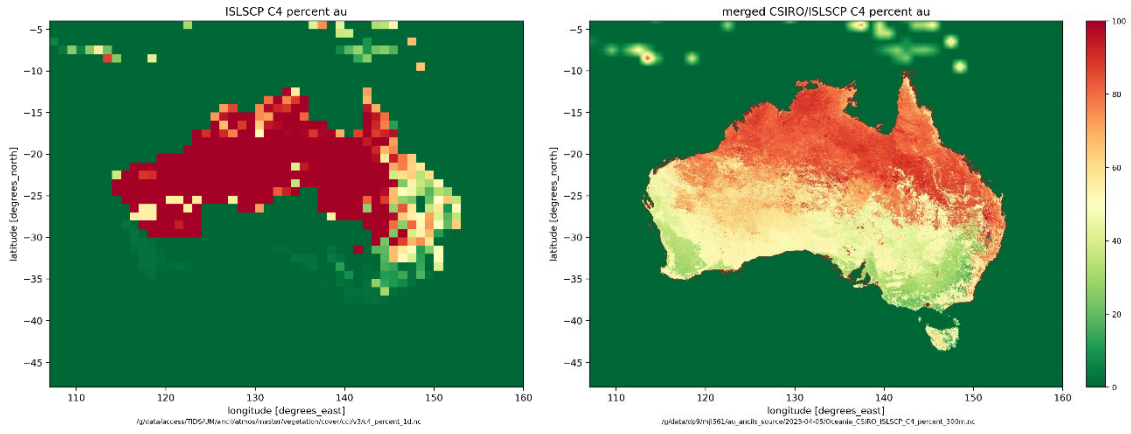


Figure 4: Datasets used to partition grass into C3/C4 types. Left is ISLCP II C4 (Still et al. 2009) and right the Australian C4 grass dataset (Donohue 2023).

## 2.2 RAL3.1 science configuration

The RAL3.1 configuration of the UM uses the ENDGame dynamical core, which is a semi-implicit semi-Lagrangian dynamical formulation that solves the non-hydrostatic, fully compressible deep-atmosphere equations of motion (Wood et al, 2014). A modification made to the semi-Lagrangian advection scheme is the implementation of a "fountain buster" scheme, which adds the missing effects of convergent in-flow and suppresses single grid points with overly intense updrafts. RAL3.1 extends the use of the Posteriori Monotone Filter to include potential temperature, as well as moist variables, with the impact of reducing dry grid point storms. For this km- and sub-km scale configuration of the model there is no parameterised convection.

The solar and terrestrial radiation is modelled using SOCRATES (Suite Of Community RAdiative Transfer codes based on Edwards and Slingo; Manners et al. 2023) where solar radiation is treated in six short-wave bands and thermal radiation in nine long-wave bands. Mixing due to turbulence is represented by the scale-aware blended scheme of Boutle et al. (2014) where the scheme blends the eddy diffusivity from the 1D vertical turbulent mixing scheme of Lock et al. (2000) with that from a 3D turbulent mixing scheme based on Smagorinsky (1963) as a function of the ratio of the grid length to a turbulent length scale. The boundary layer scheme configuration includes the additional Leonard term, which is an extra subgrid vertical flux that accounts for the tilting of horizontal flux into the vertical by horizontal gradients in vertical velocity and reduces the peak vertical velocities within updrafts (Hanley et al. 2019). RAL3.1 includes turbulent form drag over complex terrain, which has not been implemented in previous ACCESS-City model configurations.

The exchanges of mass, momentum and energy between the atmosphere and the underlying land and sea surfaces are represented using the Joint UK Land Environment Simulator (JULES; Best et al., 2011). To minimise changes between global and regional land surface settings, RAL3.1 includes numerous modifications to previously used regional JULES settings such as changes to vegetation momentum roughness lengths, use of Brookes and Corey soil hydraulics instead of van Genuchten, use of TopModel for soil heterogeneity, change in direction for super-saturated soil moisture, change to transpiration dependence on soil moisture and changes to sea-surface drag.

The largest model changes introduced in RAL3.1 are the new moist physics schemes, and these are documented in the following subsections.

### 2.2.1 CASIM: Cloud AeroSol Interacting Microphysics

Cloud microphysics schemes are a fundamental component of weather prediction models as they control the transfer of water between phases and hydrometeor species. This transfer of water impacts the intensity and timing of precipitation, cloud cover and its impact on radiative balance, and directly influences near surface weather such as temperature and wind.

RAL3.1 includes a new cloud microphysics scheme CASIM (Cloud AeroSol Interacting Microphysics; Field et al. 2023). CASIM is a more complex cloud microphysics scheme

than has been used in previous ACCESS numerical weather prediction models, and is configured as a double moment scheme predicting both the mass mixing ratios and number concentrations of five hydrometeor species (cloud, rain, ice, snow and graupel). Moving from a single to a double moment microphysics scheme has shown benefits particularly in the areal coverage of lighter precipitation, which has been linked to differences in rain evaporation (Morrison et al. 2009).

The implementation of CASIM in RAL3.1 does not include the aerosol activation or aerosol processing component of the scheme. Instead, the in-cloud droplet number concentration is prescribed. Fixing the droplet number, however, does not lead to lack of variability in the rain number concentration and rain drop sizes, fall speeds and evaporation rates. The rain number concentrations vary by orders of magnitude due to the conversion of cloud water to rain through autoconversion and accretion. The particle size distributions for each hydrometeor species are represented by a generalised gamma function with fixed shape parameter (Field et al. 2023).

### 2.2.2 Bimodal cloud cover scheme

Cloud cover, or cloud fraction, schemes represent subgrid cloud variability rather than assuming model grid boxes to be completely overcast or fully clear. Even for km-scale and sub-km scale simulations, the representation of radiation, fog and near surface temperatures have been shown to be improved with a cloud cover scheme (e.g. Boutle et al. 2016).

The ACCESS-City models use either the Smith diagnostic cloud cover scheme in the midlatitude domains or the PC2 (prognostic cloud prognostic condensate) scheme in the tropical domains. With RAL3.1 being a unified configuration that can be applied in both midlatitude and tropical domains, a different cloud cover scheme has been chosen for this model configuration. This new bimodal scheme (Van Weverberg et al. 2021) is based on the Smith diagnostic cloud cover scheme used in the regional midlatitude configuration, which uses a unimodal, non-skewed subgrid saturation-departure distribution to diagnose partial cloud cover. The bimodal scheme improves on the physical realism of the Smith scheme by identifying entrainment zones associated with strong temperature inversions and uses moist and dry Gaussian modes to represent the subgrid conditions for grid boxes in the entrainment zone. The cloud water content and cloud fraction are then diagnosed from the mean and width of the Gaussian modes that are inferred from the turbulent characteristics including the turbulent kinetic energy and a scale-aware mixing length. This results in greater cloud cover for liquid clouds and removes the need for an additional empirically based bias correction that is used with the Smith scheme.

### 2.2.3 MORUSES urban scheme

Using RAL3, ACCESS-A incorporates MORUSES (Met Office – Reading Urban Surface Exchange Scheme), a more complex urban scheme which parameterises the effects of varying building geometry on surface energy and momentum fluxes (Porson et al., 2010). MORUSES represents the impervious surfaces of urban areas as a composite of two

tiles: roof and canyon. Canyon tiles are intended to capture processes between buildings, where air flow experiences greater resistance, larger material surface area increases thermal inertia, more shortwave radiation is absorbed within street canyons, and less longwave radiation escapes to the atmosphere (Best et al., 2011).

The urban morphology inputs required by MORUSES are:

- canyon-width ratio (to partition the urban tile into roof and canyon tiles)
- canyon aspect ratio (to parameterise canyon thermal and radiative properties)
- building height (to parameterise roof and canyon tile roughness length and displacement heights for heat and momentum)

For ACCESS-A these urban morphology ancillaries are generated using predefined empirical polynomial relations derived from building-resolving (~1 m) 3D data from London, UK (Bohnenstengel et al., 2011). These empirical relations have been applied outside the London training area for lower density UK cities and have benefitted model performance there compared with the one-tile scheme (Hertwig et al., 2020).

### 2.2.4 Visibility diagnostics

While the visibility diagnostic remains essentially the same to previous configurations, one big improvement in RAL3.1 is the use of climatological aerosols as input to the aerosol mass mixing ratio ($a_m$) used in the diagnostic. Previously, a single constant number (a default of 10 μg/kg) was used outside of the UK. This number was adjusted to 15 μg/kg in APS3 to compensate for visibilities being generally too high over Australia. In highly polluted regions (like India) the value was typically set to 200 μg/kg. Note that the $a_m$ was just a single number, so there could be no variance across a model domain. With the use of climatological aerosols, the $a_m$ used in the visibility calculations now have a more realistic spatial variance. That said, the climatological aerosol ancillary file is static, and short-term acute sources of pollution will not be captured in the $a_m$ used for the visibility calculations. Australia has climatological clean air, which leads to higher visibilities in general.

### 2.2.5 Interactive buoyancy in surface exchange

An issue identified in RAL3.1 simulations is the rare occurrence of single grid points with very warm near-surface temperatures. This issue had been noticed previously in global model simulations using GAL8 (Global Atmosphere and Land 8 configuration) and traced to the surface exchange Monin-Obukhov similarity iteration using the buoyancy from the previous timestep. The surface exchange coefficients depend on the atmospheric stability, and when the stability changes from one timestep to the next this can lead to unrealistically large surface heating. The solution is to introduce an interactive buoyancy calculation within the exchange coefficient iteration. This fix to the hot spots was extensively tested with ACCESS-A and as the impact on forecast accuracy was near neutral, this fix had been adopted for the ACCESS-A science configuration. The RAL3.1 configuration plus this hot spot fix has subsequently been released by the Met Office as RAL3.2.

# 3. Case study evaluation

Two approaches have been used to aid the development of the ACCESS-A model and test the science configuration: case studies and short trials for different seasons. While verification of short trials gives a broad understanding of the model's general performance and systematic biases, case study evaluation provides insight into specific events to understand how well the model captures meteorological phenomena and ensures the model will provide reliable forecast guidance for high impact weather. Details of the case studies are documented in Table 2.

The case studies use initial and boundary conditions from the operational Met Office global model OS43 that uses the GA7.2/GL8.1 science configuration documented in Walters et al. (2019). The timestep of ACCESS-A is 60 sec, with the radiation scheme called every 15 minutes with 5-minute cloud updates. The boundary conditions are updated every hour.

The Regional Evaluation Suite (RES) was used for verification of the case studies and trials. RES contains a set of tools for diagnostic evaluation and objective verification of regional model simulations. RES verification uses the HiRA (High Resolution Assessment) framework (Mittermaier 2014), which uses a single-observation-neighbourhood-forecast approach. HiRA was developed to appropriately compare km-scale models with global models, recognising that convective-scale models usually provide more realistic features than coarser-resolution models, however, verifying such nonlinear and sometimes rapidly evolving forecasts at a grid scale around observation sites is challenging. RES uses the Bureau of Meteorology's surface weather observations and the GPM-IMERG satellite-derived rainfall product (Huffman et al. 2019). Additional evaluation was completed for specific cases depending on the focus of the assessment (see last column Table 2).

Table 2: Details of the case studies evaluated.

| Event | Date model initialised | Description |
|---|---|---|
| TC Seroja | 2021-04-10 00Z | Test the impact of strong inflow on the western boundary. |
| TC Uesi | 2020-02-13 00Z | Test the impact of strong inflow on the eastern boundary. |
| PNG hailstorm | 2019-12-25 00Z | Test the northern boundary stability associated with steep PNG topography. |
| East Coast flood | Every 6 hours 2021-03-17 06Z to 2021-03-22 18Z | Assess the model's performance to simulate convection and heavy rainfall. |

| | | |
|---|---|---|
| East Coast low pressure system | Every 6-hours 2020-07-25 00Z to 2020-07-26 00Z | Assess the model's performance to simulate convection and heavy rainfall. |
| Perth fog | 2017-08-29 00Z | Assess the model's ability to capture fog processes and low visibility. |
| Extreme heat | 2020-01-02 18Z | Test land cover ancillary and MORUSES urban scheme. |
| Extreme winter weather | 2021-06-09 00Z | Assess the model's performance to simulate unusually cold weather with strong wind and snow. |
| Brisbane hailstorm | 2020-10-30 00Z | Assess the model's representation of thunderstorms, including updraft helicity and lightning. |

## 3.1 TC Seroja

To test the impact of strong inflow on the western boundary of the domain, a case study was run for 48 hours during the latter part of Severe Tropical Cyclone (TC) Seroja. Seroja started as a slow moving tropical low near Indonesia on 2 April 2021, which intensified to a tropical cyclone on 5 April. It interacted with TC Odette during 8 and 9 April, intensifying Seroja while Odette was weakened and eventually dissipated. By 8am (0000 UTC) on 10 April, Seroja was classified as a category 2 system near the western boundary of the ACCESS-A domain where it took a sharp turn and continued to move into the domain on a south-easterly trajectory and intensifying before crossing the WA coast near Kalbarri as a category 3 TC. Figure 5 shows the official track and intensity map of TC Seroja. The image, together with a more complete description of the event can also be found at http://www.bom.gov.au/cyclone/history/seroja.shtml.

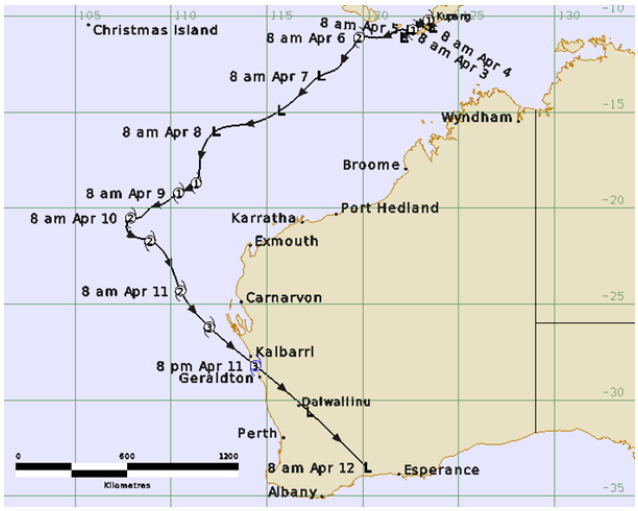


Figure 5: Official track and intensity of TC Seroja. Image extracted from http://www.bom.gov.au/cyclone/history/seroja.shtml.

ACCESS-A was initialised on 0000 UTC 10 April 2021, when TC Seroja was near the western boundary, bringing strong winds across the boundary into the domain. ACCESS-A simulated the event well, with a good timing and location of TC Seroja at landfall, though the minimum intensity was underestimated (Figure 6).

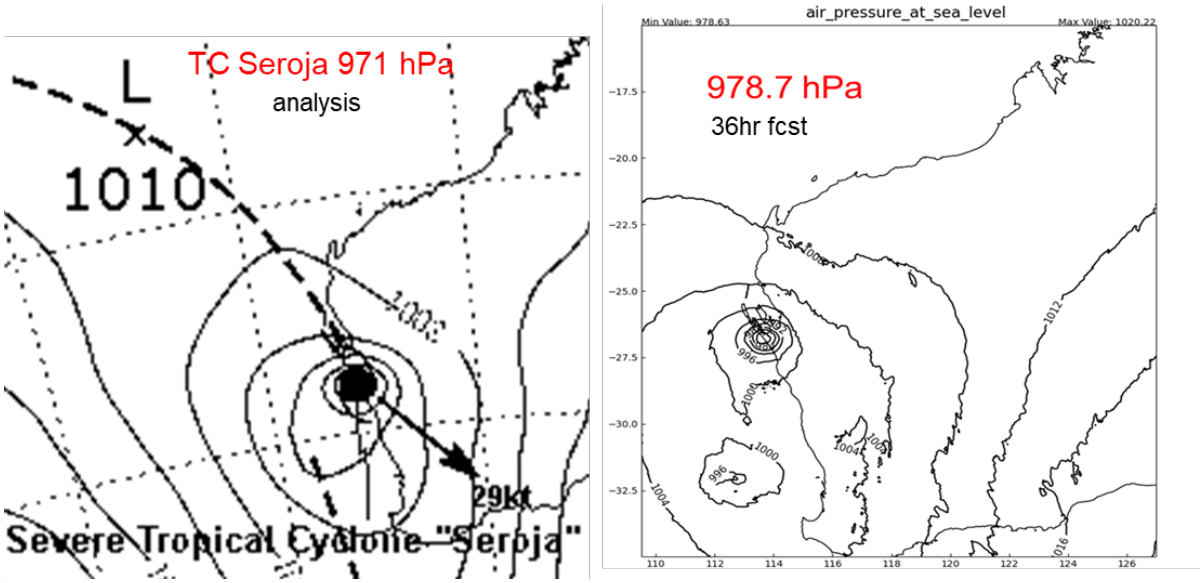


Figure 6: MSLP analysis (left) and ACCESS-A 36-hour forecast (right) for 1200 UTC 11 April 2021, when TC Seroja crossed the WA coast.

Figure 7 shows the region over which the Seroja case study was verified using RES, as well as a time series of the areal mean precipitation rate for ACCESS-A (dark blue) and GPM (light blue). The rainfall compared well against the satellite rain, although ACCESS-A missed the peak rain rates.

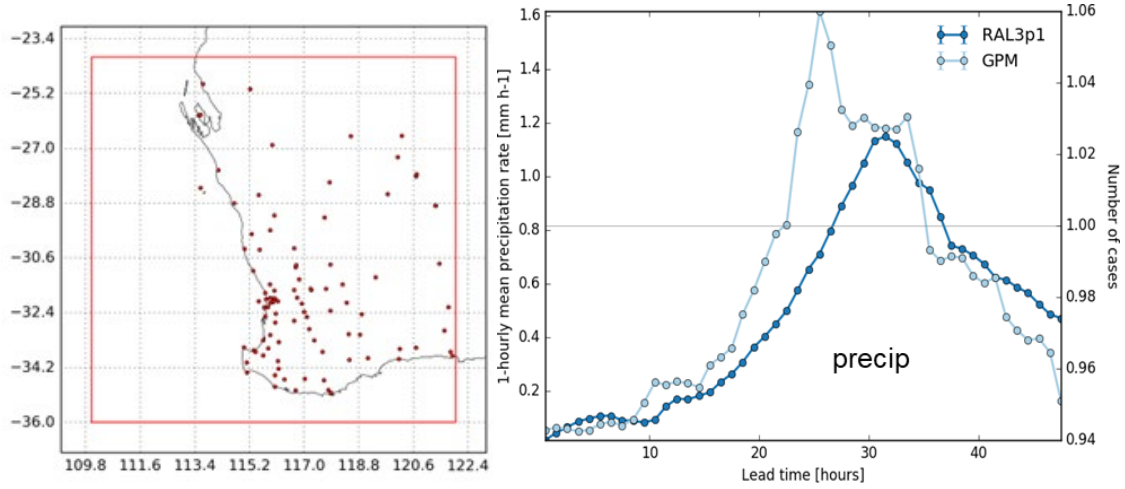


Figure 7: RES verification area (left) and areal mean hourly precipitation rate of ACCESS-A (dark blue) and GPM satellite (light blue).

Overall, RES verification shows good general agreement between the model and observations. The 10m wind speeds (Figure 8) were quite good, although ACCESS-A was biased slightly low.

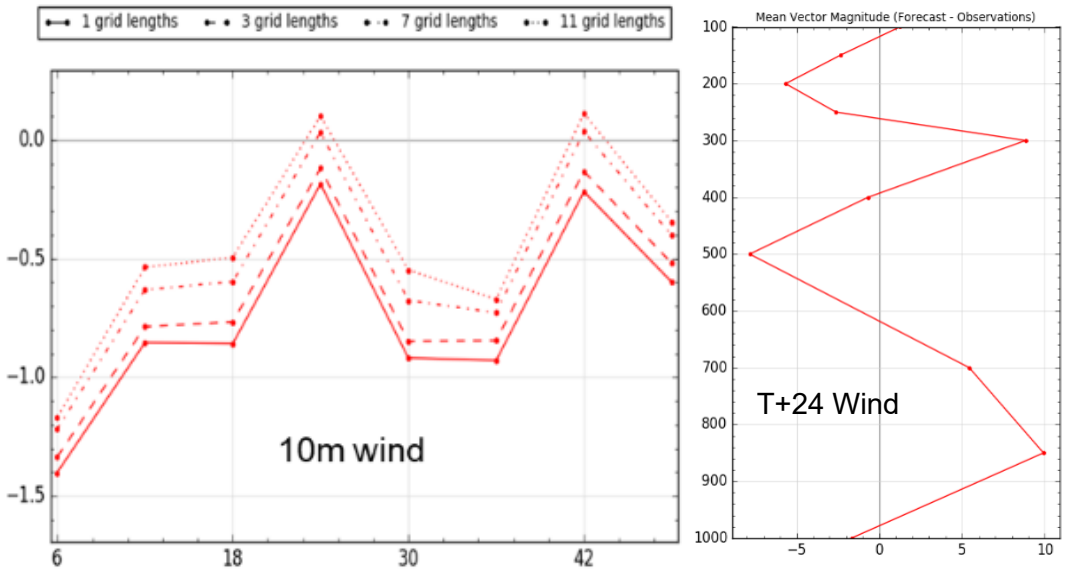


Figure 8: Areal mean error of the 10m wind speed (m/s) with lead time (left) and the mean vector magnitude of the wind profile (on pressure levels) at 0000 UTC 20210411 (right).

## 3.2 TC Uesi

Tropical Cyclone Uesi formed south of the Solomon Islands on 7 February 2020, reaching category 3 intensity west of New Caledonia by 11 February before weakening and transitioning to a sub-tropical system on 13 February, see Figure 9 (Grant & Courtney, 2023). At this stage, the system was close to the outer edge of the variable resolution domain of ACCESS-A. This case study was conducted to ensure that high inflows on the eastern boundary did not lead to model instabilities. The model was initialised on 2020-02-13 00Z and successfully completed a 48-hour forecast with no indication of instabilities developing.

Figure 10 shows the MSLP analysis (top panel) valid at 2020-02-14 00Z, with the depth of the low approximately 978 hPa. The bottom left panel shows the 24-hour MSLP forecast from ACCESS-A's uniform grid over a south-eastern subdomain that stretches to the eastern boundary. The bottom right panel shows that Uesi entered the variable-resolution grid of ACCESS-A with a minimum pressure of 976.7 hPa, closely matching the official MSLP analysis. Due to the region's proximity to the lateral boundary, the simulation here is strongly influenced by the driving model, making the minimum pressure value from ACCESS-A heavily dependent on the global model's representation.

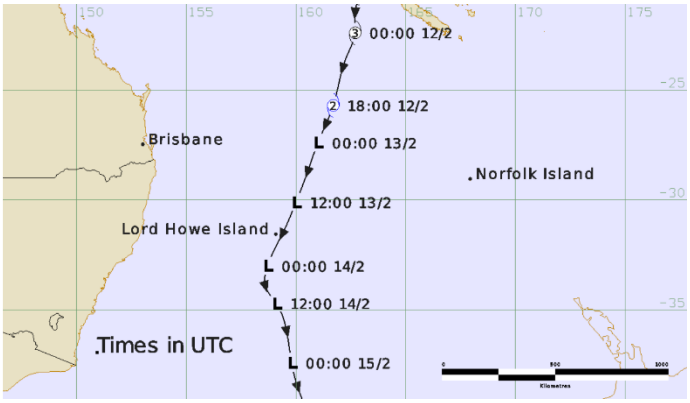


Figure 9: Best track of TC Uesi from Grant & Courtney, 2023.

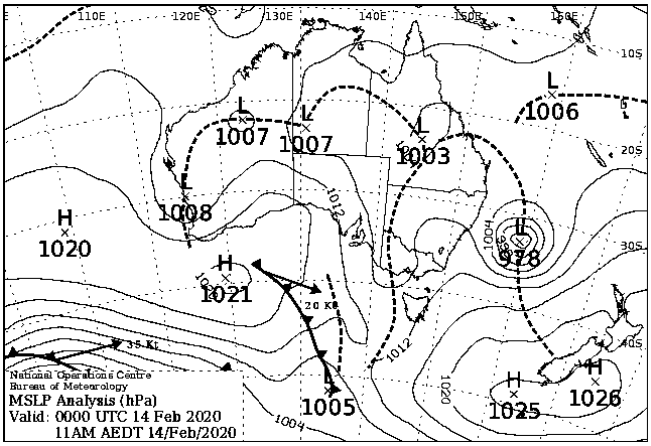

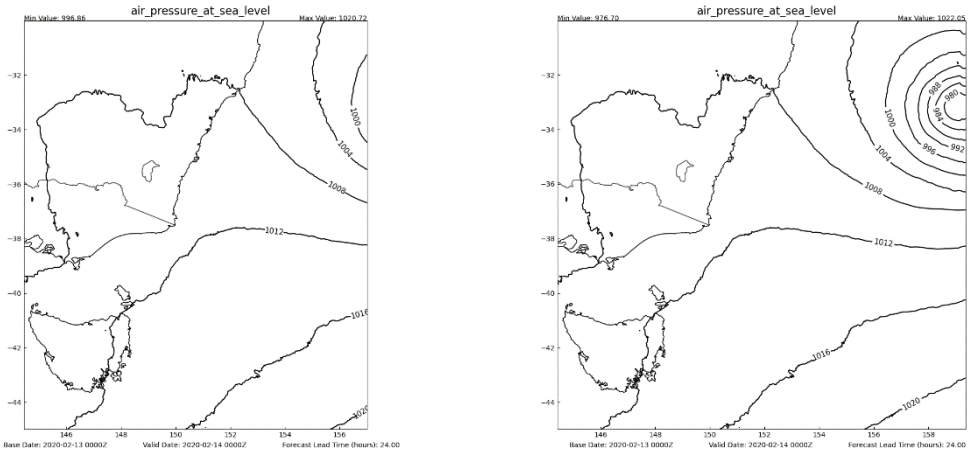


Figure 10: The MSLP analysis (top panel – previous page) valid at 2020-02-14 00Z. The bottom left panel shows the 24-hour forecast of MSLP from ACCESS-A's uniform grid over a south-east subdomain, also valid at 2020-02-14 00Z. The variable grid equivalent is shown in the bottom right panel.

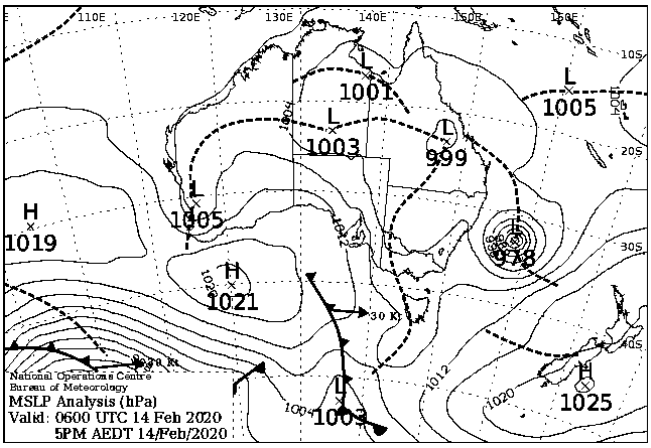


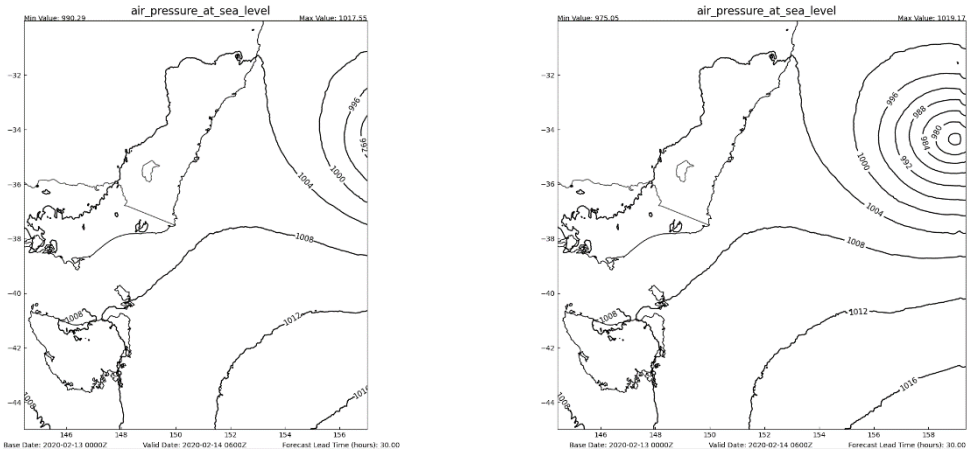


Figure 11: Same format as Figure 10, valid at 2020-02-14 06Z. 30-hour forecasts from ACCESS-A.

Similar images are presented in Figure 11, valid at 2020-02-14 06Z, with ACCESS-A showing the 30-hour forecasts. Again, Uesi remains outside of the ACCESS-A uniform grid, although it has moved closer to the eastern edge of the uniform grid. At this time the cyclone's centre has entered the variable resolution grid (bottom right panel). The 30-hour ACCESS-A forecast of Uesi's minimum pressure is 975 hPa, which is 3hPa deeper than the MSLP analysis (top panel), but compares very well to the best track pressure of 976 hPa (Grant & Courtney, 2023). Again, the proximity of the cyclone’s centre to the domain boundary means the forecasted depth of the low is strongly influenced by the driving model.

Both Figure 10 and Figure 11 reveal signs of boundary effects in the variable resolution part of the model grid, evident as kinks in the isobars near the eastern edge. These artifacts are confined to the variable portion of the grid, as the uniform grid panels in both figures do not exhibit such distortions. To assess whether boundary effects extend into the uniform inner domain, additional variables have been plotted.

Figure 12 shows the top of atmosphere outgoing longwave radiation (TOA OLR) from the uniform ACCESS-A grid (top row) and the variable grid (middle row). Himawari-8 scaled radiance images are shown on the bottom row. The left-hand column is valid at 2020-02-14 00Z and the right hand column is valid at 2020-2-14 06Z, which match the valid times of Figure 10 and Figure 11 respectively. The images in the middle rows clearly show the boundary artefacts. Along the eastern edges of the plots there are lateral boundary spin up issues, as well as the visible discontinuity in the fields bordering the eastern edge of the domain. These effects arise from the higher-resolution ACCESS-A model adjusting to the coarser-resolution boundary forcing provided by the global model. The mismatch in spatial scales leads to the ACCESS-A model needing to spin up finer-scale features that are not resolved in the driving data, resulting in artificial gradients and noise near the boundaries as the higher resolution model adjusts. Comparing these to the top row, there do not appear to be any lateral spin up or boundary artefacts in the uniform grid domain, indicating that the variable resolution grid design effectively deals with lateral boundary induced artifacts. Additionally, a qualitative comparison of the TOA OLR fields from ACCESS-A to the Himawari-8 scaled radiance shown in Figure 12 indicates that ACCESS-A forecast the major cloud features well, in particular the convection over Victoria at 2020-02-14 06Z.

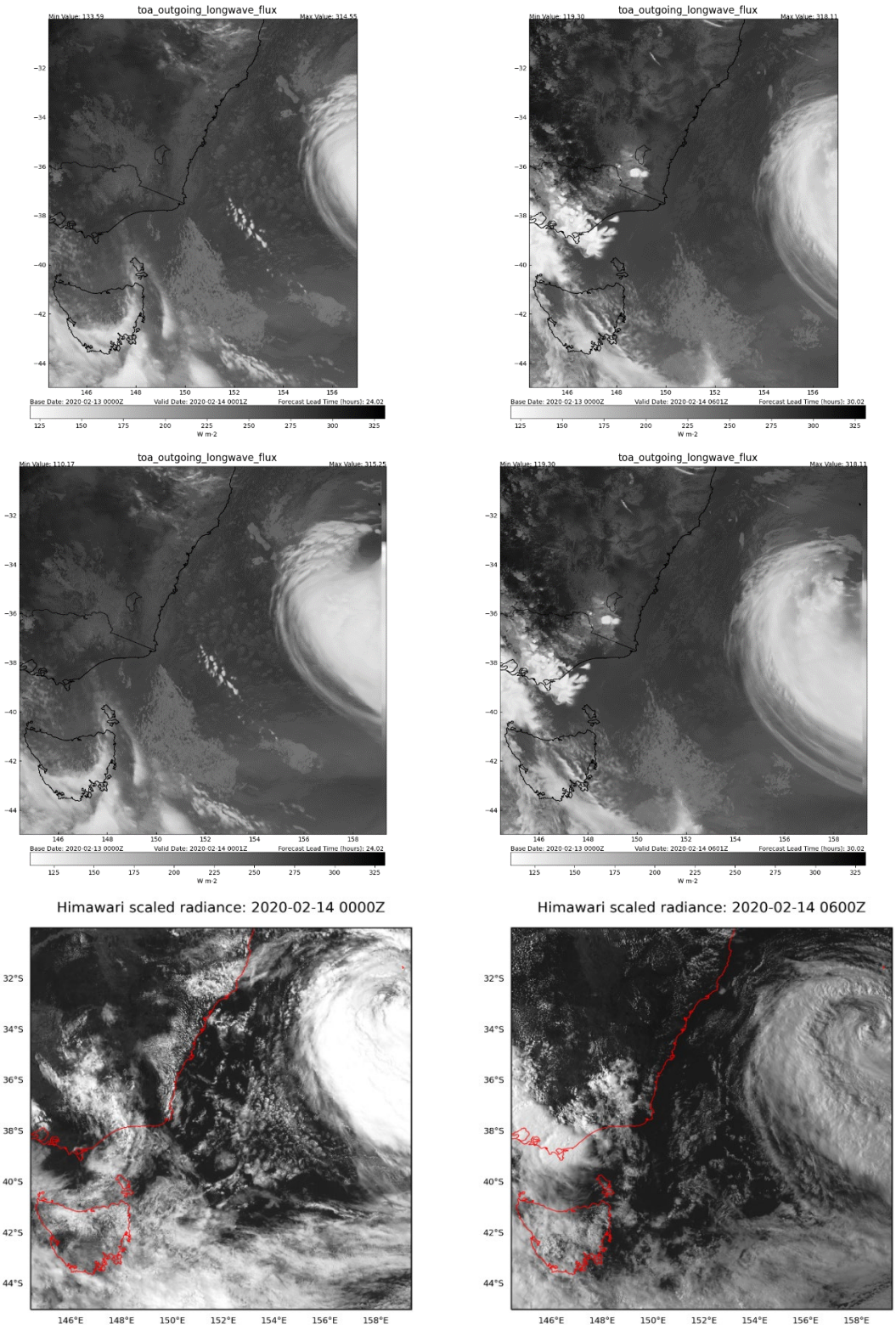


Figure 12: The top of the atmosphere outgoing longwave radiation (TOA OLR) for the uniform ACCESS-A grid (top panels) and the variable ACCESS-A grid (middle panels). The bottom panels show the scaled radiance from the Himawari-8 satellite. The images on the left are valid at 2020-02-14 00Z (matching Figure 10) and the images on the right are valid at 2020-02-14 06Z (matching Figure 11).

## 3.3 Papua New Guinea hailstorm

On Christmas Day 2019, a severe hailstorm occurred at Mt Hagen, in the Western Highlands province of Papua New Guinea (PNG). As the PNG Western Highlands are on the northern boundary of ACCESS-A, this event was used to test the model stability associated with the steep topography on the northern boundary. Testing using this case with an unstable atmosphere resulted in no model failures. RAL3.1 has improvements to the drag and cloud/latent heating, which leads to reduced horizontal and vertical winds and a more stable model than previous model versions where smoothing of steep topography was required to maintain model stability.

Furthermore, on visual examination of the cloud features (Figure 13), there is little evidence of the unrealistic high cloud features reported in other RAL3 evaluations and discussed in Section 5. In the spin up period (6 – 12 hours) there were hints of the somewhat binary cloud features with cloud fractions of 0 or 1 and sharp edges (Figure 13 top left), but the clouds in the rest of the simulation generally looked realistic (e.g. Figure 13 bottom left).

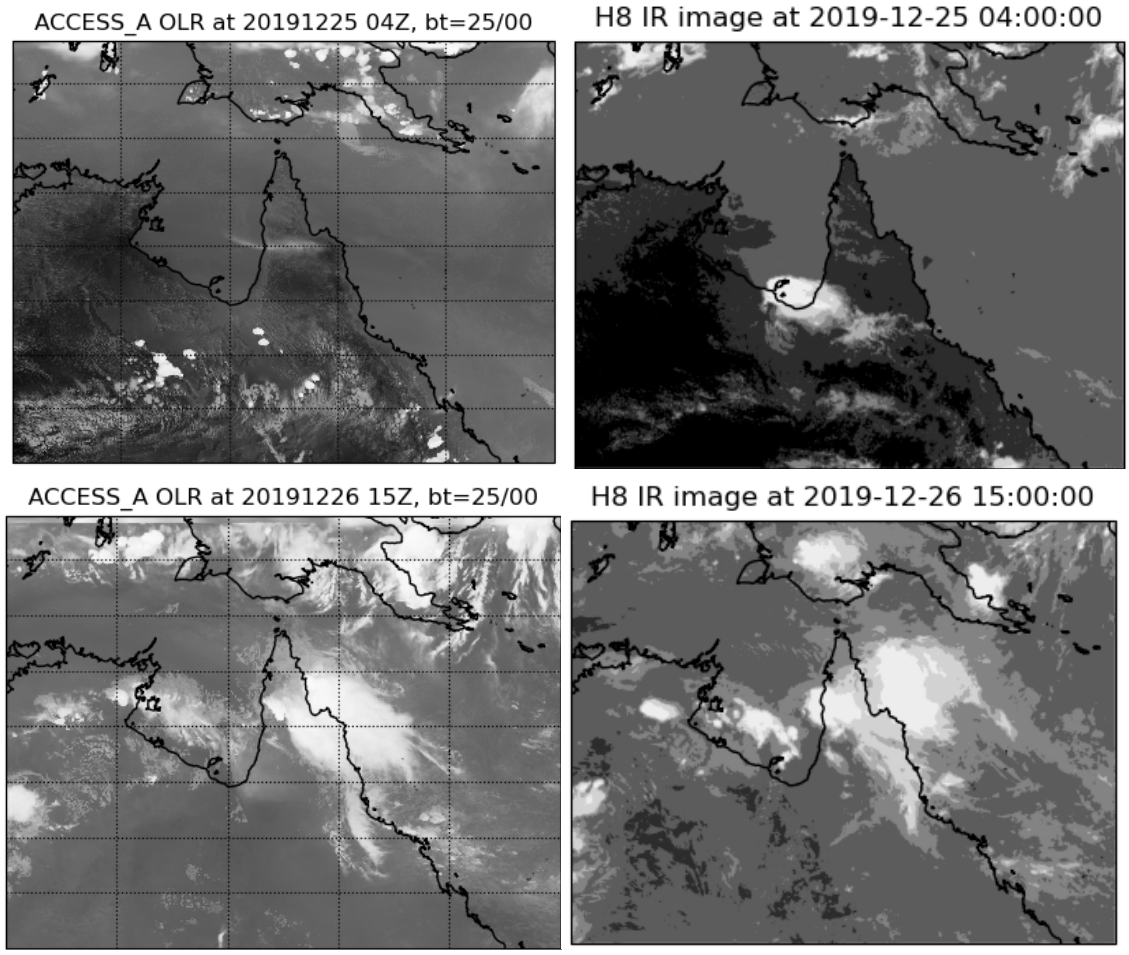


Figure 13: ACCESS-A Outgoing Longwave Radiation (left) and Himawari-8 infrared (right) images at 0400 UTC on 25 December 2019 (top) and 1500 UTC on 26 December 2019 (bottom). ACCESS-A base time is 0000 UTC 25 December 2019.

## 3.4 East Coast Flood

A major flood event impacted large parts of Australia in late March 2021, driven by heavy rainfall across inland NSW, northern SA, southern Queensland, and coastal NSW. Victoria and Tasmania also saw significant rain, with the most intense falls along the NSW coast. From March 17, a slow-moving blocking high southwest of Tasmania directed moist easterly winds over coastal NSW, persisting for about a week. Troughs and a shallow coastal low on March 19–20 intensified rainfall, with some of the highest totals recorded during this period.

Separately, a low formed over central Australia on March 22, evolving into a system over southern Queensland and northern NSW by March 23. This enhanced north-easterly flows over southeastern NSW and tracked south through Victoria on March 24, reaching the Tasman Sea west of Tasmania by March 25.

Rainfall peaked on March 19 along the Mid North Coast, with heavy falls in Sydney on March 21–22, southeast Queensland on March 22–23, and the South Coast and eastern Victoria on March 24. Tasmania recorded its highest totals on March 25 as the low moved south of the island (Bureau of Meteorology, 2021).

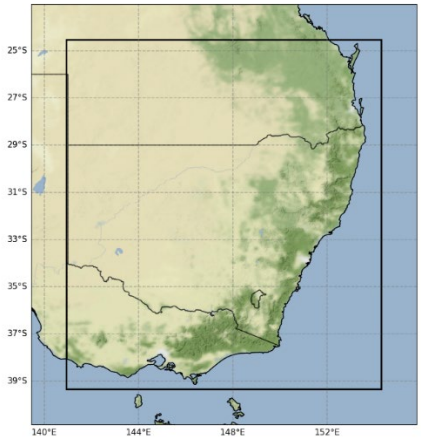


Figure 14: The black rectangle denotes the verification domain used for the March 2021 flooding event.

Table 3: Details of the East Coast Flood trial period.

| Start Cycle | Final Cycle | Number of cycles | Comments |
|---|---|---|---|
| 2021-03-17 06Z | 2021-03-22 18Z | 23 | 2021-03-17 00Z start dump missing |

To understand how well ACCESS-A performed throughout this event, a short trial was run (see Table 3 for details). Analysis of this event is concentrated on a south-east Australia domain, see Figure 14, that was heavily impacted.

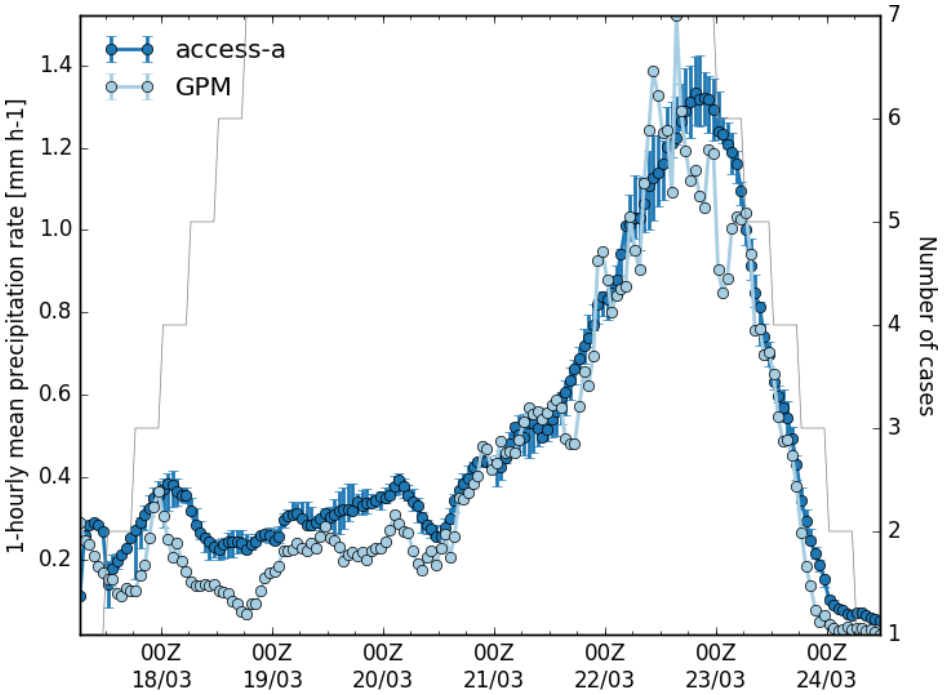


Figure 15: The hourly mean precipitation rate (mm/h). ACCESS-A is represented in dark blue, and the GPM observations are light blue.

Figure 15 shows the domain mean hourly precipitation rate from ACCESS-A and the GPM observations throughout the trial period. ACCESS-A captures the timing and magnitude of the increase, peak and decrease in the precipitation rate, doing particularly well from ~12Z on March 20 when the precipitation strongly increased until the end of the event.

Early in the event prior to the large increase in rainfall, ACCESS-A over forecast the domain mean precipitation rate. Looking at 6-hour rainfall accumulations in Figure 16 there appear to be two reasons for this over-estimation in precipitation. One reason is the excessive inland precipitation in the ACCESS-A forecast (top row), although we note that the area of heavy rain (20+ mm/6 hours) along the NSW coast is well forecast. The second reason is the spatial displacement of the main rain area. To illustrate this, the GPM plot on the lower right in Figure 16, is plotted over a larger spatial domain than the ACCESS-A forecast with the dashed black line indicating the verification domain. This shows that the main precipitation feature in ACCESS-A is over inland NSW, whereas the heaviest observed falls were bordering the verification domain.

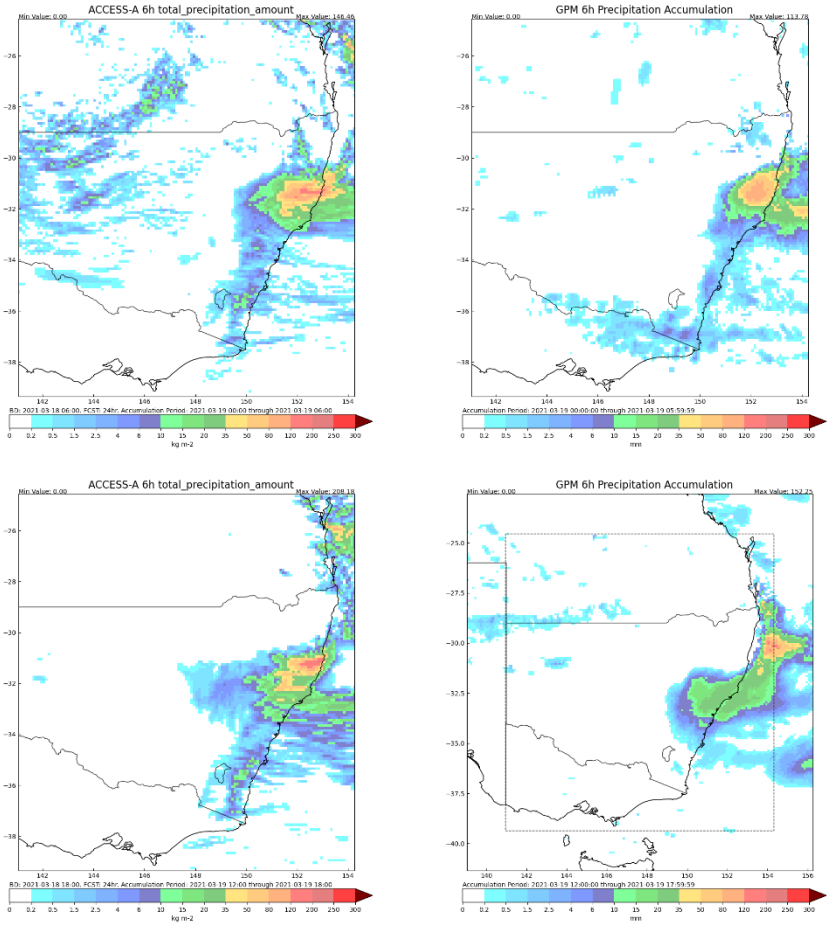


Figure 16: 6-hour precipitation accumulations from ACCESS-A (left hand column) and GPM (right hand column). These accumulations are valid at 2021-03-19 06Z for the top row and 2021-03-19 18Z for the bottom row. These are 24-hour forecast for ACCESS-A; basetime of 2020-03-18 06Z for the top row and 2020-03-18 18Z for the bottom panels. Note that bottom right GPM observations are plotted over a larger spatial extent with the dashed rectangle indicating the verification domain. See text for discussion.

Figure 17 shows the histogram of 1-hourly mean precipitation rates for ACCESS-A (dark blue) and GPM (light blue) in the top left panel. Throughout this event, ACCESS-A matched the observations for the lightest precipitation rates while slightly under-forecasting the occurrence of ~2 mm/hr precipitation rates. However, ACCESS-A over forecast the number of higher rainfall rates greater than 8 mm/hr. This is partially explained by situations such as that presented in the bottom right panel of Figure 16, which shows the heavy rain in the observations were on the border of the verification domain, as well as times where the model predicted heavy precipitation that was not observed, see Figure 18 for an example.

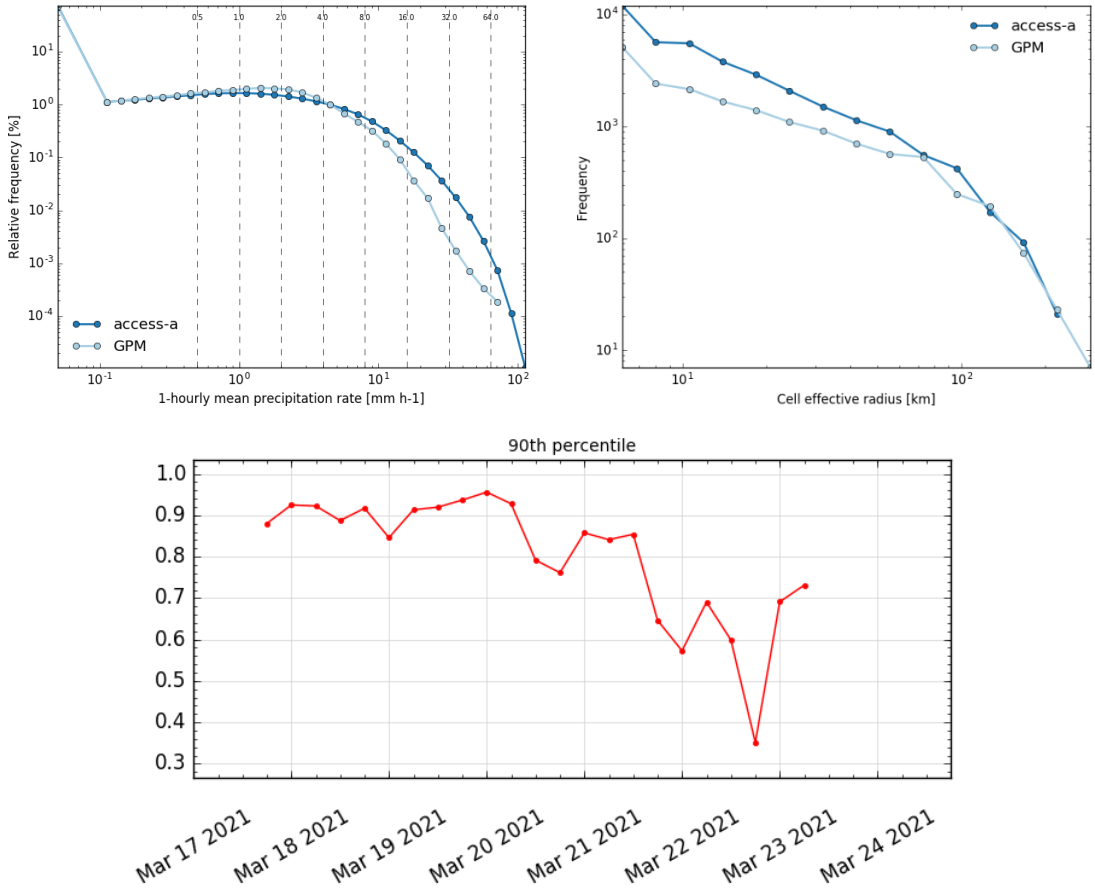


Figure 17: The top left panel shows the hourly mean precipitation rate histogram through the trial. The effective cell radii histogram for the 4 mm/hr precipitation rate is shown in the top right panel. The bottom panel shows the FSS for the 90$^{th}$ percentile precipitation rate for the 12-hour forecast lead time at the 37.5 km scale.

The cell size metric in the top right panel in Figure 17, shows that ACCESS-A produces too many small precipitating cells with of least 4 mm/hr compared to the GPM observations. This may indicate that the convection in ACCESS-A was not as well organised as was observed. However, the simulated cell sizes match the observations well for cell radii greater than 60 km.

The bottom panel in Figure 17 shows the Fractions Skill Score (FSS) (Roberts and Lean, 2008) of the 90$^{th}$ percentile precipitation rate throughout the event at the 37.5 km scale for the 12-hour forecast. Neighbourhood processing of 25 grid lengths is used to compare the 90$^{th}$ percentile of the GPM and ACCESS-A precipitation rates. The 90$^{th}$ percentile comparison allows an assessment of the highest precipitation rates throughout the event. The results show that ACCESS-A has very good skill in the first 4 days of the trial with FSS values greater than 0.8, before reducing from ~12Z on March 21, though still maintaining values greater than 0.6 in general. There is a marked reduction of FSS at 18Z on March 22. This is a result of ACCESS-A forecasting heavy precipitation in the vicinity of North Stradbroke Island (northeast corner of left panel in Figure 18), skewing the model's 90$^{th}$ percentile rate to larger values than observed.

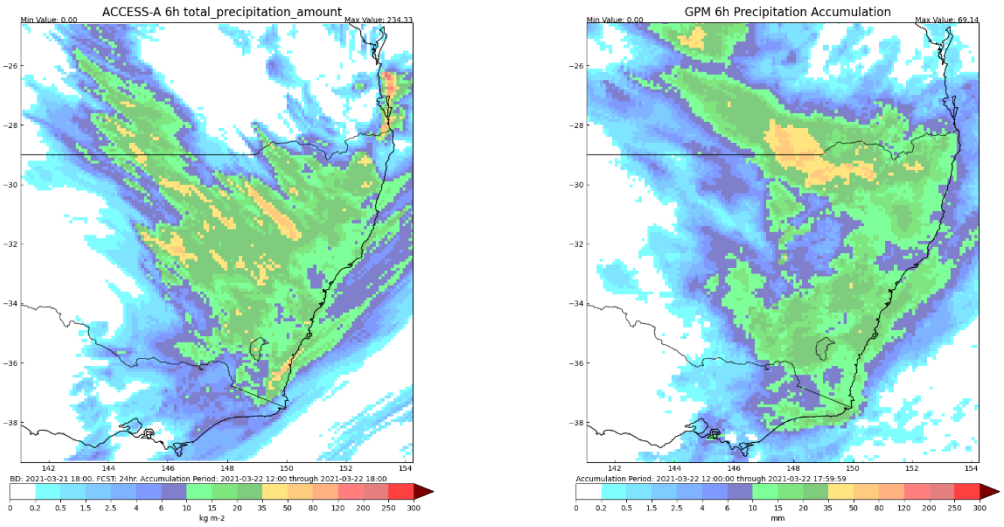


Figure 18: 6-hour precipitation valid at 2021-03-22 18Z from the 24-hour ACCESS-A forecast (left) and the GPM observations (right). Heavy precipitation forecast near North Stradbroke Island was not observed by GPM.

As well as assessing shorter time scale accumulations, it is also informative to examine longer accumulation periods. Figure 19 shows 24-hour accumulations from ACCESS-A on its native grid (top row), on the 0.1 x 0.1 degree GPM grid (middle row), along with the GPM observations (bottom row). The images in the left-hand column are valid at 2021-03-19 00Z and are 24-hour ACCESS-A forecasts. The images in the right-hand column are valid at 2021-03-20 00Z and are 48-hour ACCESS-A forecasts.

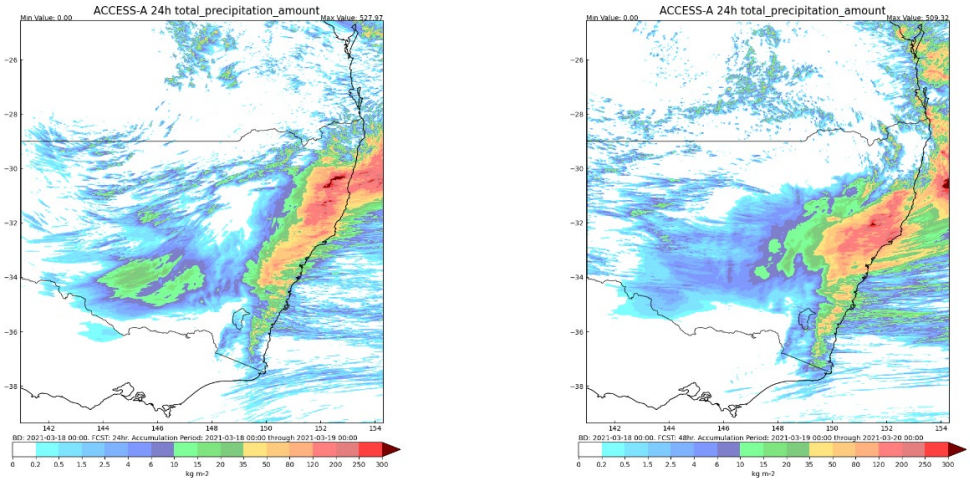

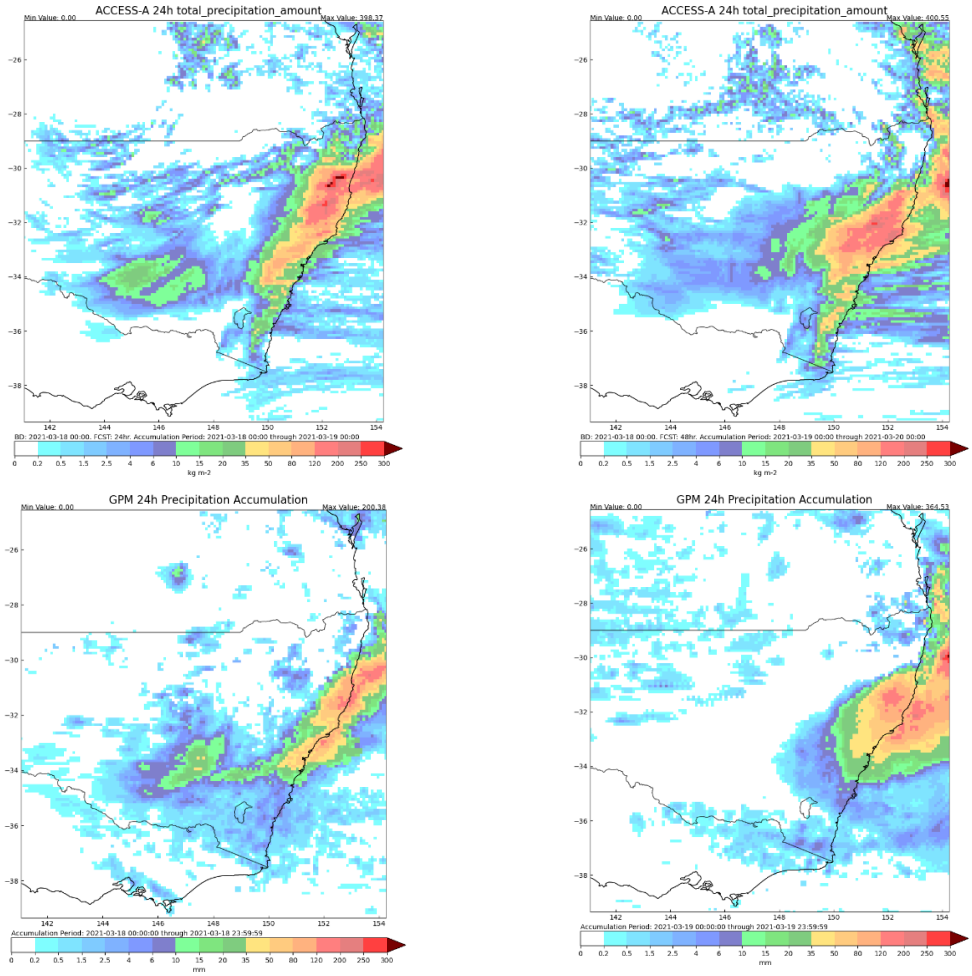


Figure 19: 24-hour precipitation accumulations from ACCESS-A on its native grid (top row – previous page), ACCESS-A on the GPM grid (middle row) and GPM observations on the bottom row. The accumulations are 24-hour forecasts from ACCESS-A valid at 2021-03-19 00Z (first column) and 48-hour forecasts valid at 2021-03-20 00Z (second column).

The top panel in the left-hand column of Figure 19 shows ACCESS-A forecasting large rainfall accumulations across coastal NSW, with peak accumulations north of the central coast and a 20+ mm band over southern central NSW. When plotted on the GPM grid (left-hand image of middle row) some of the highest accumulations are reduced. The GPM observations (bottom-left) recorded over 35 mm from central NSW extending northward, with the rainfall aligned along the coast. In contrast, ACCESS-A shifted precipitation inland, overestimating coastal coverage but capturing key high-rainfall areas. The southern inland rainfall feature in ACCESS-A appears slightly southwest of the observed location. Overall, despite overestimating extent and intensity, ACCESS-A effectively identified the regions impacted by large daily precipitation accumulations. The following day (Figure 19, right column), ACCESS-A (middle row, GPM grid) closely matched the regions of high observed rainfall (bottom row), though forecast totals were higher. The model predicted more rainfall along the southern NSW coast and generated broader regions of light inland precipitation than observed.

Figure 20 shows the mean error of 1.5m temperature (right) and 10m wind speed (left) as a function of lead time averaged over the trial period. The plots show the verification at the individual grid length (solid line) along with various neighbourhood sizes. The temperature verification shows ACCESS-A was warmer than the observations by < 0.3 degrees. Applying neighbourhood verification methods resulted in smaller mean errors with the 11 grid lengths recording the lowest mean error (dotted line). The 10m wind speed mean error (right-hand panel) increases with lead time with the impact of using larger neighbourhood sizes constant with lead time. In this case, the larger neighbourhood of 11 grid lengths produces a larger mean error from T + 18. The magnitude of these mean errors is typically small, within ~0.2 m/s of the observations.

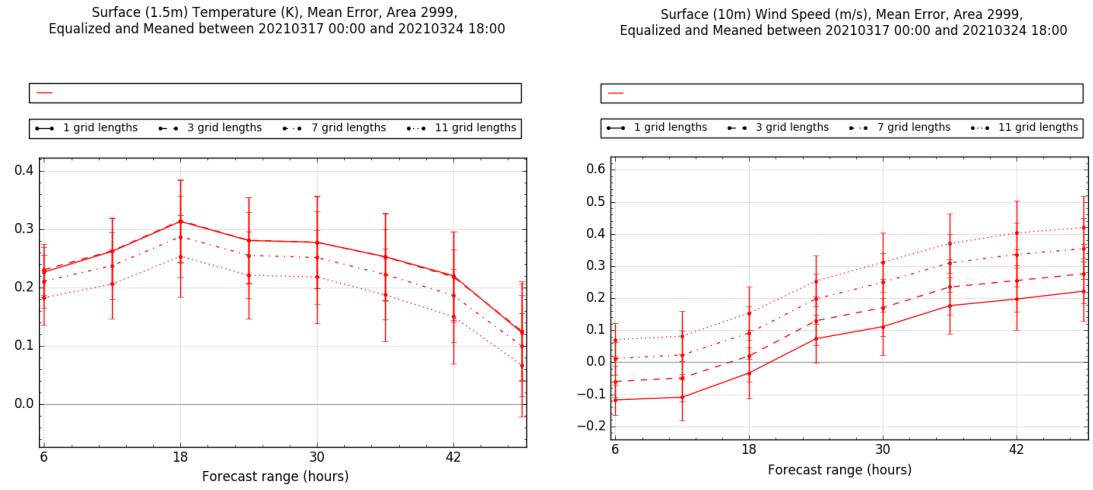


Figure 20: The mean error of 1.5m temperature and 10m wind speed throughout the trial period as a function of lead time.

## 3.5 East Coast Low Pressure System

On 24 July 2020, a low-pressure system formed off the Queensland coast. This low-pressure system subsequently deepened and moved south along the New South Wales coast from July 26 – 28. Newcastle and the South Coast district experienced flash flooding (Bureau of Meteorology, 2020b). To model the case study, ACCESS-A was run for five cycles, every 6-hours from 2020-07-25 00Z through to 2020-07-26 00Z (inclusive).

Figure 21 shows the hourly domain mean precipitation rate (top left, using the same domain as shown in Figure 14), hourly precipitation rate histogram (top right), effective cell radii for rates > 4 mm/hr (bottom left) and the 6-hour Fractions Skill Score (FSS) for the 24-hour forecast of the 90$^{th}$ percentile precipitation rate at the 37.5 km spatial scale. Concentrating on the domain mean precipitation rate (top left), ACCESS-A overestimated rainfall early in the event, matched the observations closely around 00Z on 2020-07-26, then underpredicted rainfall until 12Z on the 27$^{th}$ of July. The precipitation frequency histogram, top right of Figure 21, shows ACCESS-A matched the GPM observations very well throughout the event. The effective cell radii from ACCESS-A

matched the GPM observations reasonably well, however the higher frequencies in ACCESS-A, particularly for the small cell sizes, may indicate that the convection in ACCESS-A was not as organised as was observed. The 24-hour forecast FSS for the 90th percentile precipitation rate at the 37.5 km spatial scale from ACCESS-A was very good throughout the event with values between 0.86 and 0.97.

Figure 22 shows 6-hour accumulated precipitation forecasts and GPM observations for 26 July, when domain mean rates peaked. At 2020-07-26 06Z (top row) ACCESS-A predicted heavy rain over southern and central coastal NSW but underestimated totals, with some higher values offshore. The model also missed high rainfall accumulations along the northern NSW coast. 6-hours later (second row), ACCESS-A forecast high rainfall amounts near the central coast, aligning well with observations, though offshore accumulations were underestimated. This pattern continued in later forecasts (third and fourth rows), with consistent underestimation offshore and in southern NSW/eastern Victoria. Despite under forecasting domain mean rainfall rates, ACCESS-A provided reliable guidance on key impacted regions.

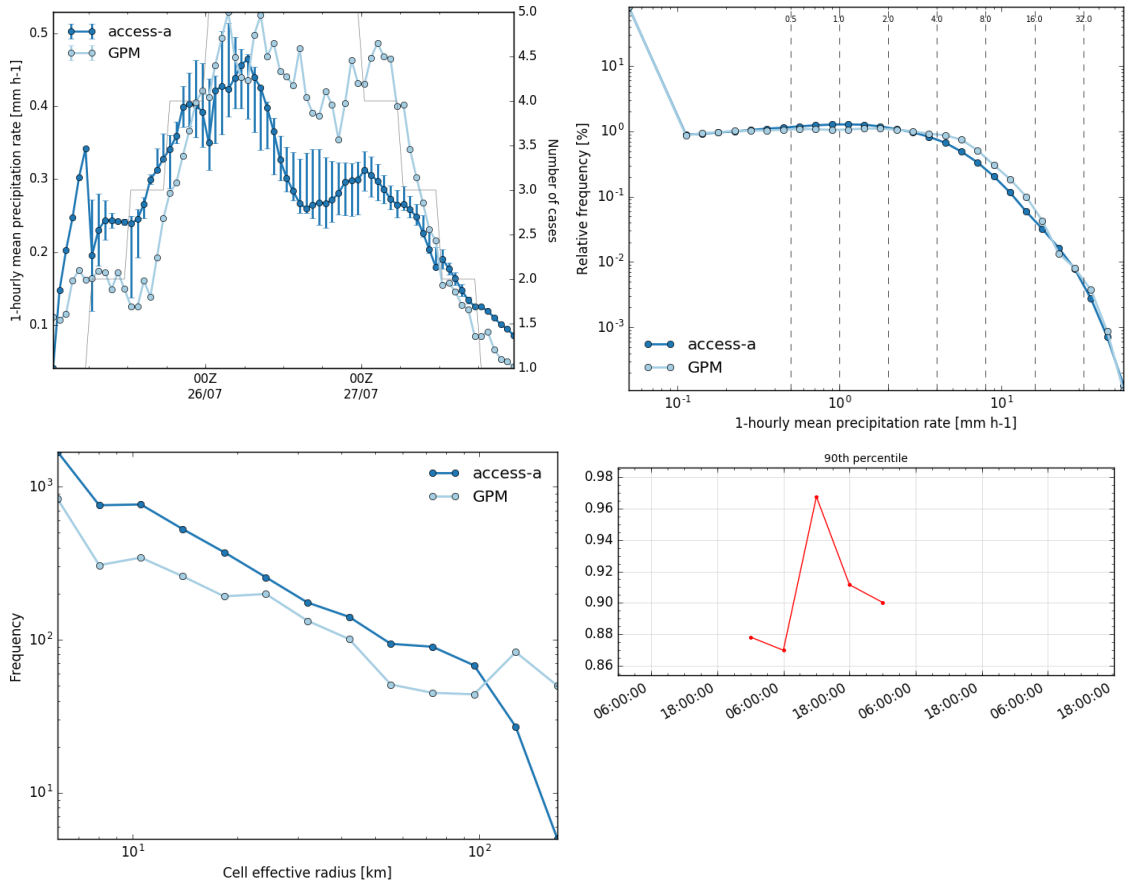


Figure 21: The mean areal precipitation rate (top left), the rainfall histogram (top right), the effective cell radii frequency plot for precipitation rates exceeding 4 mm/h (bottom left) and the Fractions Skill Score for the 90$^{th}$ percentile precipitation rate for the 37.5 km spatial scale.

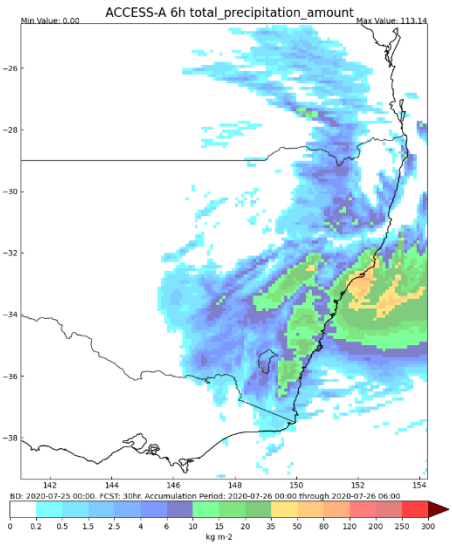
ACCESS-A 6h total_precipitation_amount
Min Value: 0.00
Max Value: 113.14
BD: 2020-07-25 00:00. FCST: 30hr. Accumulation Period: 2020-07-26 00:00 through 2020-07-26 06:00
kg m-2

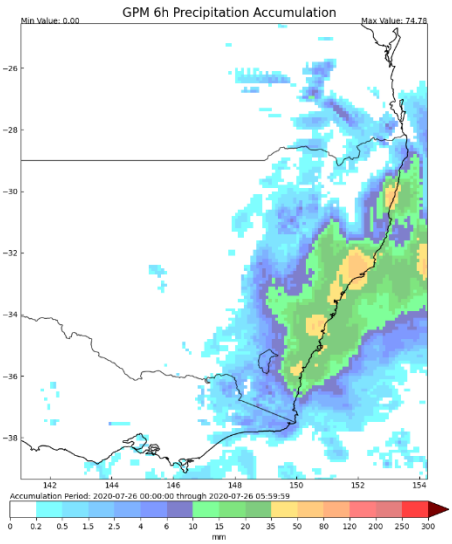
GPM 6h Precipitation Accumulation
Min Value: 0.00
Max Value: 74.78
Accumulation Period: 2020-07-26 00:00:00 through 2020-07-26 05:59:59
mm

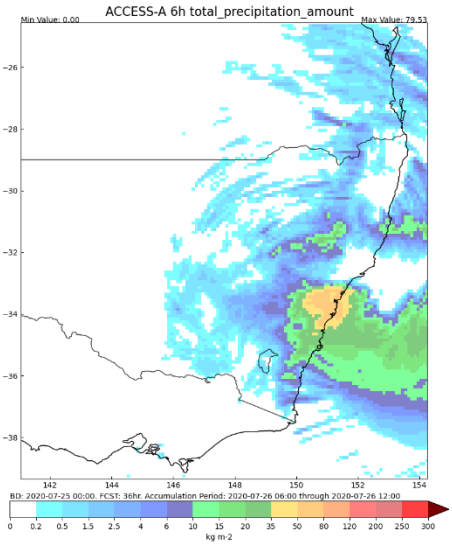
ACCESS-A 6h total_precipitation_amount
Min Value: 0.00
Max Value: 79.53
BD: 2020-07-25 00:00. FCST: 36hr. Accumulation Period: 2020-07-26 06:00 through 2020-07-26 12:00
kg m-2

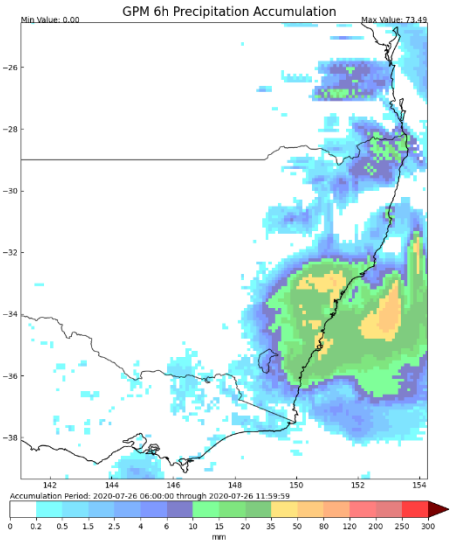
GPM 6h Precipitation Accumulation
Min Value: 0.00
Max Value: 73.49
Accumulation Period: 2020-07-26 06:00:00 through 2020-07-26 11:59:59
mm

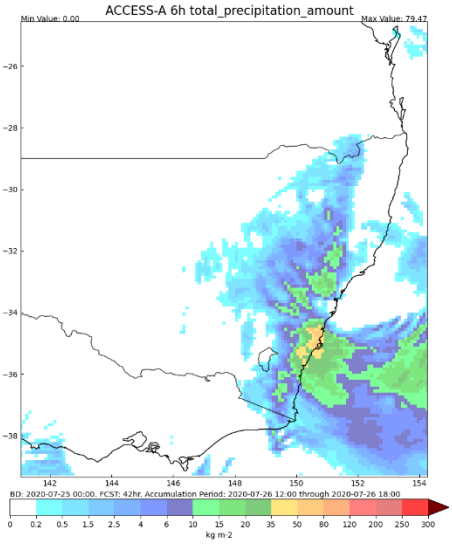
ACCESS-A 6h total_precipitation_amount
Min Value: 0.00
Max Value: 79.47
BD: 2020-07-25 00:00. FCST: 42hr. Accumulation Period: 2020-07-26 12:00 through 2020-07-26 18:00
kg m-2

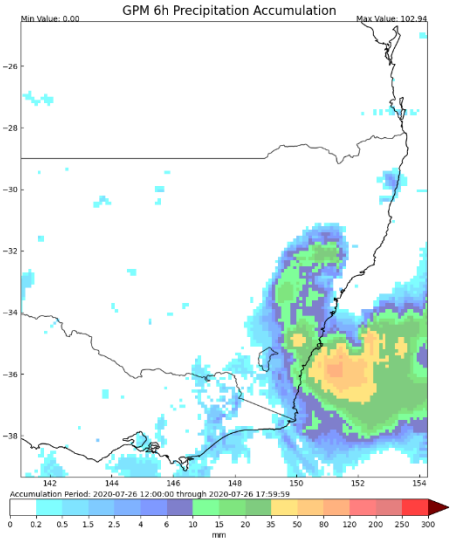
GPM 6h Precipitation Accumulation
Min Value: 0.00
Max Value: 102.94
Accumulation Period: 2020-07-26 12:00:00 through 2020-07-26 17:59:59
mm

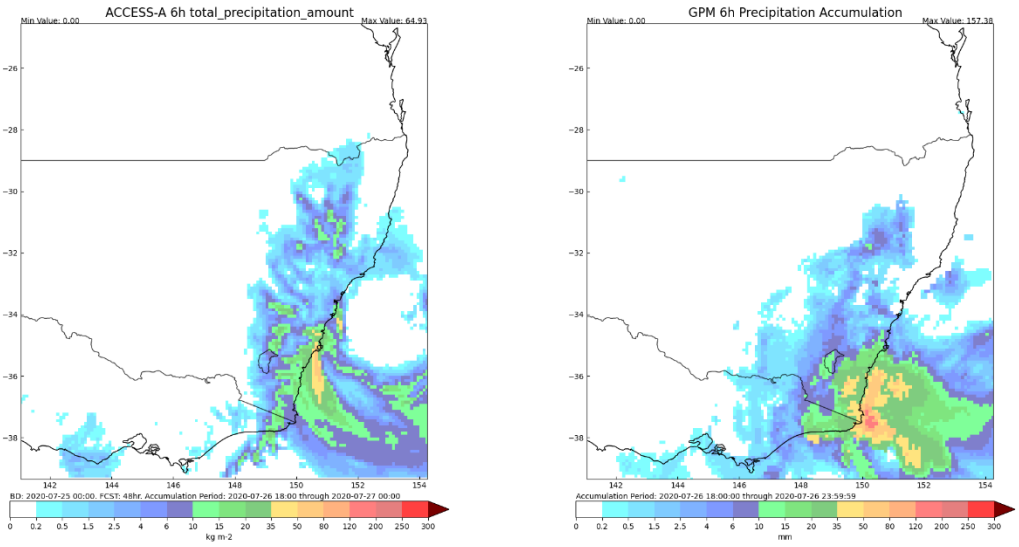


Figure 22: Four 6-hour precipitation accumulations forecast from ACCESS-A are presented in the left-hand column. These are from the 2020-07-25 00Z basetime and valid at 2020-07-26 06Z (30-hour forecast, top left), 2020-07-26 12Z (36-hour forecast, second from top left), 2020-07-26 18Z (42-hour forecast, second from bottom left) and 2020-07-27 00Z (48-hour forecast, bottom left). The corresponding 6-hour GPM rainfall accumulations are plotted in the right-hand column.

Figure 23 shows the mean error of the 10m wind speed for the event using land-based observations. The mean error is generally within 0.3 m/s of the observations indicating a very good simulation of winds for this East Coast Low.

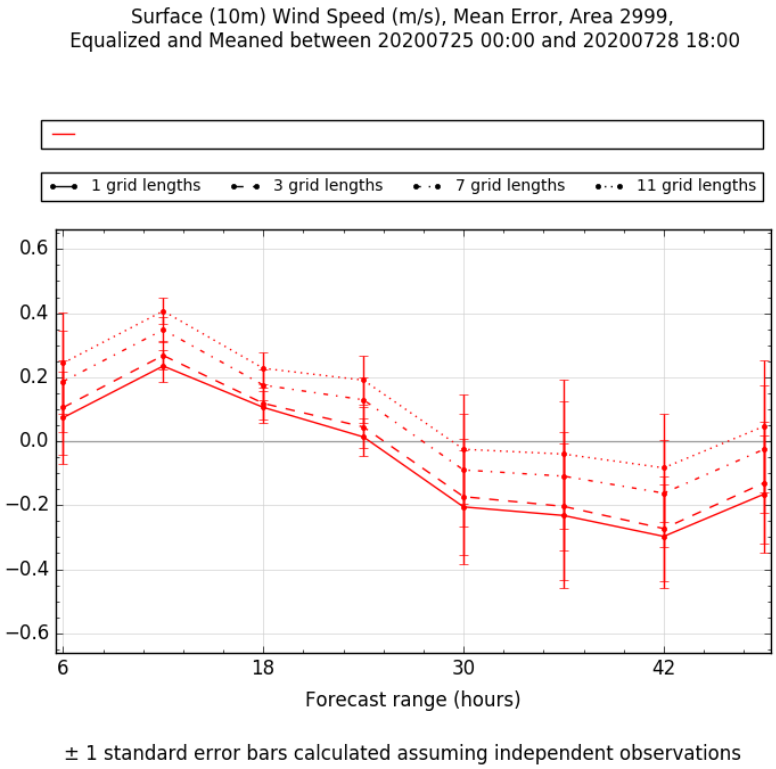


Figure 23: The 10m wind speed mean error as a function of lead time throughout the event for neighbourhoods of different size. At the native grid (solid line), 3 grid lengths (dashed line), 7 grid lengths (dot-dashed line) and 11 grid lengths (dotted line).

## 3.6 Perth fog

Fog formed along the south-western coast of WA during the night of 15 September and into the morning of 16 September 2017. It was a prolonged and widespread fog event, extending along the coast from the north of Geraldton to well south of Mandurah. Perth Airport reported fog from about 2130 UTC on 15 September (0530 am on 16 September AWST) and cleared around 0100 UTC 16 September (0900 am AWST).

This fog case study was used to examine the use of climatological aerosols in the visibility calculation instead of the constant value for aerosol concentrations used in previous ACCESS-City configurations. Using climatological aerosols should give more realistic visibility forecasts, with the largest impacts in areas of high aerosol concentrations such as South-East Asia. In Australia, the climatological aerosol concentration is low, which leads to higher visibilities in general. Figure 24 shows the values of the aerosol concentrations over south-west Western Australia.

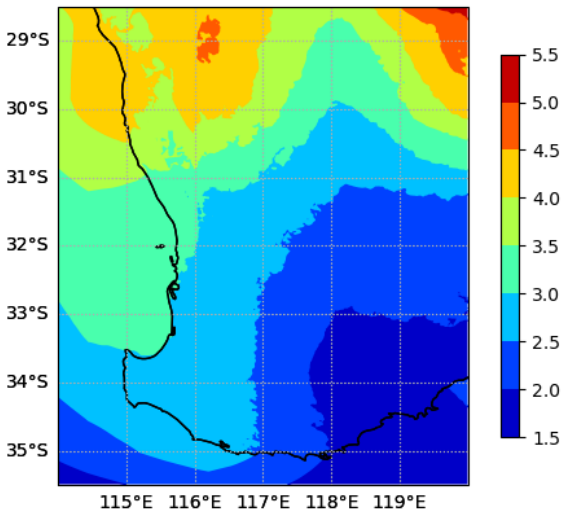


Figure 24: Climatological aerosol values over South-West Western Australia used in the visibility calculations.

The Himawari-8 night microphysics image (Figure 25a) shows the extent of the fog at 2200 UTC on 15 September 2017 (0600 am on 16 September AWST), which was one of the foggiest hours during this event. The fog is indicated by the cayenne colour, while the purple/red colour indicates overlying cloud. Figure 25b shows the minimum dewpoint depression throughout the period from the ACCESS-A simulation. This gives an indication of the moisture available at screen level, with the red colours showing areas where the air is near saturation. The minimum visibility (Figure 25c) has a nearly binary appearance, with visibilities less than 1 km where the air is almost completely saturated, and much clearer visibilities elsewhere. This behaviour can be attributed to the nature of the visibility scheme, which operates on a monodispersed aerosol field and is overly sensitive to input noise like small temperature perturbations. However, the maximum fog fraction for the event (Figure 25d) portrays a much more realistic image with reasonable values when considering both the available surface moisture in the model and the observed spatial pattern of fog from the satellite imagery.

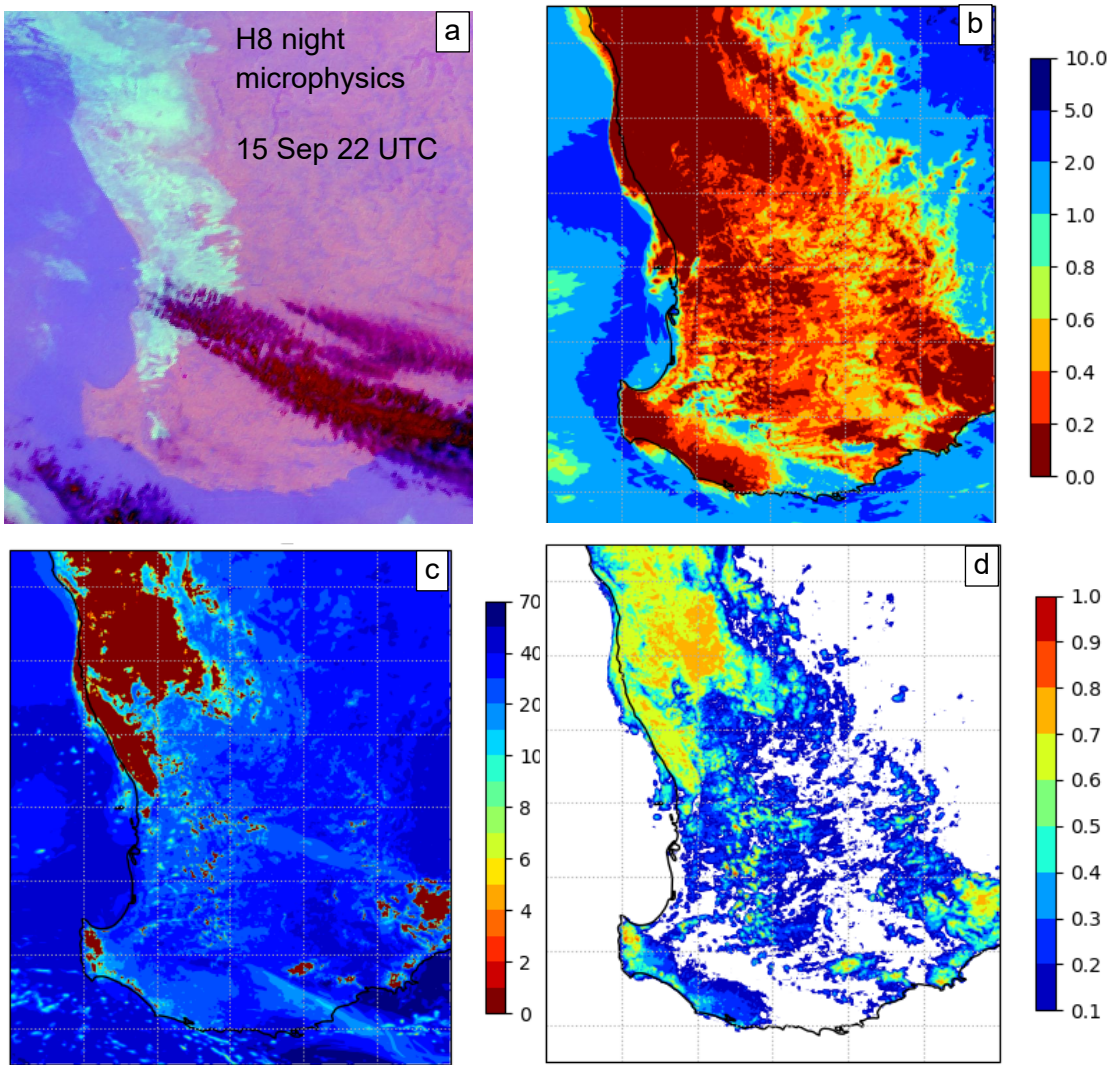


Figure 25: H8 night microphysics at 2200 UTC, 15 September (a), with ACCESS-A minimum dewpoint depression (b), minimum visibility (c), and maximum fog fraction (d) throughout the case.

## 3.7 Extreme heat

Australians were exposed to extreme heat over the “Black Summer” of 2019-2020. On 4 January 2020 temperatures in Penrith in Western Sydney reached 48.9 °C, a record high for any metropolitan area in Australia. On the same day the maximum temperature at Canberra Airport was 44.0 °C, 1.2 °C above the previous record for any site in the Australian Capital Territory (Bureau of Meteorology, 2020a).

To evaluate ACCESS-A’s ability to represent extreme heat events, we ran a 48-hour case study starting from 2020-01-02 1800Z. A whole-of-continent evaluation (Figure 26) shows 1.5 m air temperatures have mean errors of between -1 to +1.5 K. Largest positive errors occur at 6- and 30-hour lead times (10 am AEST), and negative errors at 18- and 42-hour lead times (10 pm AEST), indicating a warm bias at mid-morning and cool bias at other times, which is explored further in Section 4.

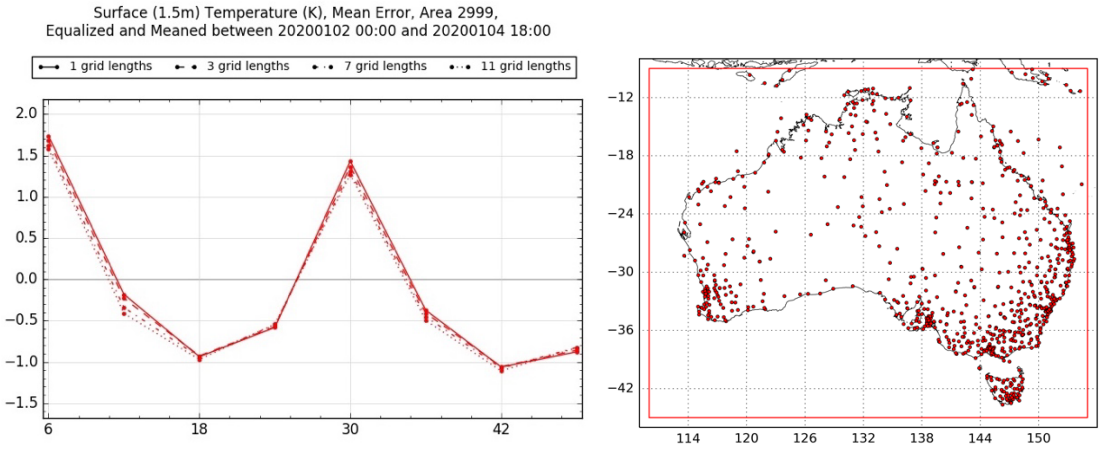


Figure 26: 1.5m temperature mean error (left) for the verification area shown in the right panel, where red dots indicate observations used.

Table 4 lists the top twenty daily maximum 1.5 m air temperature (Tmax) for Bureau sites in the ACORN-SAT national network over the simulation period, alongside the ACCESS-A and ACCESS-G3 (APS3 ACCESS Global model) air temperature for the nearest grid point. ACCESS-A Tmax is generally biased low, with a mean error of -0.4 °C. However, ACCESS-A shows improvement over the mean bias of ACCESS-G3 (-2.1 °C), noting that the global model has 12km horizontal grid boxes compared to ACCESS-A's 1.5km. The largest improvement from ACCESS-G (Williamtown, from -7.6 to -1.2 °C) is coastal, where the lower resolution global model defines the grid as ocean rather than land. Other sites showing large improvement are in areas of relatively complex orography (e.g., Canberra, Scone), with the higher resolution of topography in ACCESS-A providing benefit. Other sites that are not coastal nor have complex orography, can show improvement (e.g., West Wyalong, Bourke, Thargomindah, Rutherglen, Dubbo), or degradation (Tarcoola, Kyancutta). Some of the largest ACCESS-A biases are at sites on the fringes of large urban areas (e.g., Richmond on the outskirts of Sydney), which are known to be affected by errors in soil moisture initial conditions, an issue inherited in the ACCESS-A simulations from the global model.

Table 4: Bureau observing stations in the national ACORN-SAT network that recorded the highest daily 1.5m temperature (Tmax) during 3 - 4 January 2020, along with the ACCESS-A and ACCESS-G3 Tmax for the nearest grid point.

| | Station ID | Station Name | State | Obs. Tmax [° C] | ACCESS-A [° C] | ACCESS-G [° C] | ACCESS-A bias | ACCESS-G bias |
|---|---|---|---|---|---|---|---|---|
| 1 | 67105 | Richmond | NSW | 47.4 | 45.0 | 43.9 | -2.4 | -3.5 |
| 2 | 38026 | Birdsville | QLD | 46.8 | 45.4 | 45.7 | -1.4 | -1.1 |
| 3 | 17043 | Oodnadatta | SA | 46.5 | 47.1 | 45.7 | 0.6 | -0.8 |
| 4 | 48245 | Bourke | NSW | 46.3 | 46.2 | 45.0 | -0.1 | -1.3 |
| 5 | 46012 | Wilcannia | NSW | 46.2 | 46.0 | 45.4 | -0.2 | -0.8 |
| 6 | 50017 | West Wyalong | NSW | 46.1 | 45.8 | 43.7 | -0.3 | -2.4 |
| 7 | 72150 | Wagga Wagga | NSW | 46.1 | 46.8 | 44.2 | 0.7 | -1.9 |
| 8 | 48027 | Cobar | NSW | 45.9 | 44.9 | 44.5 | -1.0 | -1.4 |
| 9 | 17126 | Marree | SA | 45.7 | 44.7 | 44.2 | -1.0 | -1.5 |
| 10 | 46126 | Tibooburra | NSW | 45.7 | 45.6 | 45.5 | -0.1 | -0.2 |
| 11 | 82039 | Rutherglen | VIC | 45.6 | 45.4 | 42.7 | -0.2 | -2.9 |
| 12 | 45025 | Thargomindah | QLD | 45.6 | 45.9 | 43.9 | 0.3 | -1.7 |
| 13 | 16098 | Tarcoola | SA | 45.6 | 47.9 | 45.6 | 2.3 | 0.0 |
| 14 | 18044 | Kyancutta | SA | 45.6 | 47.4 | 46.1 | 1.8 | 0.5 |
| 15 | 16001 | Woomera | SA | 45.5 | 45.1 | 44.7 | -0.4 | -0.8 |
| 16 | 61078 | Williamtown | NSW | 45.5 | 44.3 | 37.9 | -1.2 | -7.6 |
| 17 | 61363 | Scone | NSW | 44.6 | 42.3 | 39.0 | -2.3 | -5.6 |
| 18 | 52088 | Walgett | NSW | 44.4 | 44.7 | 43.8 | 0.3 | -0.6 |
| 19 | 65070 | Dubbo | NSW | 44.3 | 44.1 | 42.8 | -0.2 | -1.5 |
| 20 | 70351 | Canberra | ACT | 44.0 | 41.1 | 37.4 | -2.9 | -6.6 |
| | | | **mean:** | **45.7** | **45.3** | **43.6** | **-0.4** | **-2.1** |

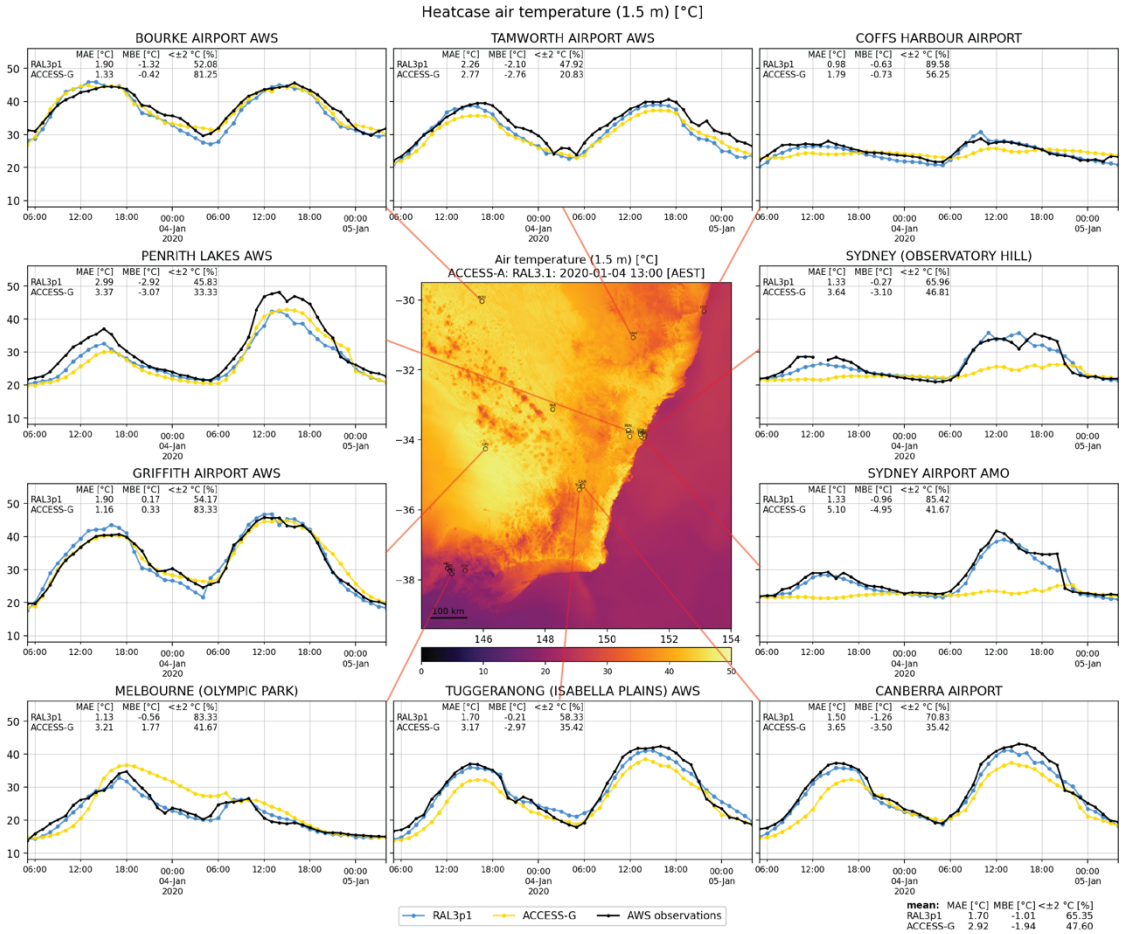


Figure 27: 1.5m temperature at select AWS stations on 04/01/2020 and for ACCESS-A (RAL3p1) and ACCESS-G3. The centre panel shows a map of ACCESS-A 1.5m temperature at 13:00 AEST along with AWS stations in the circles. Site metrics are indicated top right of each panel, and mean statistics in the figure bottom right (MAE: mean absolute error; MBE: mean bias error; <± 2°C: percent within 2 °C of observations).

To understand the temporal performance of ACCESS-A screen level temperature, we use Bureau automatic weather station (AWS) 1-hour instantaneous observations for a selection of sites in eastern Australia (Figure 27). The ACCESS-A model better captures the diurnal cycle and peak air temperatures compared with the operational global model ACCESS-G3, particularly for coastal sites where the higher resolution reduces the fractional coverage of ocean impacting the grid-box mean temperature (e.g. Sydney Observatory Hill, Sydney Airport). Elsewhere, ACCESS-A has a better representation of surface heating and cooling rates in cities compared with ACCESS-G (e.g. Melbourne Olympic Park).

## 3.8 Extreme winter weather

The extreme winter weather of 9-10 June 2021 over south-east Australia was used to look at the model's performance in simulating cold temperatures, snow, high winds and heavy rainfall. Figure 28 shows the MSLP analysis and minimum temperatures over Australia for 10 June 2021.

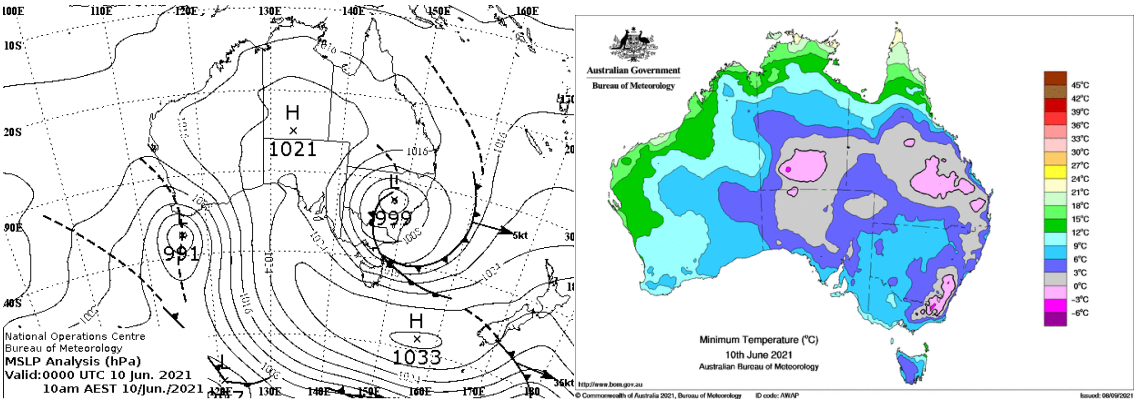


Figure 28: The Bureau's MSLP analysis at 0000 UTC (left) and minimum temperatures (right) for 10 June 2021.

RES verification was done over south-eastern Australia (Figure 29). The timing and precipitation amounts were generally well represented and there was no evidence of the cold bias or excessive snow noted in other RAL3 assessments by the Met Office. The mean 10m winds were biased slightly low in the first 30 hours and slightly high in the last 18 hours but the errors were generally within 0.5 m/s (Figure 30).

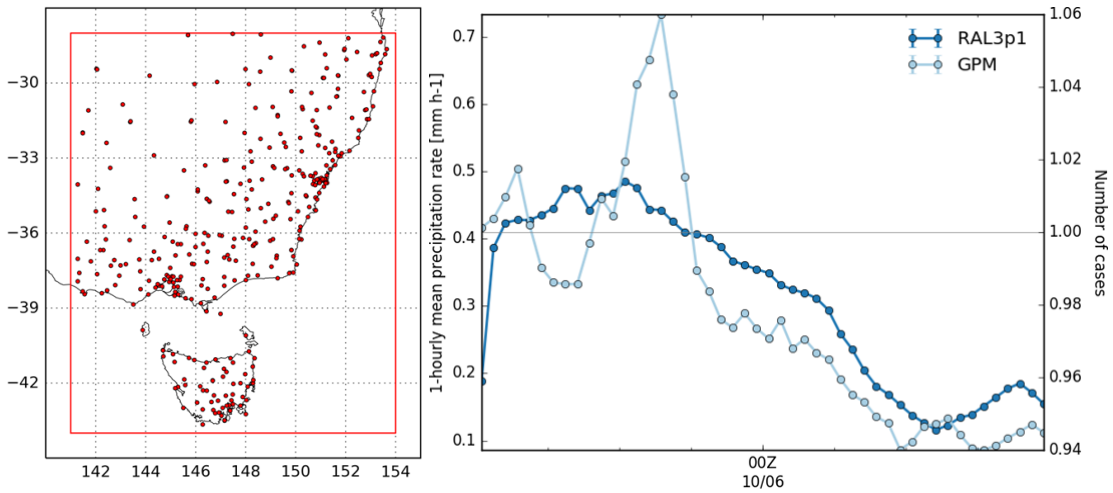


Figure 29: RES verification area and AWS stations (left) and hourly mean precipitation rate over the area (right) of ACCESS-A (dark blue) and GPM satellite (light blue).

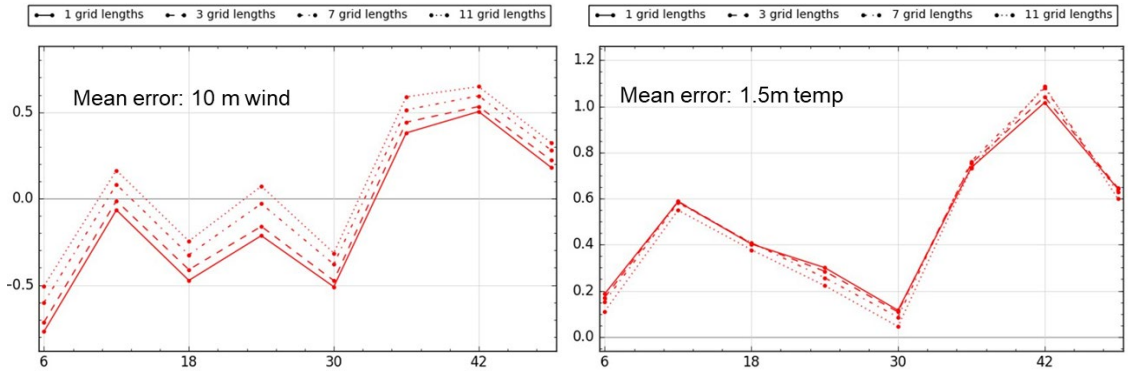


Figure 30: Time series of the mean error in 10 m wind (left) and screen temperature (right) for different model grid lenghts over the RES verification region.

Taking a closer look at the mountainous region in eastern Victoria and south-western NSW, the amount and location of heavy precipitation was captured very well (Figure 31).

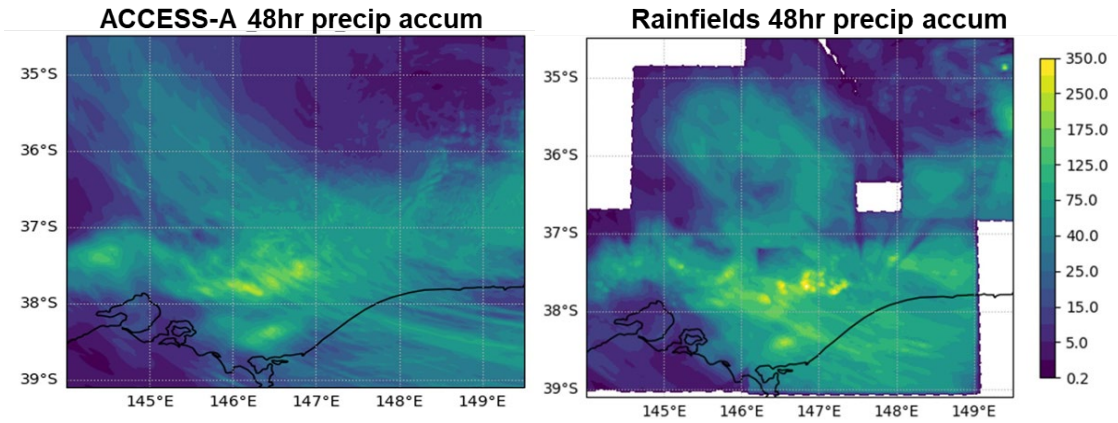


Figure 31: ACCESS-A (left) and Rainfields (right) 48-hour precipitation accumulation for 10-11 June 2021 over eastern Victoria and south-western NSW.

Looking at Tasmania (Figure 32), the wind speed and direction was generally captured very well, although there are locations in areas of steep topography where the wind speeds were too low.

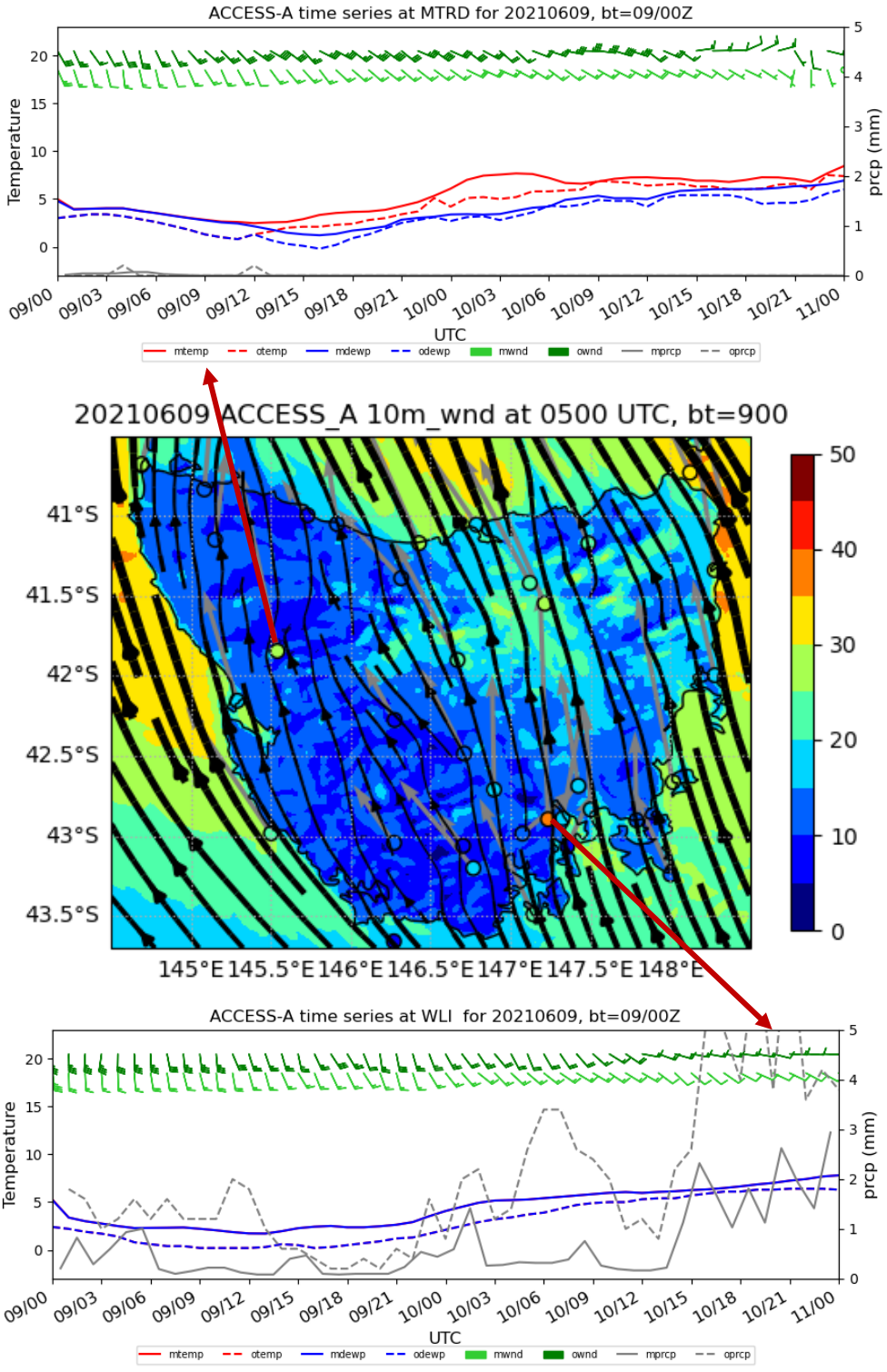


Figure 32: ACCESS-A and AWS 10 m wind over Tasmania for 0500 UTC 9 June 2021 (middle) with time series of 10 m wind, screen temperature, dewpoint temperature, and precipitation at two AWS locations with steep topography where ACCESS-A wind speeds were noticeably low. During periods of precipitation the red temperature lines are obscured by the dewpoint temperatures for both the model and observations as they were equal.

## 3.9 Brisbane hailstorm

In October 2020, Queensland experienced 11 consecutive days of widespread thunderstorms, culminating in the most significant and destructive thunderstorm outbreak on 31 October 2020. These thunderstorms of 31 October predominantly impacted south-eastern Queensland. During the outbreak, many right and left-moving storms were observed, along with single cell bow echoes. However, it was two classic supercells that delivered the most severe impacts (Bureau of Meteorology, 2020c).

These supercells initiated within 35 minutes of each other along a dryline across the eastern Darling Downs. They traversed east southeasterly along tracks separated by less than 10 km. Grapefruit sized hail stones (maximum diameter of 13.8 cm) were reported, some of the largest hailstones ever reported in Australia. Supercell 1 was first observed at 12.12 pm local time (0212 UTC) before dissipating at 2.48 pm local time (0448 UTC). Supercell 2 was observed from 12.48 pm (0248 UTC) to 2.36 pm (0436 UTC) (Bureau of Meteorology, 2020c).

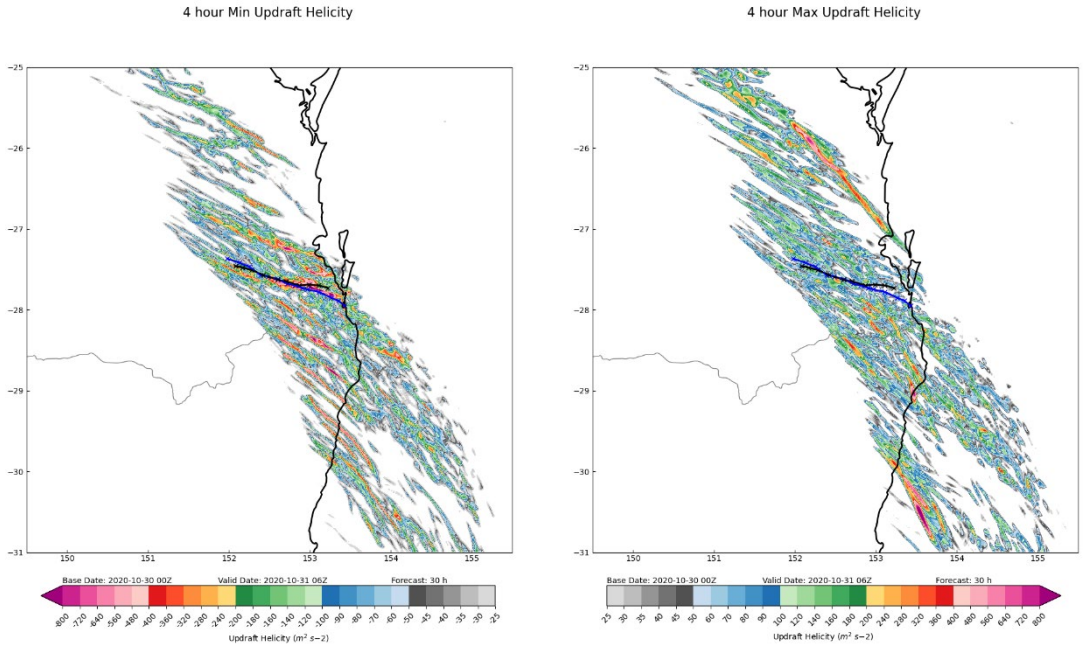

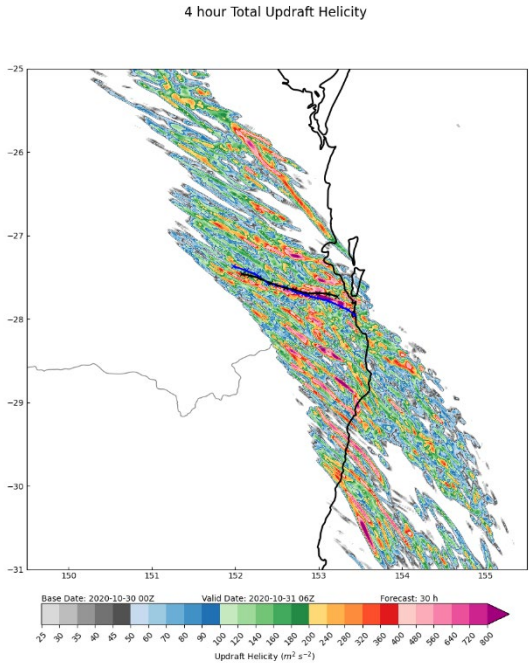


Figure 33: Four-hour minimum updraft helicity tracks (top left), four-hour maximum updraft helicity tracks (top right) and four-hour total updraft helicity tracks valid at 2020-10-31 06Z. The observed tracks of supercell 1 (blue line and crosses) and supercell 2 (black line and crosses) are indicated in each panel.

Updraft Helicity (UH) is a diagnostic field used to identify rotating storms. It is calculated as the integral of the product of the vertical velocity and vertical component of vorticity over the model vertical levels from 2 – 5 km (Kain et al., 2008; Sobash et al., 2011) at each timestep. In the southern hemisphere, the maximum UH field is used to identify anti-cyclonic (right-moving) storms while the minimum UH field is used to identify cyclonic (left-moving) storms (Marin et al., 2021).

Figure 33 presents the 4-hour minimum, maximum and total updraft helicity tracks. These 4 hours span from 02Z to 06Z on 2020-10-31 (the two supercells were observed during this time period). These panels also indicate the observed paths of supercell 1 (blue line and crosses) and supercell 2 (black line and crosses). The 30-hour forecast from ACCESS-A successfully identified the spatial region in which the two supercells were observed, with the correct timing. Note that there were many storms during this event, however only the two most destructive supercell paths have been plotted in Figure 33.

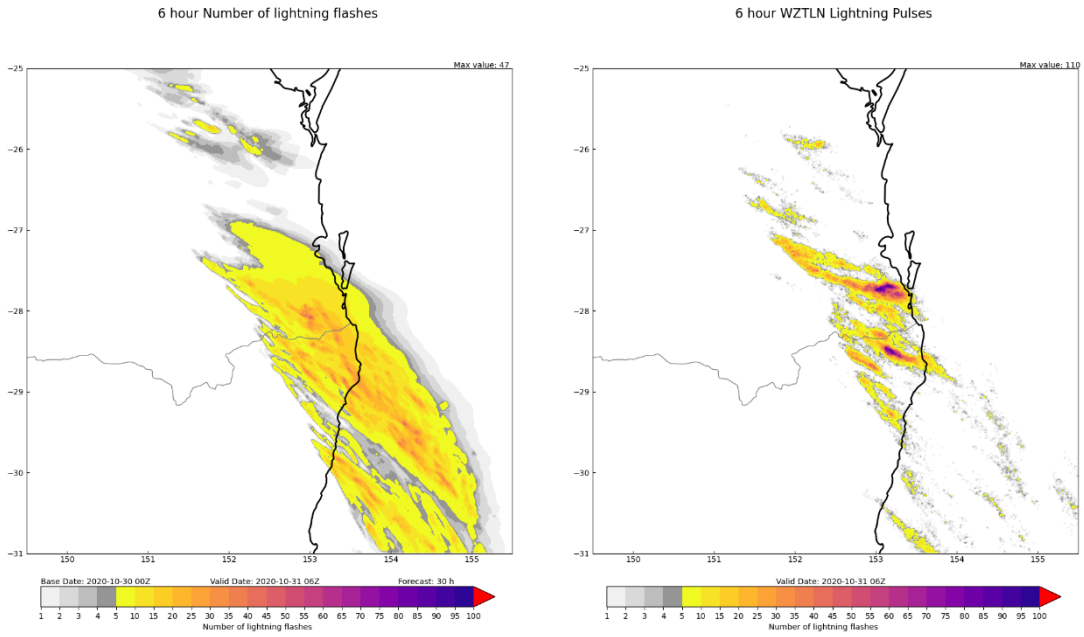


Figure 34: 6-hourly number of lightning flashes from ACCESS-A forecast (left) valid at 2020-10-31 06Z, a 30-hour forecast. The corresponding 6-hour WZTLN total lightning pulse observations (right).

Figure 34 shows the 30-hour forecast of 6-hourly number of lightning flashes valid at 2020-10-31 06Z. This includes the period in the UH plots in Figure 33 when the supercells were observed. The right panel shows the lightning pulse observations from the Weatherzone Total Lightning Network data, which measures both intra-cloud and cloud to ground lightning pulses. As there may be multiple pulses measured for the same lightning flash, these observations cannot be used for a quantitative assessment of the modelled lightning flashes. In general, ACCESS-A is doing a reasonable job in forecasting when and where lightning is likely to occur for these storms. The forecast lightning field is smoother and larger than observed, with the number of lightning flashes lower than the observed lightning pulses. While it is difficult to compare the modelled lightning to these observations, this result may suggest that ACCESS-A under forecasts the number of lightning flashes.

# 4. Verification

While case studies are extremely useful for detailed evaluation of specific model processes, the performance and verification of the model can vary between single case studies. To get an overview of the general model tendencies, the Regional Evaluation Suite (RES) has been used to evaluate the model over several cases and trial periods, spanning different seasons, start times and different weather phenomena in 2020 and 2021. Overall, 148 model cycles have been used in the verification, which has been stratified into five sub-regions (see Figure 35) to differentiate between different climatic

zones. The zones are: Tropics, Subtropics, Southeast Australia (SEAUS), Central and (Southern Australia) Mediterranean.

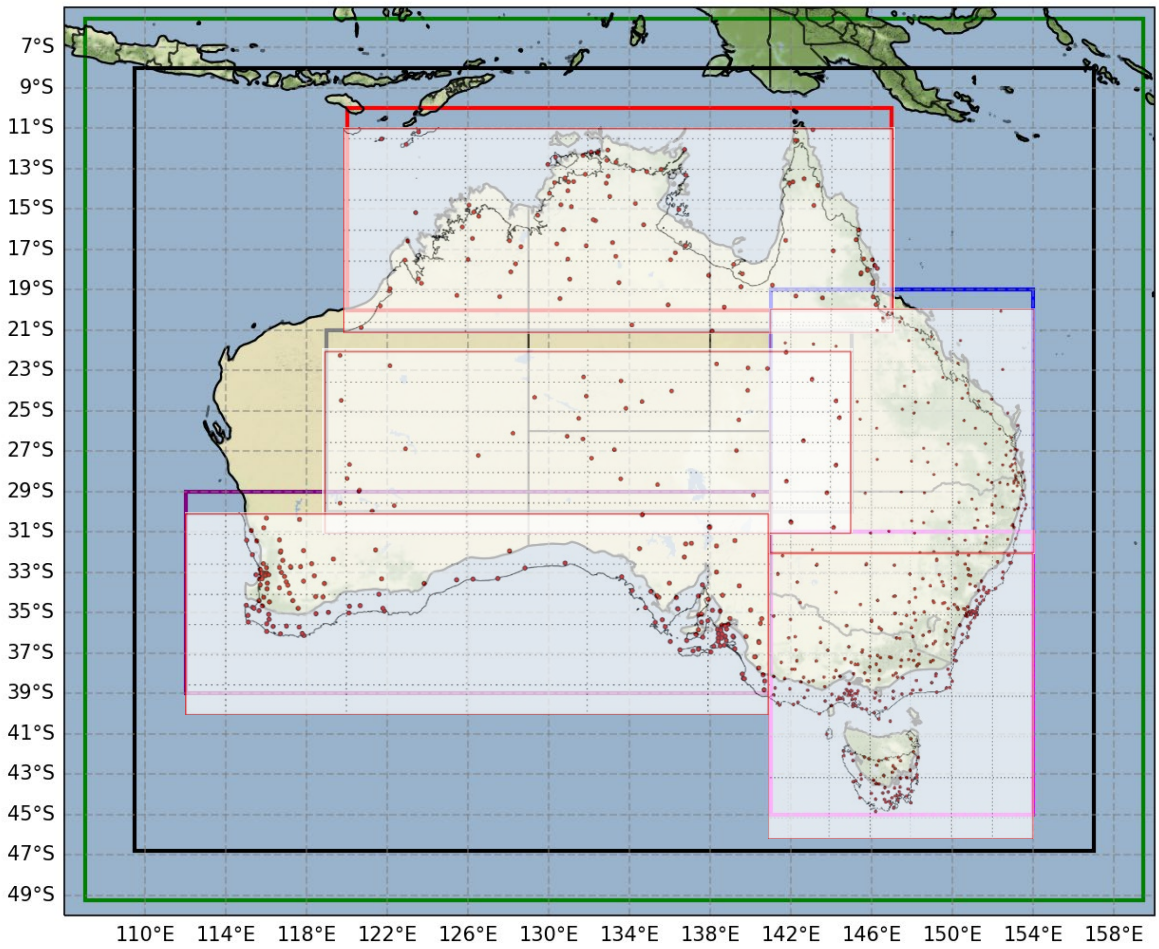


Figure 35: Domains and locations of AWS used for the Regional Evaluation Suite (RES) verification. The domains from top to bottom and left to right are: Tropics, Central, (Southern Australia) Mediterranean, Subtropics, Southeast Australia (SEAUS).

Table 5 summarises the verification results for each region for precipitation, screen level temperature and relative humidity, 10 m wind speed, and cloud cover. The breakdown of verification results for each domain is given in Sections 4.1 – 4.5.

Table 5: Summary of the verification results for each region.

| | **Precipitation** | **Screen temperature and humidity** | **10m winds** | **Clouds** |
|---|---|---|---|---|
| **Tropics** | Under forecast low rain rates (< 4mm/hr) and over forecast medium rates (8-32mm/hr), | Cold bias, apart from morning temperatures (0000 UTC), which are neutral. RH too | Biased high during the night (to 0.6m/s), | Total cloud cover overestimated (<10%) apart from mid-morning |

| | | | | |
|---|---|---|---|---|
| | with high rain rates underestimated. 6-hour accumulations compare well to gauges. | high, except for the morning hours, when it is slightly low. | slightly too low during the day. | where small underestimation. |
| **Sub-tropics** | All rain rates below 64mm/hr slightly under forecast compared to GPM. | Temperatures are slightly cold to neutral, except for morning temperatures (0000 UTC) which have a warm bias biased (~0.6 deg). RH errors mirror temperature errors. | Wind speeds close to neutral, slightly too high (0.1 m/s) at 1800 UTC (~4am), decreasing to -0.6 m/s at 0600 UTC (4pm). Wind speed error increases with lead time. | Mean error in total cloud cover close to neutral. |
| **Southeast Australia (SEAUS)** | Low rain rates (> 2mm/hr) slightly over forecast. Higher rain rates (> 4mm/hr) under forecast with an increasing frequency as rates increase. | Morning temperature (0000 UTC) warm bias (~0.6 deg), other times close to neutral. RH– biased low during the morning, close to neutral during the night. | Wind speeds small low bias, worst at 0600 UCT when it reaches ~-0.6m/s. Mean bias decreases with increasing lead time. | Mean error in total cloud cover close to neutral. |
| **Central** | Slightly under forecast low rain rates and over forecast medium rates. Relative frequency of high rain rates well represented. | Night temperature cold bias (~-1.5 degrees), slight warm bias (~0.5 degrees) during the day. RH biased high during the night, unbiased during the day. | Wind speed biased slightly high (up to 0.6 m/s). Diurnal cycle evident, with 0600 UTC (afternoon) wind bias close to zero. | Very little cloud/rain in Central Aus to have reliable verification results but an indication of too little cloud cover. |
| **(Southern Australia) Mediterranean** | Low rain rates (up to 2mm/hr) match well with GPM. Frequency of higher rain rates under forecast. | Nighttime cold bias (0.5-1 degrees), daytime warm bias (0.5-1 degrees). RH bias opposite to temp bias. | 10m winds are too low (up to 0.5 m/s), except for morning (0000 UTC) when bias is 0. Maximum low bias is at 0600 UTC (early afternoon). | TCC under forecast. |

## 4.1 Tropical domain verification

Verification of rainfall is considered using two metrics, hourly rain rate distributions compared to the GPM satellite-derived rainfall and 6-hourly accumulations compared to rain gauges. Compared to GPM, Figure 36 shows that ACCESS-A under forecasts light rain rates (< 4 mm/hr) and over forecast medium rates (8-32mm/hr) in the tropics. Heavy rain rates are under forecast compared to GPM, and this underestimate is expected to be worse compared to radar-derived rain rates (see e.g. Figure 4 in Bush et al. 2025). 6 hourly rain accumulations have a small underestimate of 0.4 mm compared to the rain gauge observations (Figure 37), where the spin up from the global model initial conditions can be seen in the figure from 6 – 12 hours.

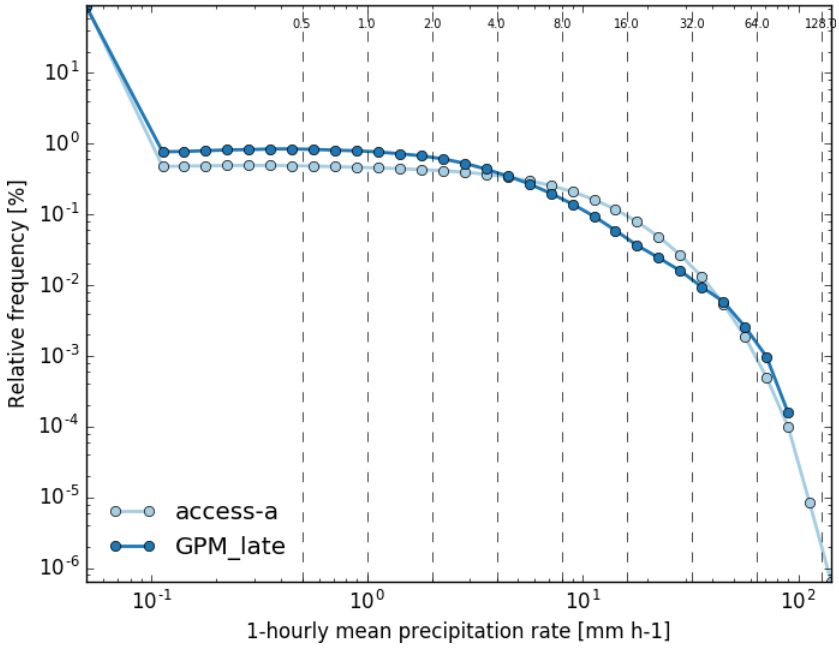


Figure 36: Histogram of the ACCESS-A and GPM hourly mean precipitation rate over the Tropics.

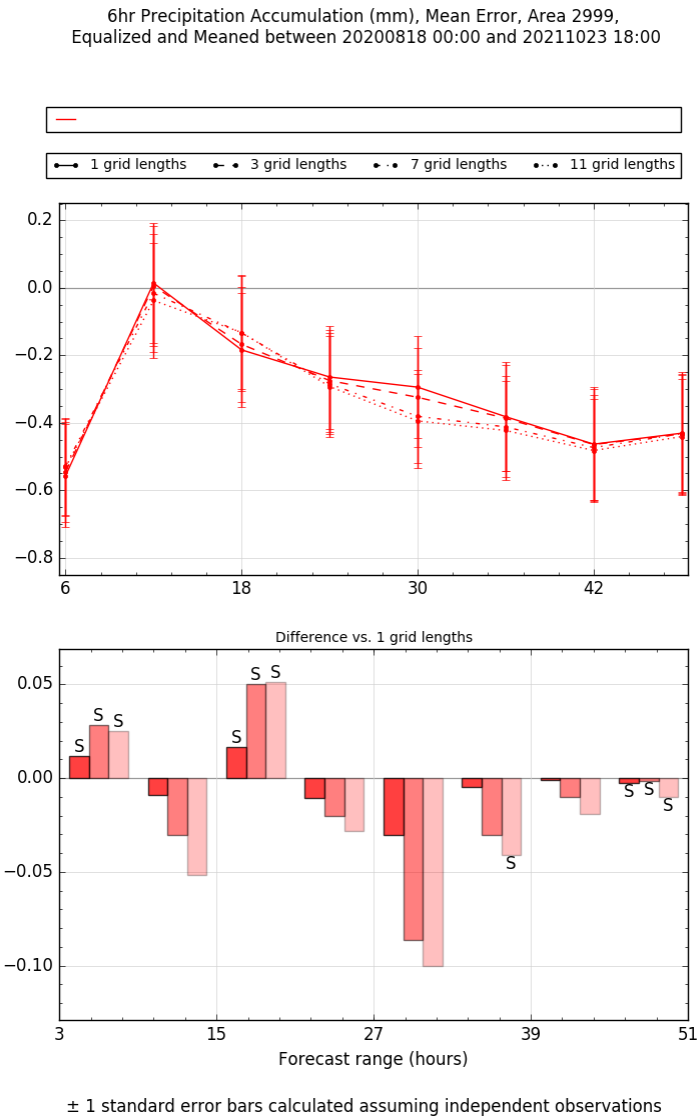


Figure 37: ACCESS-A precipitation mean error as a function of lead time against rain gauges over the Tropics.

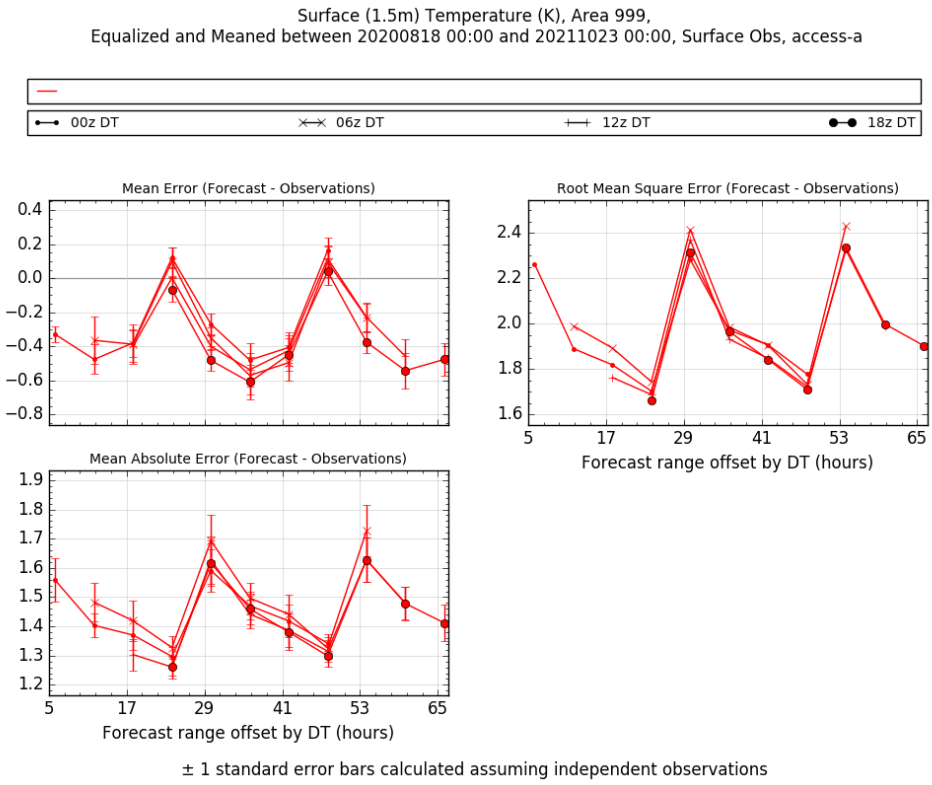


Figure 38: ACCESS-A diurnal range of screen temperature error for the Tropics.

Verification of the 1.5m temperature (Figure 38) and relative humidity (Figure 39) shows a general cold (<-0.6°C) and moist (<4%) bias, apart from the morning (0000 UTC (8-10am)), which shows very small biases of opposite sign. The errors have a strong diurnal signature with the largest errors occurring at 1700 UTC, which is around 2am local time. The timing of this maximum error is also seen in the 10m wind speeds (Figure 40), with overestimated wind speeds of up to 0.4 m/s overnight, and a small underestimate of < -0.2 m/s during the daytime.

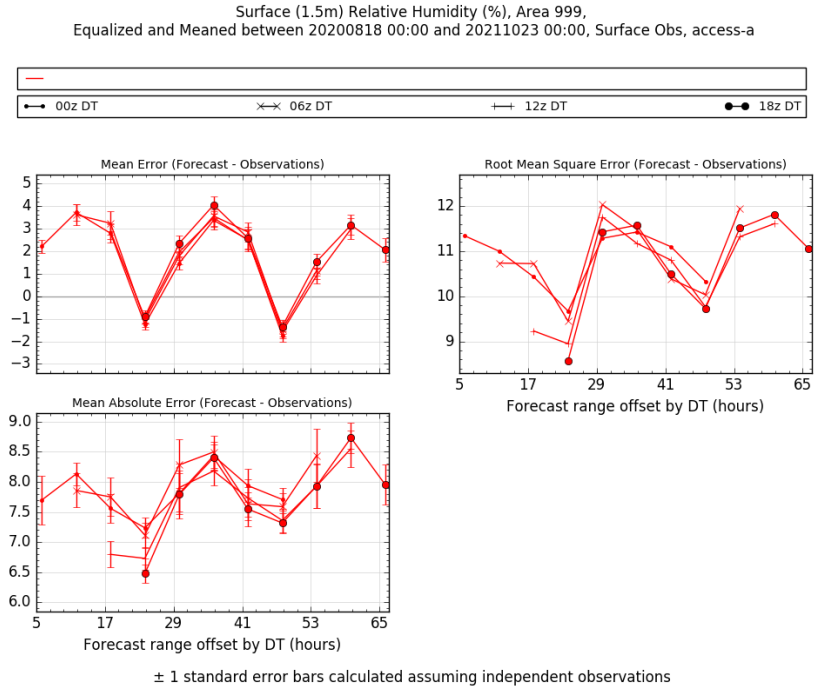


Figure 39: ACCESS-A diurnal range of screen level relative humidity error for the Tropics.

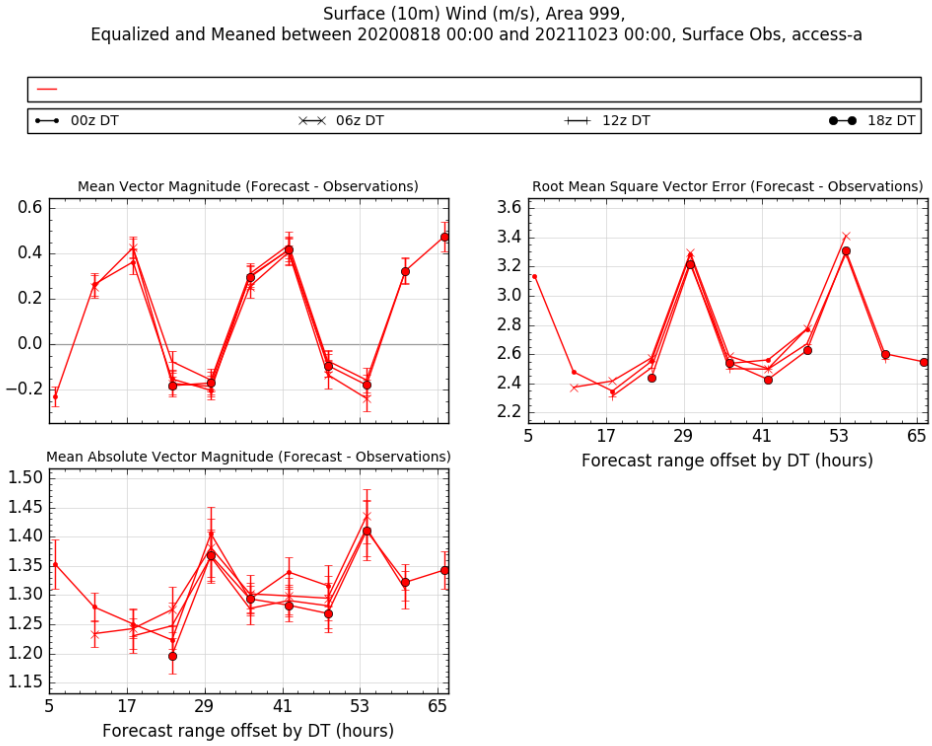


Figure 40: ACCESS-A diurnal range of 10m wind error for the Tropics.

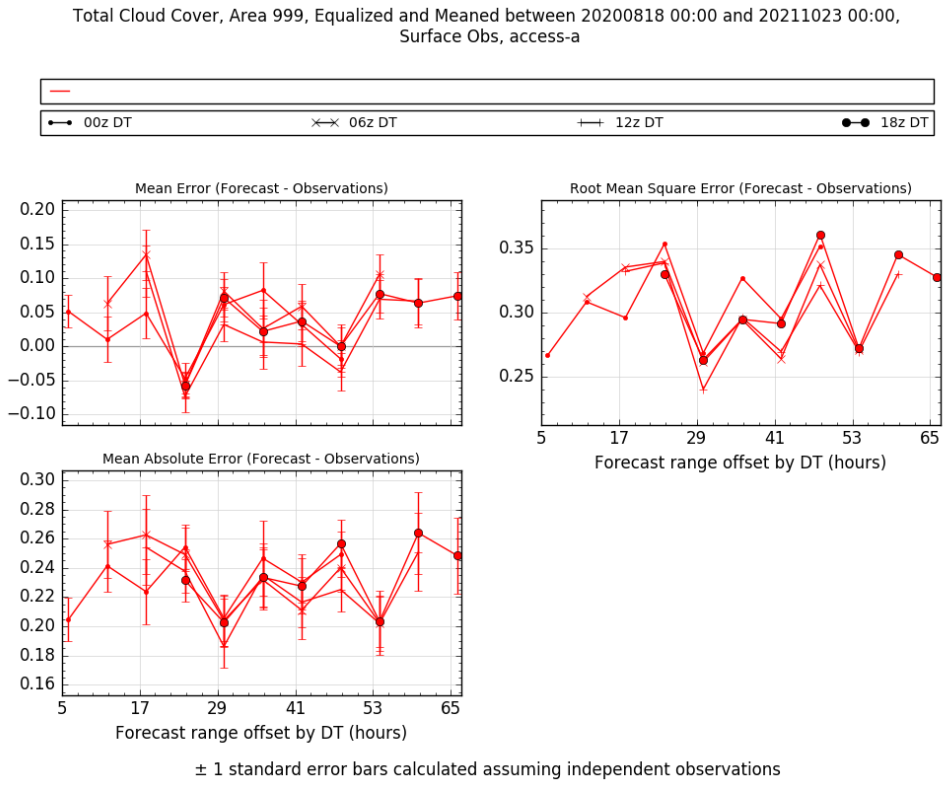


Figure 41: ACCESS-A diurnal range of cloud amount error for the Tropics.

Verification of total cloud cover in the Tropics (see Figure 41), shows that there is a small overestimate of total cloud fraction at all times apart from early morning local time (00 UTC). 8-10am local time has a small underestimate of cloud fraction, which corresponds to the time when the temperature bias shifts from cold to neutral indicating that the realistic temperatures at this time may be due to compensating effects due to lack of cloud cover. In general, the overestimated total cloud cover bias is <10%, with the RMSE around 30%.

## 4.2 Subtropical domain verification

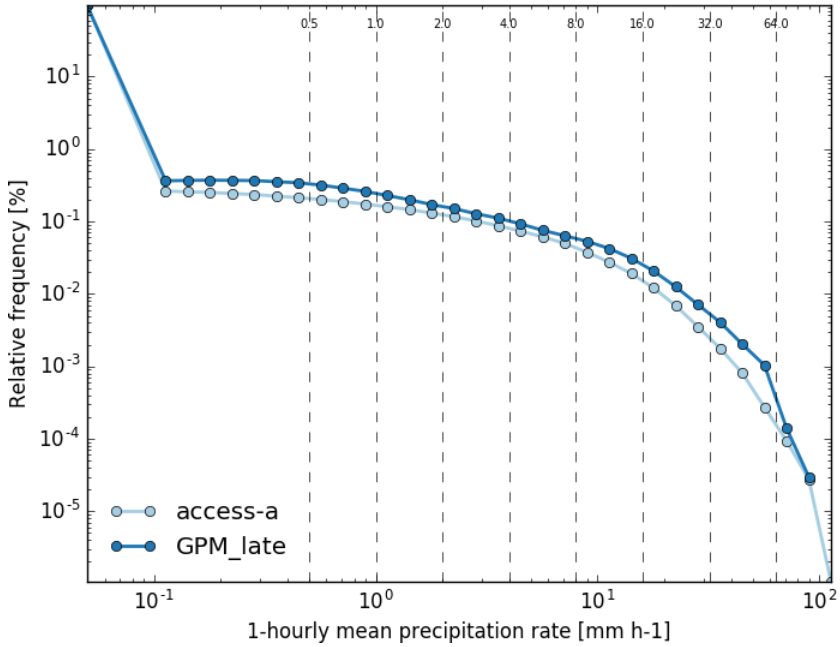


Figure 42: Histogram of the ACCESS-A and GPM hourly mean precipitation rate over the Subtropical region.

Compared to the GPM satellite-derived rainfall observations, Figure 42 shows that ACCESS-A under forecasts all rain rates, particularly those between 10 and 64 mm/hr. This is in contrast to the comparison with the 6 hourly rainfall accumulations measured by rain gauges (Figure 43), which shows that the modelled rainfall accumulations are represented very well with maximum overestimations < 0.4 mm/6 hours. The lack of an underestimation in the comparison of rain gauges compared to the satellite observations could be due to differences in the spatial or temporal sampling, or differences in the observations, highlighting the need to use multiple sources of rainfall observations to assess models.

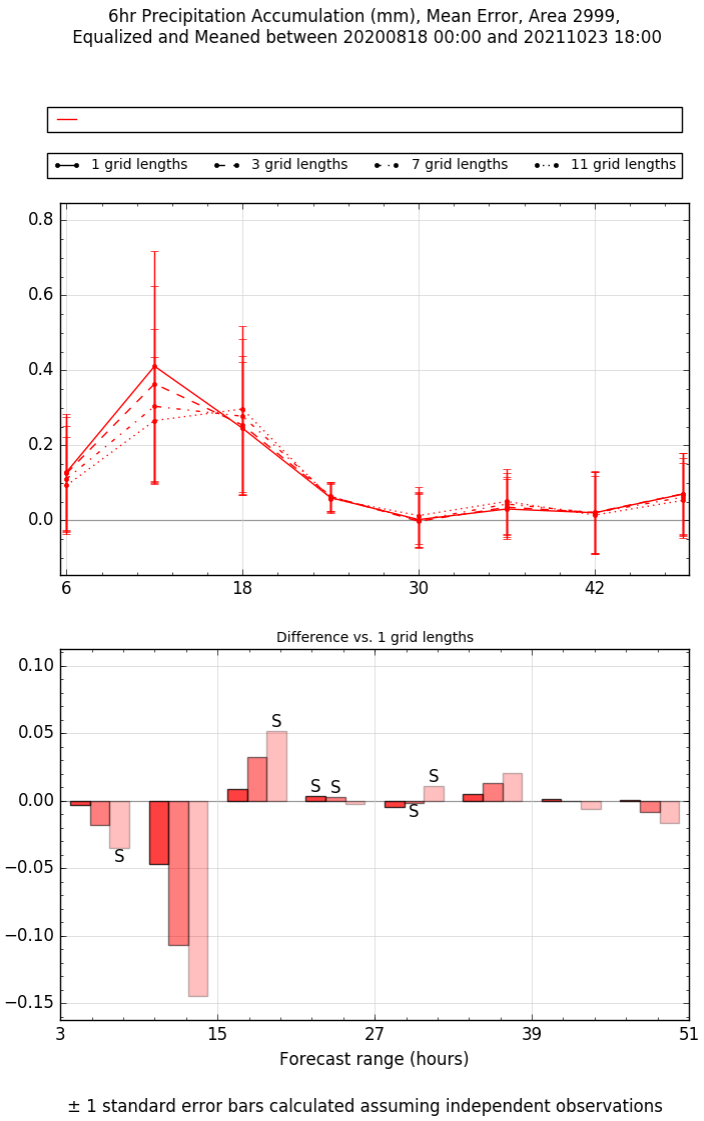


Figure 43: ACCESS-A precipitation mean error as a function of lead time against rain gauges over the Subtropics.

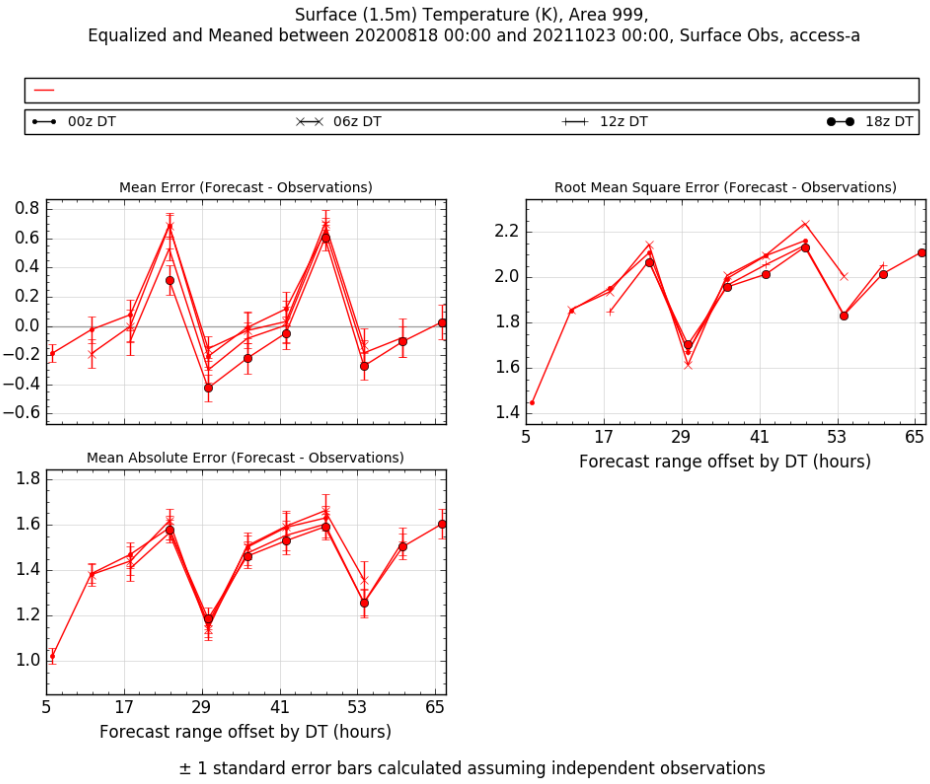


Figure 44: ACCESS-A diurnal range of screen level temperature error for the Subtropical region.

Subtropical 1.5m screen temperatures modelled by ACCESS-A have a cold – neutral bias apart from morning temperatures (0000UTC, 10am) that have a warm bias of up to 0.6 degrees (see Figure 44). The RMSE is smaller than for the tropical region with a larger increase in error with lead time. The errors in the screen level RH shown in Figure 45 mirror the errors seen in the screen level temperature, with a moist bias of up to 4% apart from the morning where the bias shifts to a dry bias of the same magnitude.

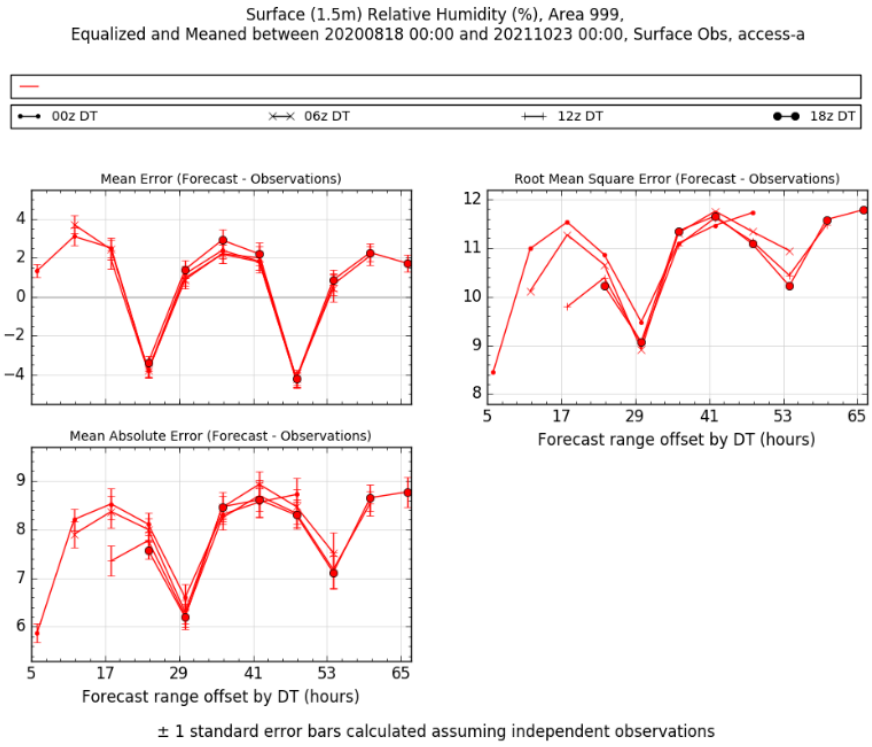


Figure 45: ACCESS-A diurnal range of screen level relative humidity error for the Subtropical region.

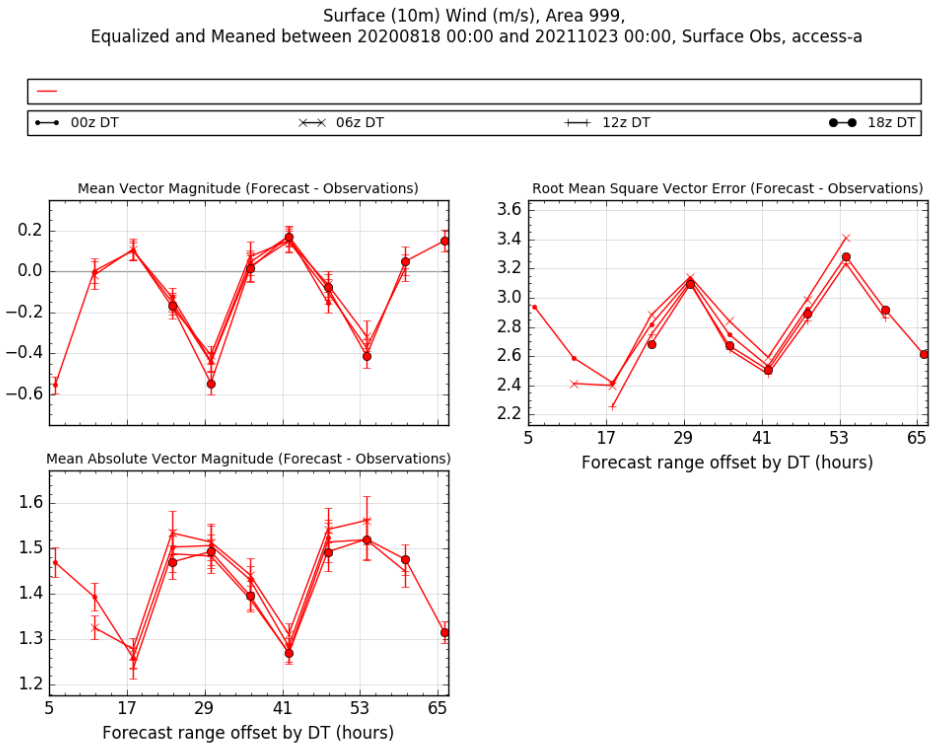


Figure 46: ACCESS-A diurnal range of 10m wind error for the Subtropical region

The subtropical domain's cold and moist bias corresponds to the times when the 10m wind speeds are too low and where the wind RMSE is largest (see Figure 46). Whereas the warm bias corresponds to times when the winds speeds are closer to those observed with a small overestimate in wind speed. The total cloud cover in the subtropics shown in Figure 47 is generally underestimated by about 10%, with the largest RMSE of 40% coinciding with the times prior to when the near surface temperatures are too warm.

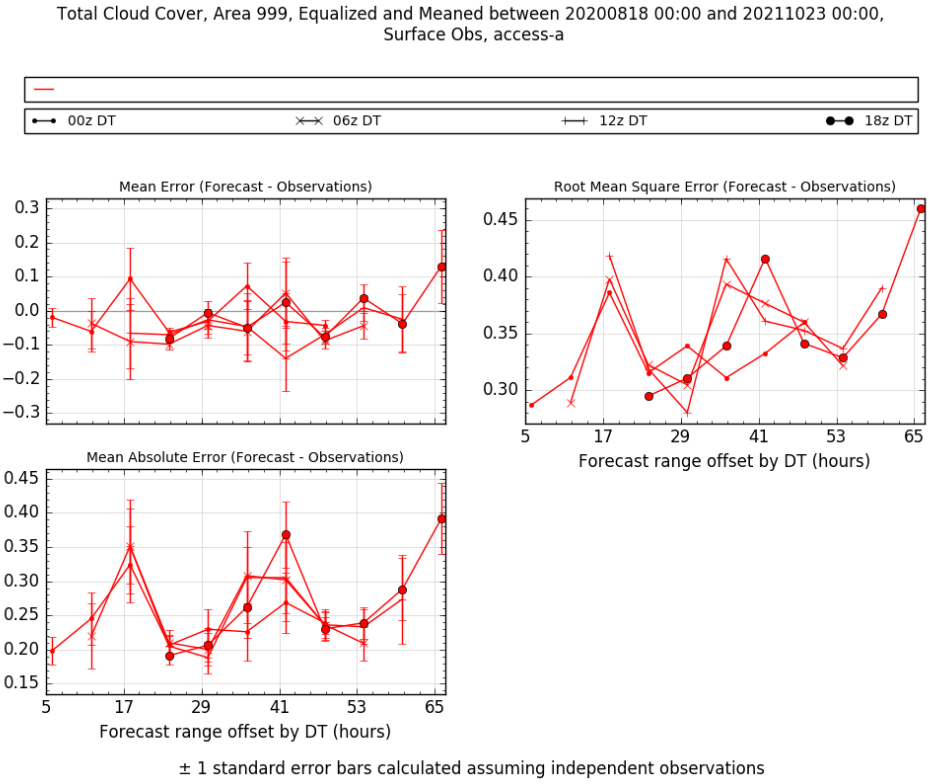


Figure 47: ACCESS-A diurnal range of cloud amount error for the Subtropics.

## 4.3 South East Australia domain verification

Assessing rainfall for the SE Australia domain shows that ACCESS-A tends to under forecast rain rates greater than 4 mm/hr while over forecasting light rain (Figure 48). The mean error against rain gauges for 6-hour rainfall accumulations shown in Figure 49 is an underestimate of about 0.2 mm, indicating no systematic bias in the rainfall accumulation.

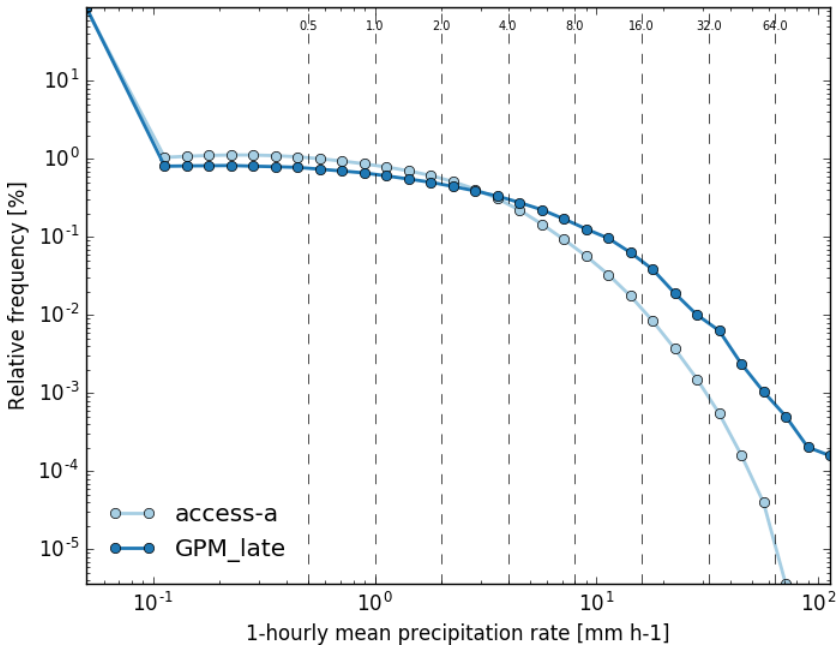


Figure 48: Histogram of the ACCESS-A and GPM hourly mean precipitation rate over the SEAUS region.

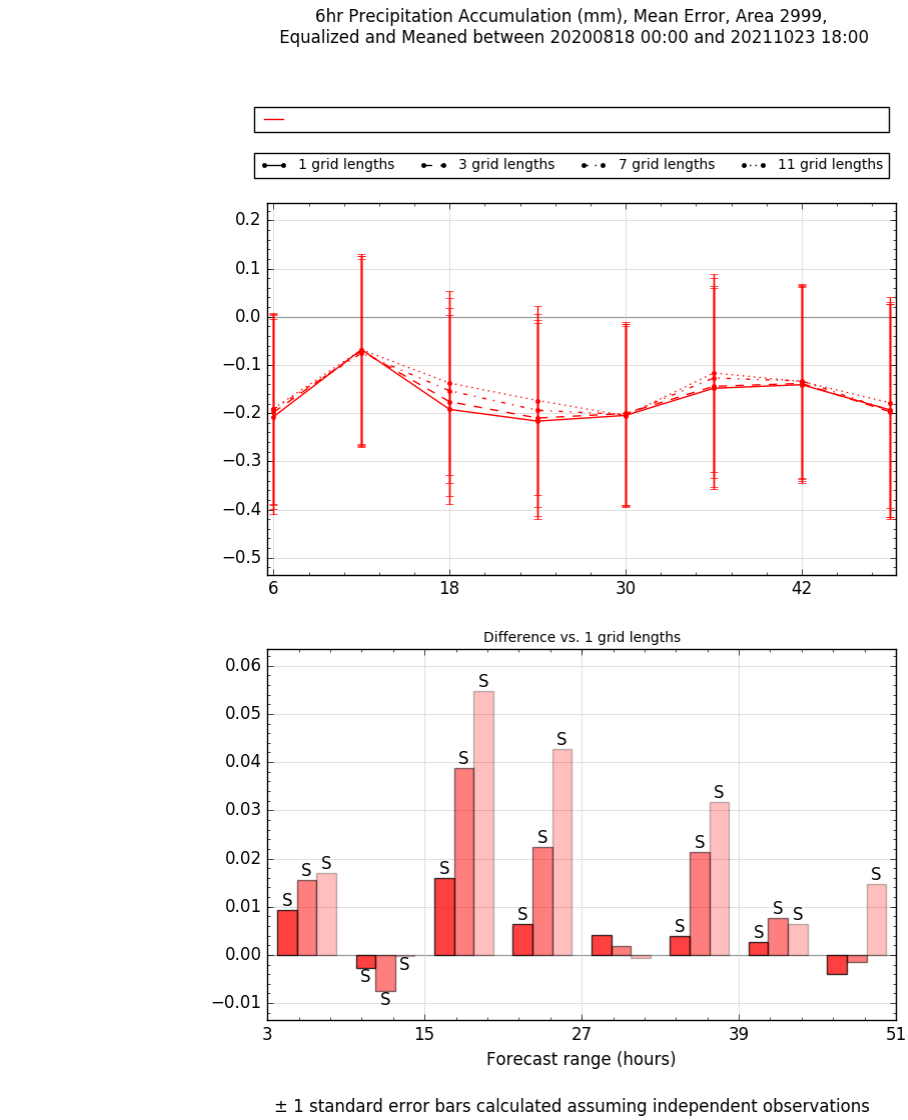


Figure 49: Timeseries of ACCESS-A precipitation mean error against rain gauges over the Southeast Australian region.

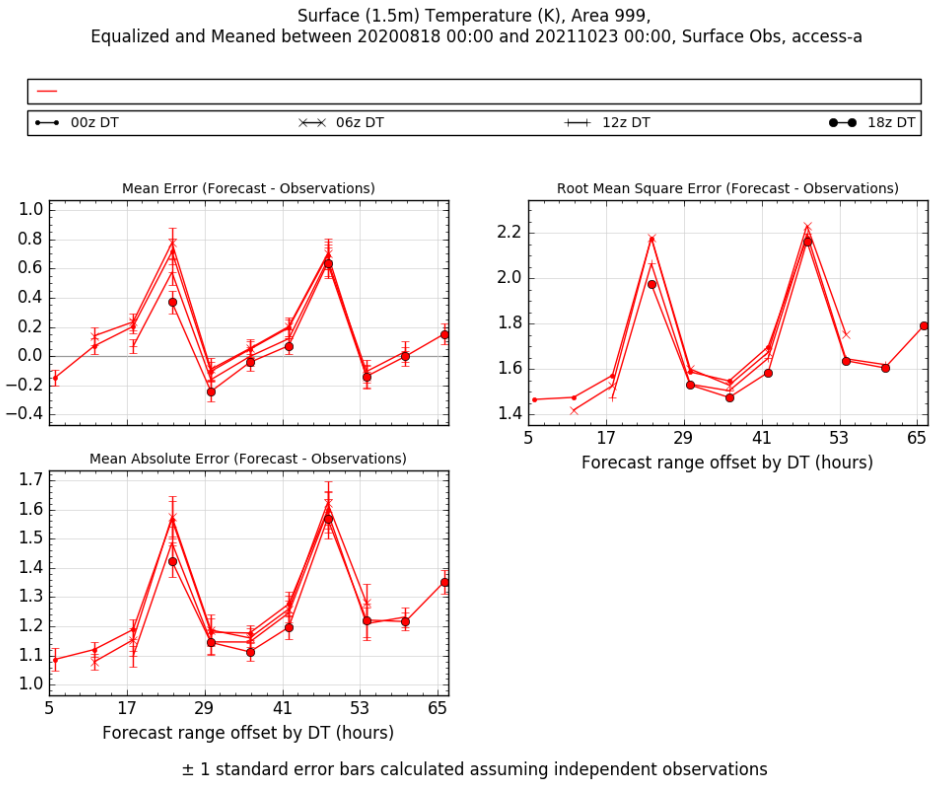


Figure 50: ACCESS-A diurnal range of screen level temperature error for SEAUS.

ACCESS-A screen level temperature biases in SE Australia exhibit the same characteristics as in the subtropics, with a generally neutral bias apart from the morning (0000UTC, 10-11am) where there is a warm bias of about 0.6 degrees (see Figure 50). The magnitude of the 1.5 temperature RMSE is less in the SE Australia domain compared to the subtropics, apart from the maximum error that is of a similar magnitude (~2.1 degrees) and occurs at the same time of local morning 0000UTC. This is the time when the largest 1.5m RH RMSE and bias occurs, which is slightly larger for SE Australia compared to the subtropics (Figure 51).

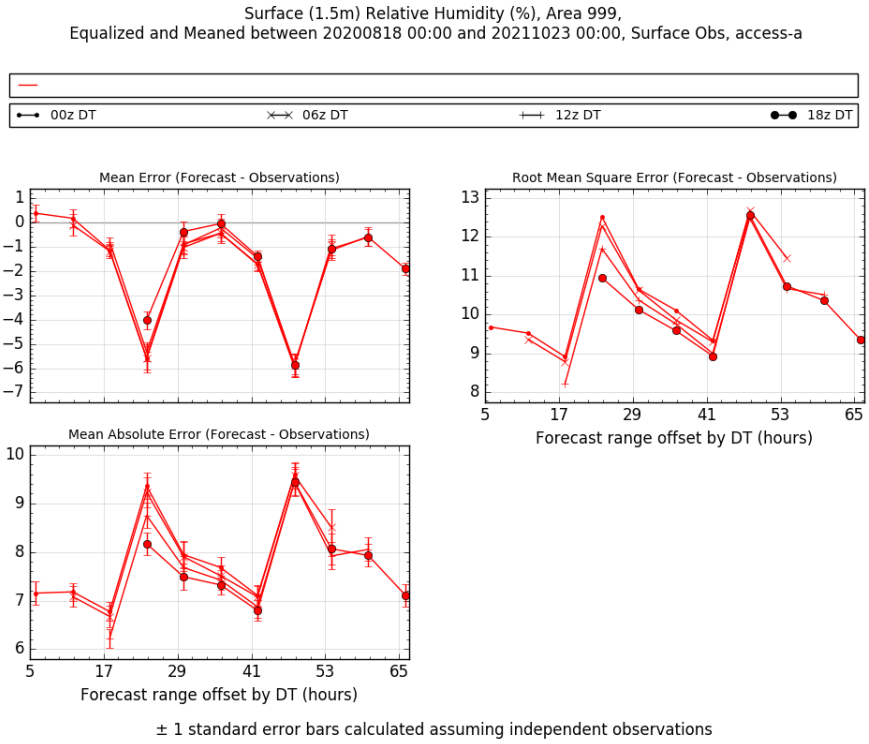


Figure 51: ACCESS-A diurnal range of screen level relative humidity error for SEAUS.

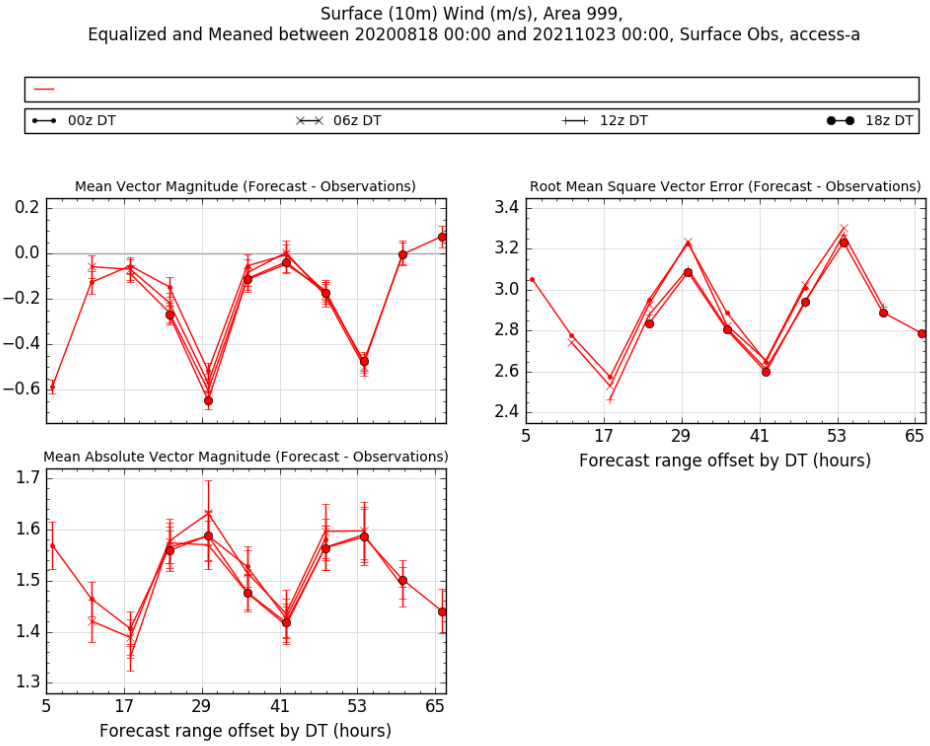


Figure 52: ACCESS-A diurnal range of 10m wind error for SEAUS.

The 10m winds in the SE Australia domain tend to be too weak with a maximum bias of -0.6 m/s occurring at 0600UTC when the RMSE is about 3 m/s (Figure 52). There is a clear diurnal cycle in the 10m wind error with more accurate wind speeds overnight and larger errors during the daytime. The total cloud cover verification shows that generally the cloud cover has a small underestimate of around 10% (see Figure 53) and a mean absolute error of typically between 20 and 30%, which is similar to the total cloud MAE for the tropical and subtropical domains.

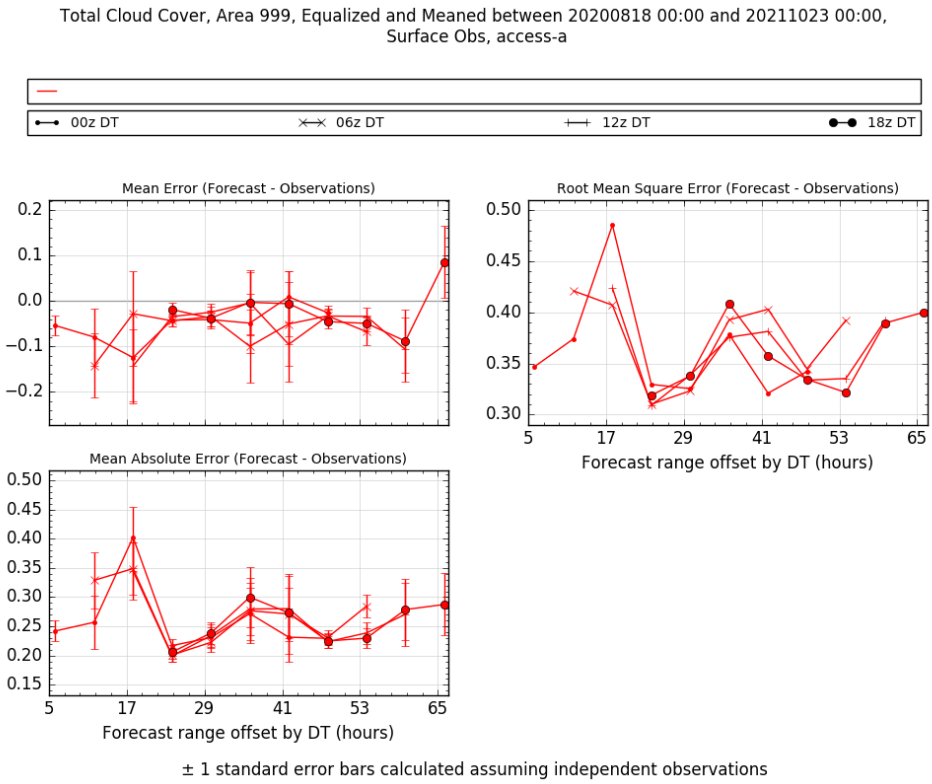


Figure 53: ACCESS-A diurnal range of cloud amount error for SEAUS.

## 4.4 Central Australian domain verification

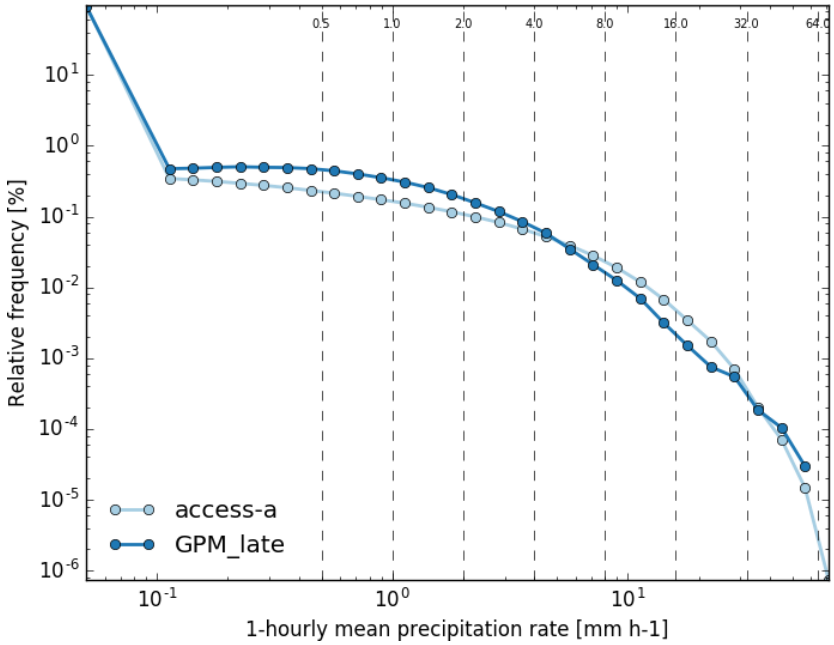


Figure 54: Histogram of the ACCESS-A and GPM hourly mean precipitation rate over the Central region.

The ACCESS-A rain rate histogram comparison with GPM for the central Australian domain shows results similar to the tropical domain, with an underestimate of low rain rates and too many occurrences of medium rates between 4 and 32 mm/hr (see Figure 54). Compared to the 6 hourly gauge precipitation accumulations shown in Figure 55, the model shows a small overestimate of the accumulated precipitation by < 0.1 mm/6 hr after the model has spun up.

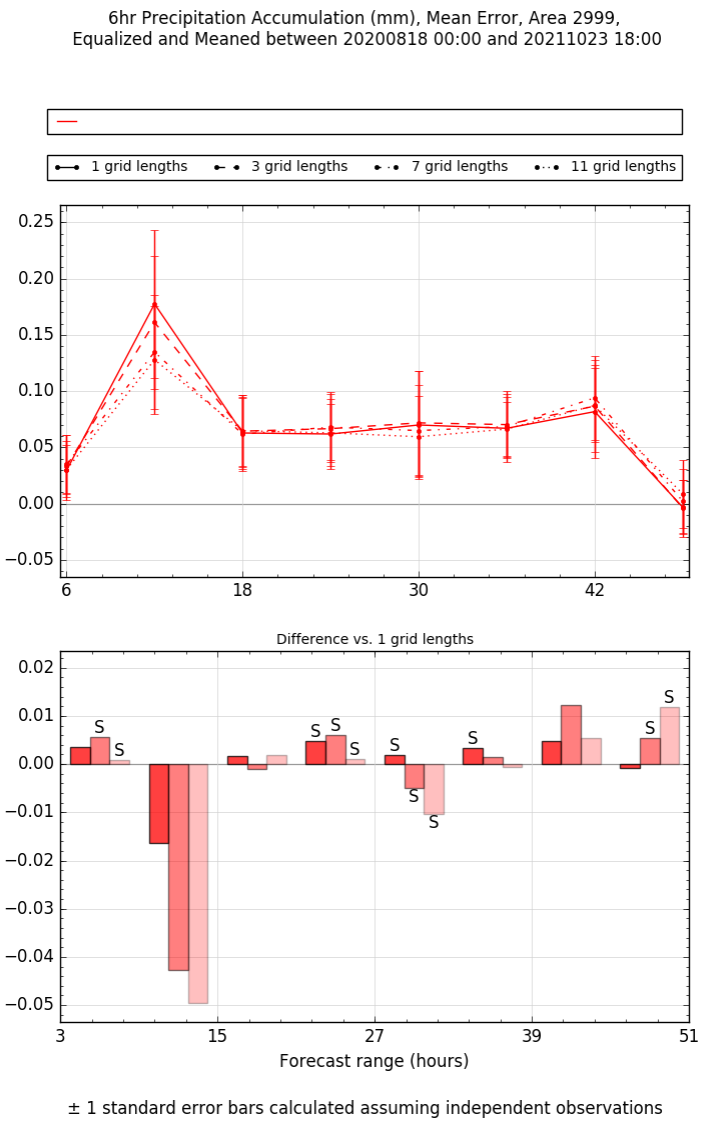


Figure 55: ACCESS-A precipitation mean error as a function of lead time against rain gauges over the Central region.

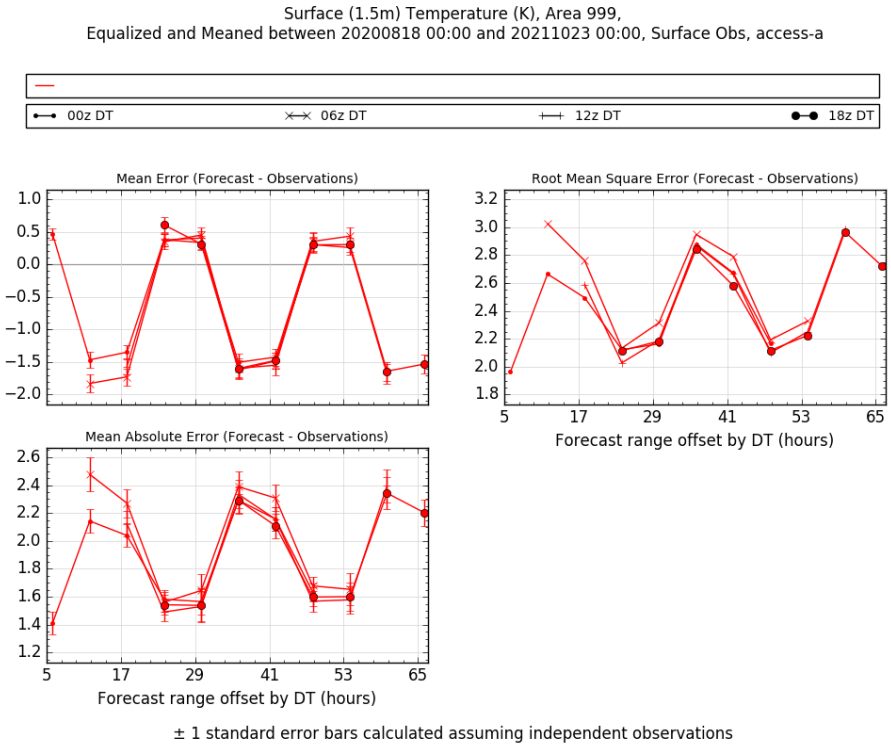


Figure 56: ACCESS-A diurnal range of screen level temperature error for the Central region.

Overnight screen level temperatures in the central Australia domain shown in Figure 56 have a cold bias with a maximum of about -1.5 degrees. This switches to a small warm bias during the morning with RMSE peaking around local noon. The 1.5m relative humidity errors are similar to the tropical domain with a moist bias overnight and unbiased during the daytime (see Figure 57). The cold and moist bias in the central Australia domain occurs at the time of the largest 10m wind speed bias (see Figure 58). The wind speed bias has a clear diurnal cycle with the overnight winds too high, with RMSE of around 3.5 m/s and MSE increasing with lead time.

While there is limited cloud cover in this domain during the assessment times to generate robust statistics, the verification of cloud cover shown in Figure 59 indicates that the model does not produce enough cloud cover. The ME in cloud fraction increases with lead time from 0.15 to 0.25. The cloud cover observations only cover the daytime, and future research will use satellite observations of cloud cover to assess whether the cold bias overnight throughout the central Australia domain is linked to a lack of cloud cover.

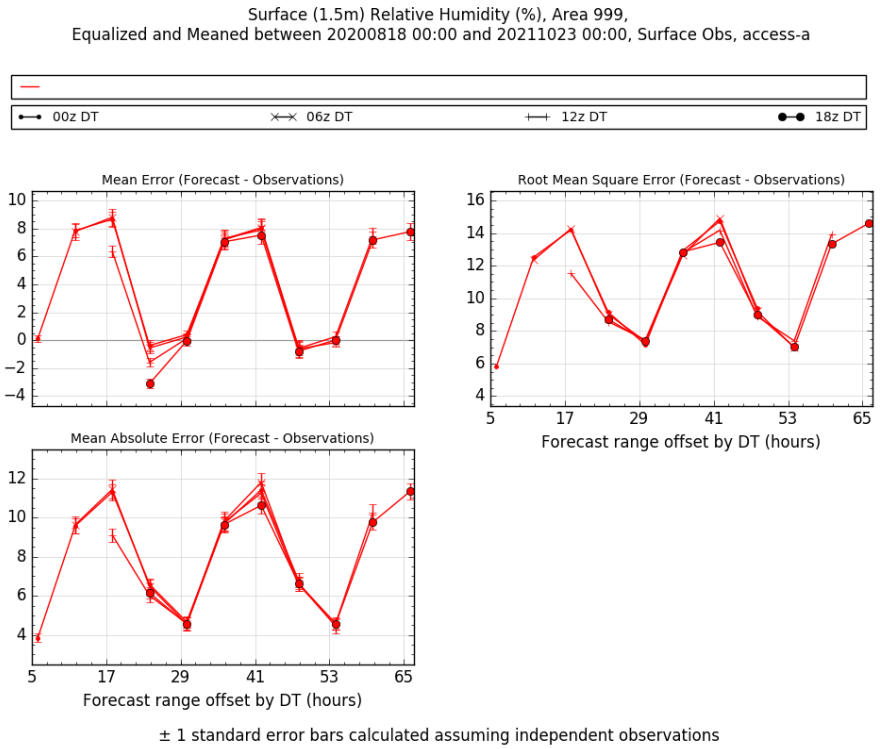


Figure 57: ACCESS-A diurnal range of screen level relative humidity error for the Central region.

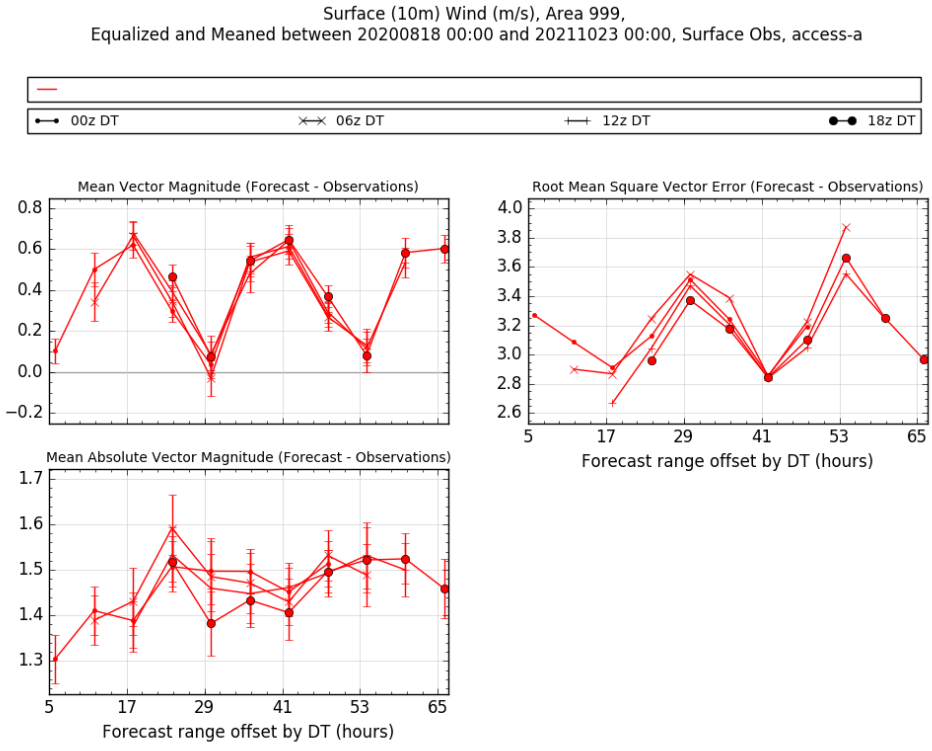


Figure 58: ACCESS-A diurnal range of 10m wind error for the Central region.

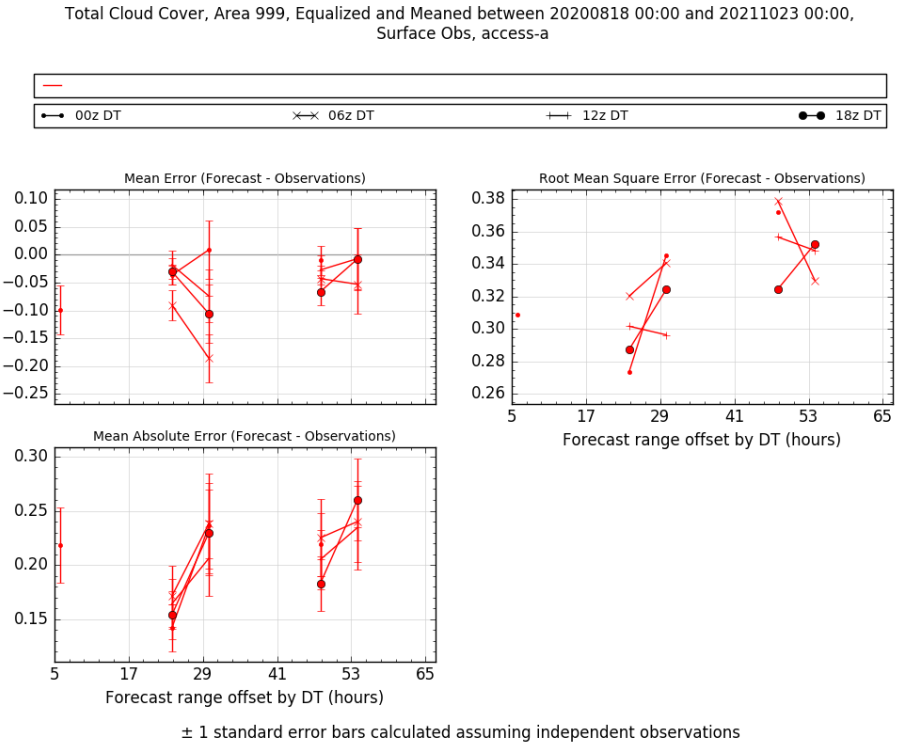


Figure 59: ACCESS-A diurnal range of cloud amount error for the Central region.

# 4.5 Mediterranean domain verification

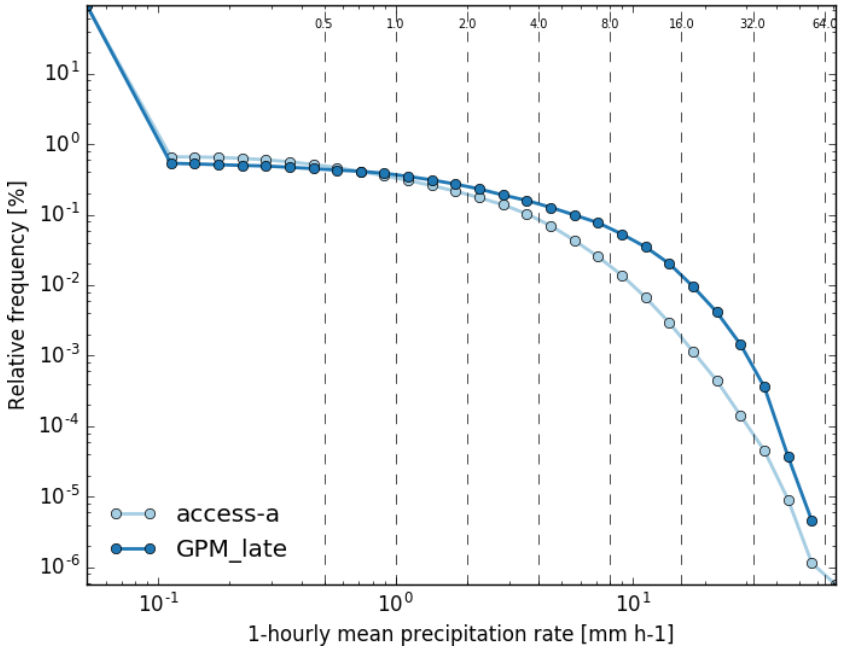


Figure 60: Histogram of the ACCESS-A and GPM hourly mean precipitation rate over the Mediterranean region

The Mediterranean domain shows that light rain rates < 2mm/hr are represented well in ACCESS-A, however, heavier rain rates are too infrequently produced by the model (Figure 60). The rainfall ME compared to gauges shown in Figure 61 demonstrates that the 6 hourly precipitation accumulations are generally within 0.1 mm/6hr, with the afternoon showing an underestimation of rain.

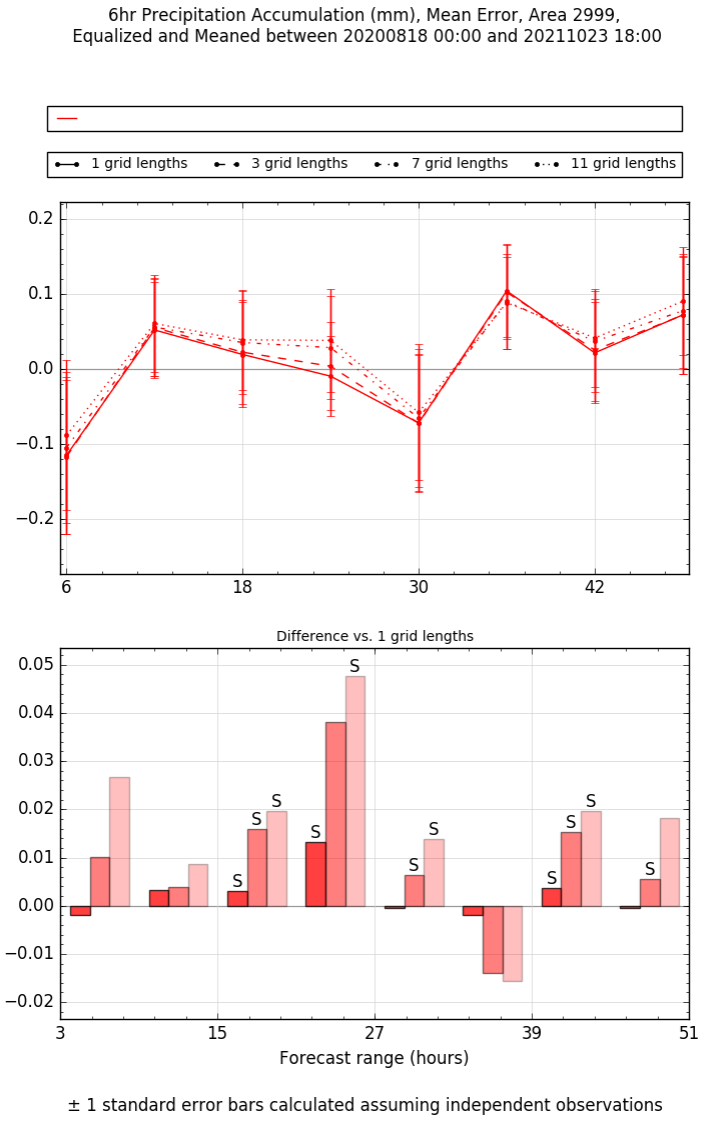


Figure 61: Timeseries of ACCESS-A precipitation mean error against rain gauges over the Mediterranean region.

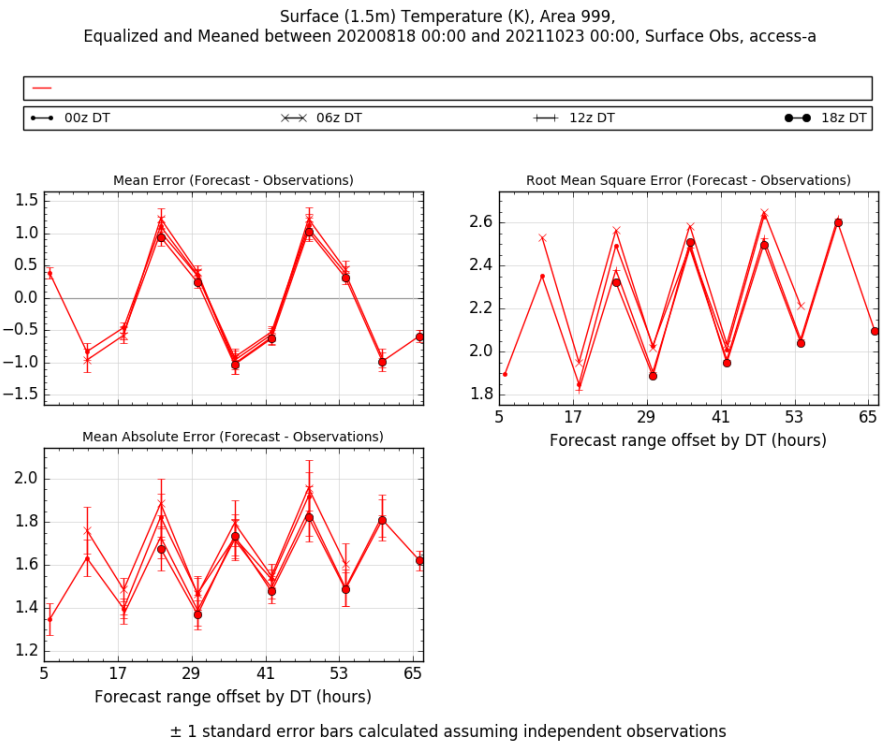


Figure 62: ACCESS-A diurnal range of screen level temperature error for the Mediterranean region.

The screen level temperature verification (Figure 62) shows a balanced bias (~ +/- 1.0 degrees) across the diurnal cycle, with the peak warm bias occurring around 0800 local time and the peak cold bias at 2000 local time. The RMSE for the Mediterranean screen level temperature is lower than for the central Australian region but higher than the SE Australian region.

The screen level relative humidity (see Figure 63) shows that the model peak dry bias and RMSE occurs at 0800 local time, which is the time when the 10m wind speed bias in the model is the lowest (Figure 64). The 10m wind speeds are underestimated in the Mediterranean domain, with a sharp change in the bias from 0800 to the largest bias occurring around local noon.

The total cloud cover verification results in Figure 64 show that ACCESS-A underestimates the cloud cover in the Mediterranean domain with the largest bias of up to 30% occurring at around local midnight, which is likely to contribute to the cold bias overnight.

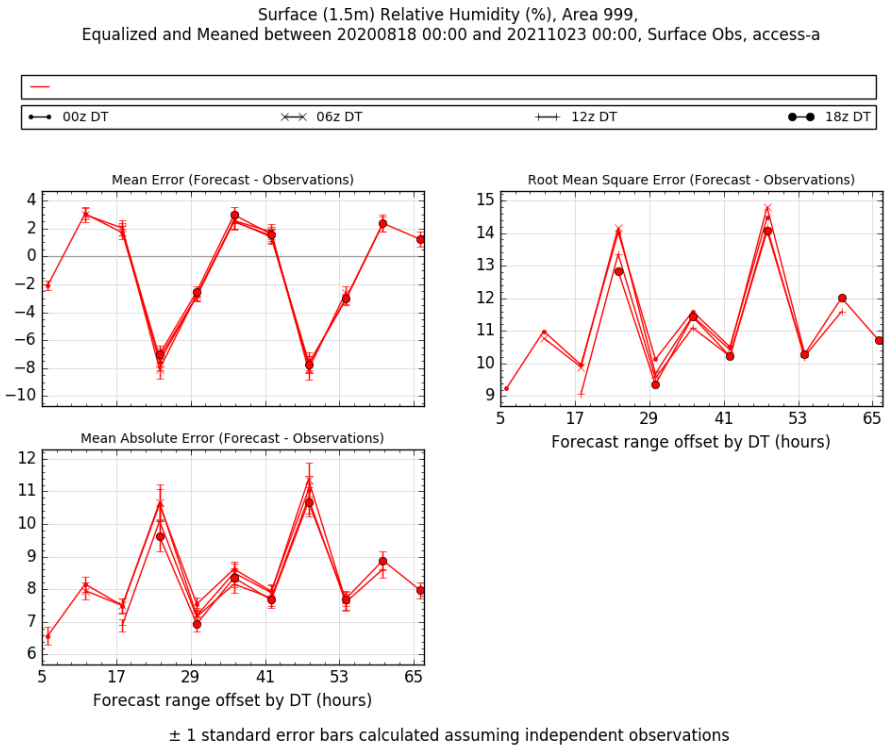


Figure 63: ACCESS-A diurnal range of screen level relative humidity errors for the Mediterranean region.

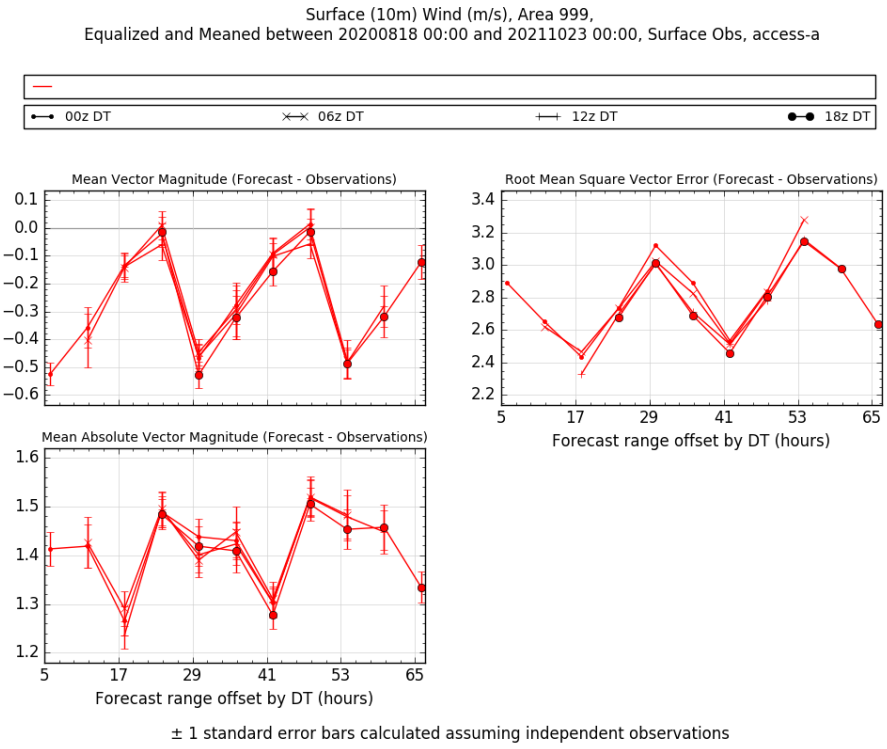


Figure 64: ACCESS-A diurnal range of 10m wind errors for the Mediterranean region.

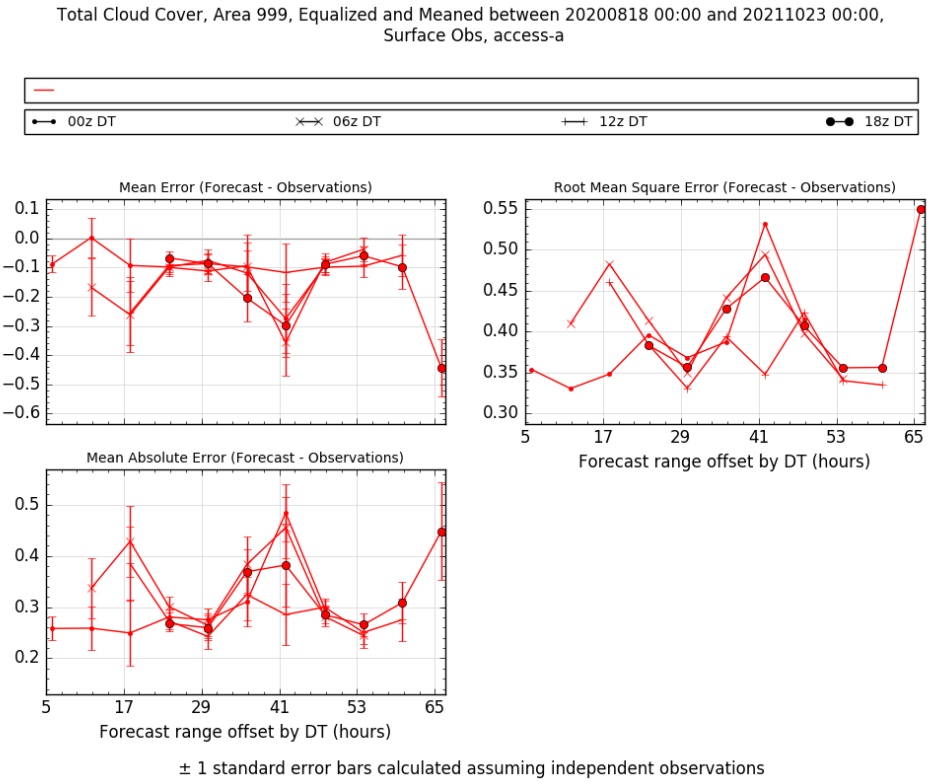


Figure 65: Figure 66: ACCESS-A diurnal range of cloud amount error for the Mediterranean region.

# 5. Known issues

The top of atmosphere outgoing longwave radiation (OLR) field was shown as part of the TC Uesi case study, see section 3.2. As part of the investigation into this case, evidence was found of 'binary' high cloud fields. Figure 67 shows the top of atmosphere OLR (top left), the low cloud fraction (top right), the medium cloud fraction (bottom left) and the high cloud fraction (bottom right), for 30-hour forecasts valid at 2020-02-14 0600Z. All three cloud types cover significant fractions of the domain. Both the low and medium cloud fractions show significant regions of 100% coverage, however there are also regions where the cloud fraction is >0 % but less than 100%. The high cloud fraction is predominantly binary, either 0% or 100% cloud cover with only very small regions exhibiting cloud fractions between the two extremes. The 'binary' high cloud fraction is a known issue caused by the calculation of ice cloud cover in the bimodal cloud scheme in the RAL3 physics configuration. This issue is also illustrated in Figure 68, which shows that the histogram of low cloud cover, which is dominated by liquid cloud, has many more occurrences of partial cloud cover compared to the medium and high cloud, where ice cloud dominates.

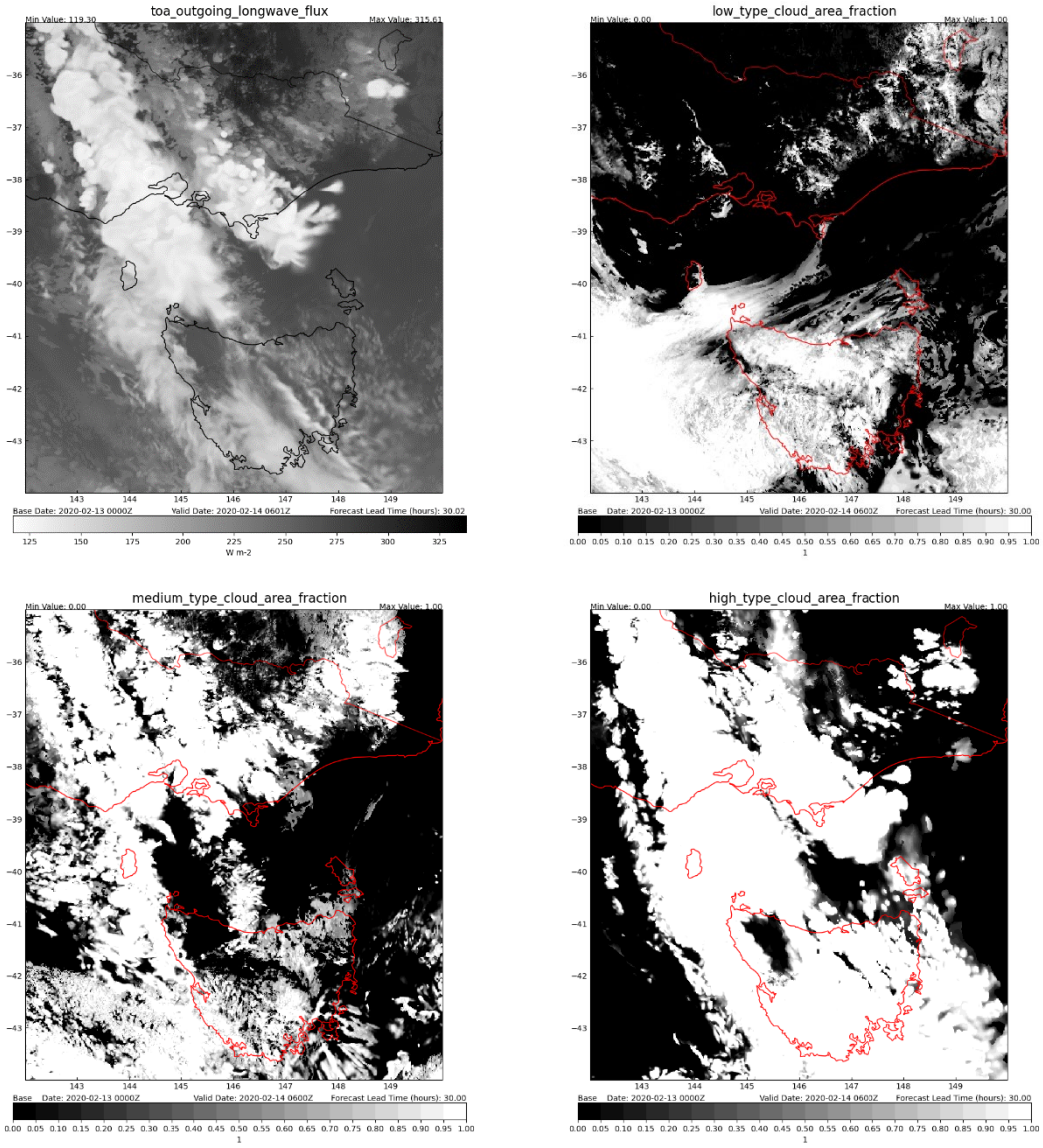


Figure 67: Top of atmosphere longwave outgoing radiation (top left), low cloud area fraction (top right), medium cloud area fraction (bottom left), and high cloud area fraction (bottom right) 30-hour forecasts valid at 2020-02-14 06Z. This example illustrates one of the known issues of the RAL3.2 configuration – the 'binary' high cloud fraction.

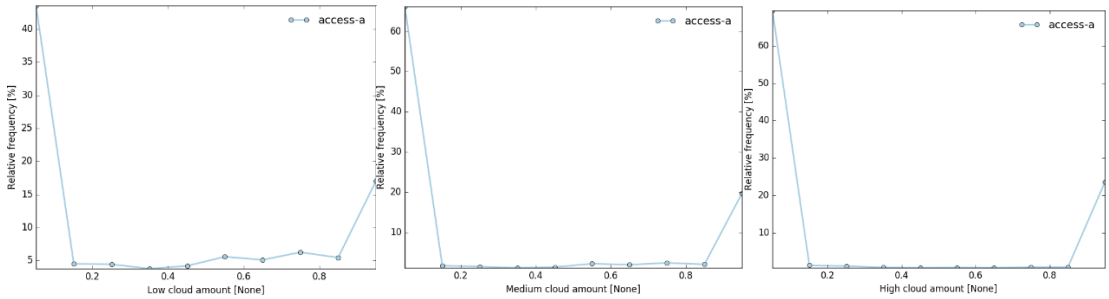


Figure 68: Histograms of low (left) medium (centre) and high (right) cloud fractions for the SEAUS domain.

Another known issue with the RAL3.2 configuration is the presence of 'holes' in the instantaneous 1km altitude radar reflectivity fields, see Figure 69 for an example but note that while these areas of no radar reflectivity do appear in ACCESS-A, they are not common. There are two known causes for these holes: one is related to the ice melting when non-monotonic temperature profiles are inherited from the initial conditions; and the second cause is due to the size sorting of rain drops over a depth of 5 km in the tropics. At the time of this work, these issues were being investigated.

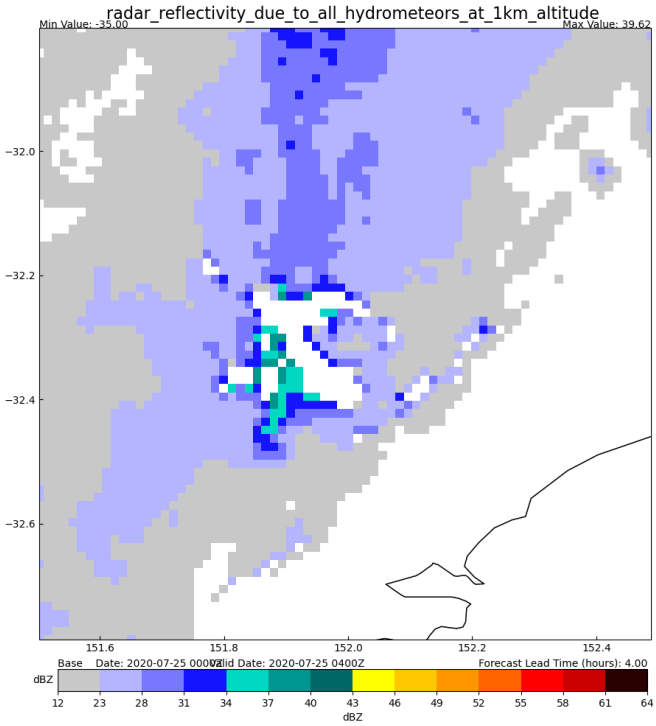


Figure 69: Example of the reflectivity holes in the ACCESS-A output.

# 6. Summary

This report documents the development and evaluation of the ACCESS-A model, focusing on its grid design and scientific configuration prior to the introduction of data assimilation. The model uses a pan-Australia variable resolution grid with horizontal resolution smoothly transitioning from 1.5 to 4 km at the boundaries to effectively manage lateral boundary spin-up artifacts. The science configuration assessed is RAL3.1 (Regional Atmosphere and Land), which forms the operational baseline for ACCESS-A, apart from a minor fix introduced in RAL3.2 that does not alter model behaviour or performance. This pre-assimilation development and testing ensures that the model accurately represents the physics and dynamics of the atmosphere–land system, is numerically stable, and provides a reliable foundation for the assimilation of observational data.

Model performance shows generally good results across domains and for different meteorology. Tropical cyclone intensity is generally underestimated, though this finding is based on a limited number of cases. Rainfall during flooding events is well captured, with some spatial displacement of the heaviest precipitation at times. Thunderstorm tracks and lightning compare well with qualitative observations, indicating realistic convective behaviour. Fog and low visibility conditions are also effectively simulated, supporting the model's use in operational forecasting.

ACCESS-A model verification across multiple domains reveals consistent biases in rainfall, temperature, humidity, wind, and cloud cover. In tropical regions, the model underestimates light and heavy rain rates compared to satellite data, while slightly underestimating 6-hourly rainfall accumulations against rain gauge observations. Temperature and humidity show a general cold and moist bias, especially overnight, with wind speeds overestimated during the night and underestimated during the day. In subtropical and SE Australia domains, rainfall accumulations align well with gauges despite an underestimation of medium-high rain rates compared to GPM IMERG satellite observations. Temperature biases are mostly neutral with a warm morning bias. Wind speeds are typically underestimated, and cloud cover is slightly underpredicted, with RMSE values similar across regions.

In central Australia and the Mediterranean domain, ACCESS-A shows similar rainfall biases, underestimating light and heavy rain rates but performing well in 6-hour accumulation comparisons. Central Australia exhibits a pronounced cold and moist bias overnight, coinciding with overestimated wind speeds. The Mediterranean domain shows balanced temperature biases across the diurnal cycle, with a dry bias and underestimated wind speeds during the day. Cloud cover is underpredicted, especially overnight, likely contributing to the cold bias.

Overall, the ACCESS-A model demonstrates good performance and readiness for the introduction of data assimilation as presented in Rennie et al. (2025). Future work to understand the cause of model biases will include the use of satellite observations of cloud properties, radiosonde observations to assess the model's vertical structure of temperature and moisture and evaluation of more cases studies.

# References

Best, M. J., Pryor, M., Clark, D. B., Rooney, G. G., Essery, R. L. H., Ménard, C. B., Edwards, J. M., Hendry, M. A., Porson, A., Gedney, N., Mercado, L. M., Sitch, S., Blyth, E., Boucher, O., Cox, P. M., Grimmond, C. S. B., and Harding, R. J. (2011) The Joint UK Land Environment Simulator (JULES), model description – Part 1: Energy and water fluxes, Geosci. Model Dev., 4, 677–699.

Bohnenstengel, S. I., Evans, S., Clark, P. A., and Belcher, S. E. (2011) Simulations of the London Urban Heat Island, Q. J. Roy. Meteor. Soc., 137, 1625–1640, https://doi.org/10.1002/qj.855.

Boutle, I., Finnenkoetter, A., Lock, A.P. and Wells, H. (2016) The London model: Forecasting fog at 333 m resolution. Quarterly Journal of the Royal Meteorological Society, 142, 360–371

Boutle, I. A., Eyre, J. E. J., and Lock, A. P. (2014) Seamless stratocumulus simulation across the turbulent gray zone, Mon. Weather Rev., 142, 1655–1668.

Bureau of Meteorology (2020a). Special Climate Statement 73 - extreme heat and fire weather in December 2019 and January 2020, Bureau of Meteorology, Melbourne.

Bureau of Meteorology. (2020b). Monthly Weather Review Australia July 2020. http://www.bom.gov.au/climate/mwr/aus/mwr-aus-202007.pdf

Bureau of Meteorology. (2020c). Halloween Hail Outbreak. Internal Environmental Prediction Services report: unpublished.

Bureau of Meteorology. (2021). Special Climate Statement 74 – extreme rainfall and flooding in eastern and central Australia in March 2021. http://www.bom.gov.au/climate/current/statements/scs74.pdf

Bush, M., Flack, D., Lewis, H., Bohnenstengel, S., Short, C., Franklin, C., Lock, A., Best, M., Field, P., McCabe, A., Van Weverberg, K., Berthou, S., Boutle, I., Brooke, J., Cole, S., Cooper, S., Dow, G., Edwards, J., Finnenkoetter, A., Furtado, K., Halladay, K., Hanley, K., Hendry, M., Hill, A., Jayakumar, A., Jones, R., Lean, H., Lee, J., Malcolm, A., Mittermaier, M., Mohandas, S., Moore, S., Morcrette, C., North, R., Porson, A., Rennie, R., Roberts, N., Roux, B., Sanchez, C., Su, C.-H., Tucker, S., Vosper, S., Walters, D., Warner, J., Webster, S., Weeks, M., Wilkinson, J., Whitall, M., Williams, K., and Zhang, H. (2025). The third Met Office Unified Model–JULES Regional Atmosphere and Land Configuration, RAL3. Geosci. Model Dev., 18, 3819–3855.

Bush, M., Boutle, I., Edwards, J., Finnenkoetter, A., Franklin, C., Hanley, K., Jayakumar, A., Lewis, H., Lock, A., Mittermaier, M., Mohandas, S., North, R., Porson, A., Roux, B., Webster, S., and Weeks, M. (2023). The second Met Office Unified Model–JULES Regional Atmosphere and Land configuration, RAL2, Geosci. Model Dev., 16, 1713–1734.

Bush, M., Allen, T., Bain, C., Boutle, I., Edwards, J., Finnenkoetter, A., Franklin, C., Hanley, K., Lean, H., Lock, A., Manners, J., Mittermaier, M., Morcrette, C., North, R., Petch, J., Short, C., Vosper, S., Walters, D., Webster, S., Weeks, M., Wilkinson, J., Wood, N., and Zerroukat, M. (2020). The first Met Office Unified Model–JULES Regional Atmosphere and Land configuration, RAL1, Geosci. Model Dev., 13, 1999–2029.

Cooper, S., Rennie S., Bridge C., Franklin C., Dietachmayer G., Steinle P., Xiao Y., Coleman T., Marshall M., and Finch J. (2025). APS3 ACCESS City Ensemble, Bureau Research Report 113, Bureau of Meteorology, http://www.bom.gov.au/research/publications/researchreports/BRR-113.pdf

Defourny, P. (2016). ESA Land Cover Climate Change Initiative (Land_Cover_cci): Global Land Cover Maps, Version 1.6.1.

De Kauwe, M. G., Disney, M. I., Quaife, T., Lewis, P., and Williams, M.: An assessment of the MODIS collection 5 leaf area index product for a region of mixed coniferous forest, Remote Sens. Environ., 115, 767–780.

Donohue, R. (2023). Australian C4 grass cover percentage, v1. CSIRO, Australia https://doi.org/10.25919/FFP4-B663.

Field, P.R., Hill, A.A., Shipway, B., Furtado, K., Wilkinson, J., Miltenberger, A., Gordon, H., Grosvenor, D.P., Stevens, R. and Van Weverberg, K. (2023). Implementation of a double moment cloud microphysics scheme in the UK Met Office regional numerical weather prediction model. Quarterly Journal of the Royal Meteorological Society,149 (752), 703–739.

Grant, D. and Courtney, J. (2023). Severe Tropical Cyclone Uesi. Bureau of Meteorology. http://www.bom.gov.au/cyclone/history/pdf/Uesi2020_report.pdf

Hanley, K., Whitall, M., Stirling, A., and Clark, P. (2019) Modifications to the representation of subgrid mixing in kilometre-scale versions of the Unified Model, Q. J. Roy. Meteor. Soc., 145, 3361–3375.

Hertwig, D., Grimmond, S., Hendry, M. A., Saunders, B., Wang, Z., Jeoffrion, M., Vidale, P. L., McGuire, P. C., Bohnenstengel, S. I., Ward, H. C., and Kotthaus, S. (2020). Urban signals in high-resolution weather and climate simulations: role of urban land-surface characterisation, Theoretical and Applied Climatology, 142, 701–728, https://doi.org/10.1007/s00704-020-03294-1.

Huffman, G.J., Bolvin, D.T., Nelkin, E.J., Tan, J. (2019). GPM IMERG Final Precipitation L3 Half Hourly 0.1° x 0.1° V06. NASA Goddard Earth Sciences Data and Information Services Center (GES DISC). DOI: 10.5067/GPM/IMERG/3B-HH/07

Kain, J. S., Weiss, S. J., Dembek, S. R., Levit, J. J., Bright, D. R., Case, J. L., Coniglio, M. C, Dean, A. R., Sobash, R. A., and Schwartz, C. S. (2008). Severe-weather forecast guidance from the first generation of large domain convection-allowing models: challenges and opportunities. 24th Conference on Severe Local Storms. https://ams.confex.com/ams/pdfpapers/141723.pdf.

Lipson, M., Nazarian, N., Hart, M. A., Nice, K. A., and Conroy, B. (2022). Urban form data for climate modelling: Sydney at 300 m resolution derived from building-resolving and 2 m land cover datasets (v1.01), https://doi.org/10.5281/ZENODO.6579061.

Lock, A. P., Brown, A. R., Bush, M. R., Martin, G. M., & Smith, R. N. B. (2000). A New Boundary Layer Mixing Scheme. Part I: Scheme Description and Single-Column Model Tests. Monthly Weather Review, 128(9), 3187–3199. https://doi.org/10.1175/1520-0493.

Manners, J., Edwards, J. M., Hill, P., and Thelen, J.-C.: SOCRATES (Suite Of Community RAdiative Transfer codes based on Edwards and Slingo) Technical Guide, Met Office, UK, https://code.metoffice.gov.uk/trac/socrates

Marín, C. J., Barrett, B. S., and Pozo, D. (2021). The tornadoes of 30–31 May 2019 in south-Central Chile: Sensitivity to topography and SST. Atmospheric Research, 249, 1-20. https://doi.org/10.1016/j.atmosres.2020.105301

Mittermaier, M. (2014). A strategy for verifying near-convection-resolving forecasts at observing sites, Weather Forecast., 29, 185–204, https://doi.org/10.1175/WAF-D-12-00075.1.

Morrison, H., Thompson, G. and Tatarskii, V. (2009) Impact of cloud microphysics on the development of trailing stratiform precipitation in a simulated squall line: comparison of one-and two-moment schemes. Monthly Weather Review, 137(3), 991–1007.

Porson, A., Clark, P., Harman, I., Best, M., and Belcher, S. (2010). Implementation of a new urban energy budget scheme in the MetUM. Part I: Description and idealized simulations, Q. J. Roy. Meteor. Soc., 136, 1514–1529, https://doi.org/10.1002/qj.668.

Rennie, S. Franklin, C.N. Cooper, S., Roux, B., Steinle, P., Zidikheri, M., Eizenberg, N., Dharssi, I., Krysta, M., Khanarmuei, M., Smith, F., Smith, A., Samrat, N., Griffin, C. and Brook, J., (2025). ACCESS-A: Developing convective scale NWP for the Australian continent. Submitted to Journal of Southern Hemisphere Earth System Science.

Rennie, S., Cooper, S., Steinle, P., Dietachmayer, G., Krysta, M., Franklin, C., Bridge, C., Marshall, M., Xiao, Y., & Sgarbossa, D. (2022). ACCESS-C: Australian Convective-Scale NWP with Hourly 4D-Var Data Assimilation. Weather and Forecasting. https://doi.org/10.1175/WAF-D-21-0183.1

Roberts, N. M., and Lean, H. W. (2008) Scale-Selective Verification of Rainfall Accumulations from High-Resolution Forecasts of Convective Events. Monthly Weather Review, 136(1), 78-97.

Roff, G., Bermous, I., Dietachmayer, G., Fernon, J., Fraser, J., Lu, W., Rennie, S., Steinle, P., & Xiao, Y. (2022). APS2-ACCESS-C2: the first Australian operational NWP convection-permitting model. Journal of Southern Hemisphere Earth Systems Science, 72(1), 1–18. https://doi.org/10.1071/ES21013

Smagorinsky, J. (1963). General Circulation Experiments With The Primitive Equations. Monthly Weather Review, 91(3), 99–164. https://doi.org/10.1175/1520-0493.

Sobash, R. A., Kain, J. S., Bright, D. R., Dean, A. R., Coniglio M. C., and Weiss, S. J. (2011). Probabilistic Forecast Guidance for Severe Thunderstorms Based on the Identification of Extreme Phenomena in Convection-Allowing Model Forecasts. Weather and Forecasting, 26(5), 714-728. https://doi.org/10.1175/WAF-D-10-05046.1

Still, C. J., Berry, J. A., Collatz, G. J., and Defries, R. S. (2009). ISLSCP II C4 Vegetation Percentage, ORNL DAAC, Oak Ridge, Tennessee, USA https://doi.org/10.3334/ORNLDAAC/932.

Zanaga, D., Van De Kerchove, R., De Keersmaecker, W., Souverijns, N., Brockmann, C., Quast, R., Wevers, J., Grosu, A., Paccini, A., Vergnaud, S., Cartus, O., Santoro, M., Fritz, S., Georgieva, I., Lesiv, M., Carter, S., Herold, M., Li, L., Tsendbazar, N.-E., Ramoino, F., and Arino, O. (2021). ESA WorldCover 10 m 2020 v100 (v100), https://doi.org/10.5281/zenodo.5571936.

Van Weverberg, K., Morcrette, C.J., Boutle, I., Furtado, K. and Field, P.R. (2021) A bimodal diagnostic cloud fraction parameterization. Part I: Motivating analysis and scheme description. Monthly Weather Review, 149 (3), 841–857.

Walters, D. N., Baran, A., Boutle, I., Brooks, M., Earnshaw, P., Edwards, J., Furtado, K., Hill, P., Lock, A., Manners, J., Morcrette, C., Mulcahy, J., Sanchez, C., Smith, C., Stratton, R., Tennant, W., Tomassini, L., Weverberg, K. V., Vosper, S., Willett, M., Browse, J., Bushell, A., Dalvi, M., Essery, R., Gedney, N., Hardiman, S., Johnson, B., Johnson, C., Jones, A., Mann, G., Milton, S., Rumbold, H., Sellar, A., Ujiie, M., Whitall, M., Williams, K., and Zerroukat, M. (2019). The Met Office Unified Model Global Atmosphere 7.0 and JULES Global Land 7.0 configurations, Geosci. Model Dev., 12, 1909–1963, https://doi.org/10.5194/gmd-12-1909-2019.

Warner, J.L., Franklin, C.N., Roux, B., Cooper, S., Rennie, S. and Kumar, V. (2025). Diagnosing lateral boundary spin-up in regional models using an age-of-air diagnostic. Quarterly Journal of the Royal Meteorological Society, https://doi.org/10.1002/qj.4971

Wood, N., Staniforth, A., White, A., Allen, T., Diamantakis, M., Gross, M., Melvin, T., Smith, C., Vosper, S., Zerroukat, M., and Thuburn, J. (2014) An inherently mass-conserving semi-implicit semi-Lagrangian discretization of the deep-atmosphere global non-hydrostatic equations, Q. J. Roy. Meteor. Soc., 140, 1505–1520.

Zanaga, D., Van De Kerchove, R., De Keersmaecker, W., Souverijns, N., Brockmann, C., Quast, R., Wevers, J., Grosu, A., Paccini, A., Vergnaud, S., Cartus, O., Santoro, M., Fritz, S., Georgieva, I., Lesiv, M., Carter, S., Herold, M., Li, L., Tsendbazar, N.-E., Ramoino, F., and Arino, O. (2021). ESA WorldCover 10 m 2020 v100 (v100), https://doi.org/10.5281/zenodo.5571936.